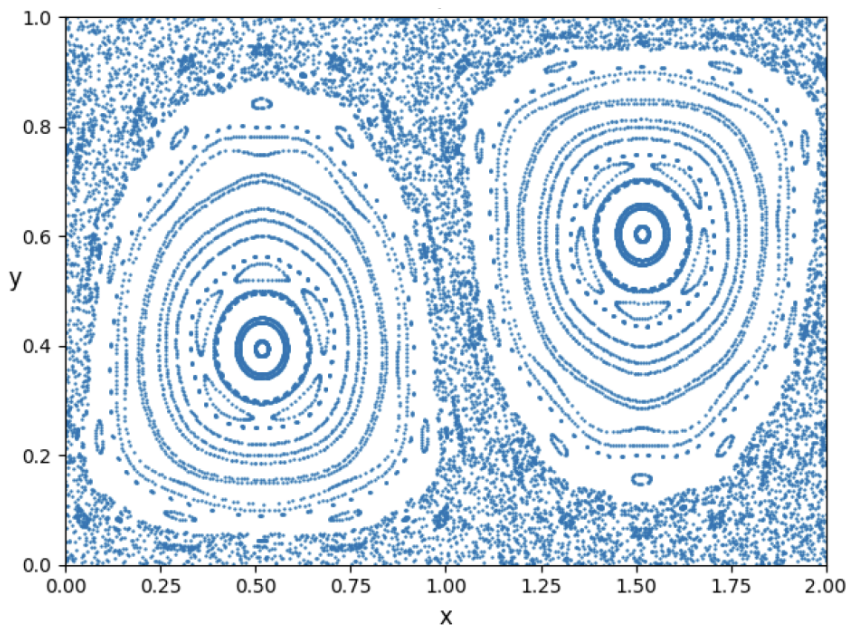

Using particle tracking to simulate sediment transport in estuaries



Author:
Niels Hendrikx

Supervisors:
Leo Maas & Maarten van der Vegt

April 17, 2018



Universiteit Utrecht

Using particle tracking to simulate sediment transport in estuaries

Abstract

The morphology of estuaries is characterized by a complex channel-shoal pattern. Interaction between river and tidal currents produces a wide variety of sand bar types. These sand bars are not static and migrate due to tidal and residual currents. Sand bars can move into shipping channels or harbors and removing them requires costly dredging activities. Eventually sand bars may regrow and pose the same problem. Hence, understanding how sand bars develop and evolve in estuaries is of importance. Currently, already a few theories exist that predict sand bar shapes and dimensions given some estuarine properties. However, predictions are wrong compared to observations, suggesting a lack of understanding. To this end, a numerical model was set up which simulates sediment transport in a different way than usual. Instead of an Eulerian approach, particle tracking is used for the advection of sediment. Particle tracking offers additional information on the flow dynamics that is lost in the Eulerian approach. This potentially can help to improve understanding of sand bar dynamics. An outline of particle tracking and some examples of particle trajectories are presented. Furthermore a few preliminary results on the simulation of sand bars are discussed.

Contents

| | | |
|----------|--|-----------|
| 1 | Introduction | 3 |
| 2 | Physics and literature review | 5 |
| 2.1 | Tidal bar dimensions and characteristics | 5 |
| 2.2 | Hydrodynamics in estuaries | 8 |
| 2.3 | Residual velocity and vorticity | 11 |
| 2.4 | Sediment transport and bed evolution | 13 |
| 2.5 | Compound tides | 15 |
| 3 | Methods | 18 |
| 3.1 | Hydrodynamical model | 18 |
| 3.2 | Kinematic model | 18 |
| 3.3 | Sediment transport model | 18 |
| 3.4 | Model outline | 18 |
| 4 | Hydrodynamic model | 20 |
| 4.1 | Computational grid | 20 |
| 4.2 | Alternating direction implicit method | 20 |
| 4.3 | Boundary conditions | 22 |
| 4.3.1 | Closed boundaries | 22 |
| 4.3.2 | Open boundary | 23 |
| 4.4 | Initial conditions | 24 |
| 4.5 | Model input and output | 24 |
| 4.6 | Comments on stability, accuracy and consistency | 24 |
| 4.7 | Verification hydrodynamical model | 27 |
| 4.7.1 | Kelvin waves and harmonic analysis | 27 |
| 4.7.2 | Velocity field analysis | 29 |
| 4.7.3 | Resonance effects | 34 |
| 4.7.4 | Residual current verification | 34 |
| 5 | Sediment transport and bed evolution model | 37 |
| 5.1 | Numerical implementation particle tracking | 37 |
| 5.2 | Numerical implementation erosion and deposition | 41 |
| 5.3 | Verification kinematic model | 42 |
| 5.3.1 | Particle trajectories numerical results | 42 |
| 5.3.2 | Particle trajectories (semi-) analytical results | 46 |
| 5.4 | Verification implementation sediment transport | 50 |
| 5.4.1 | Spatial settling lag test case | 51 |
| 6 | Numerical experiments and results | 53 |
| 6.1 | Chaotic advection of sediment | 53 |
| 6.2 | Linear stability analysis | 56 |
| 6.3 | Transient morphodynamics | 59 |
| 7 | Discussion | 61 |
| 8 | Conclusion | 64 |

1 Introduction

The morphology of estuaries is characterized by a complex channel-shoal pattern. Interaction between river and tidal currents produces a wide variety of sand bar types. These sand bars are not static and migrate due to residual and tidal currents. Sand bars can move into shipping channels or harbors and removing them requires⁶ costly dredging activities. Eventually sand bars may regrow and pose the same problem. Next to this, morphology also influences³⁶ flow dynamics which in turn may have consequences for ecology. Hence, understanding how sand bars develop and evolve in estuaries is of importance. Complex numerical models can already simulate¹⁵ the development of sand bars, but these models are too complex to extract the physical mechanisms responsible for sand bar formation. However, current theoretical models¹⁷ cannot yet accurately reproduce tidal bars and dimensions in relation to estuarine width and depth. Theoretical models are often based on a mathematical tool called linear stability analysis.^{10,26} According to these theoretical models, tidal excursion length determines sand bar length, while observations¹⁷ suggest that estuarine width is the most important lengthscale that determines sand bar length. This suggests that an essential physical mechanism is missed by the current theories.

In this project, a numerical model was developed that uses particle tracking to simulate sediment transport. This implies that, instead of the conventional Eulerian approach to sediment transport, a Lagrangian viewpoint is used. This Lagrangian viewpoint comprises that the water volume is divided in numerous small sub-volumes. Each sub-volume can hold sediment and can freely move throughout the domain according to the hydrodynamics. While this sub-volume moves throughout the domain, it can pick up sediment by erosion but also loose sediment by means of deposition. Information about the movement of these sub-volumes is lost in an Eulerian description. The question is, can we, by introducing a Lagrangian viewpoint, capture physical mechanisms that are missed by theoretical models?

For the Eulerian approach only the Navier Stokes equations, or a simplified version of these equations, are used to solve the dynamics. Additionally, the concentration equation is solved for every gridcell in the domain. By using this Eulerian approach, information about where the water (which holds sediments) moves to, is not explicitly obtained. This can only be obtained by solving the kinematic equations, which are nonlinear ordinary partial differential equations due to its nonlinear righthand side:

$$\frac{d\mathbf{x}}{dt} = \mathbf{u}(\mathbf{x}, t) \quad (1)$$

In this way, more rich and complete dynamics of the water flow can be captured. For simplicity, from now on, we refer to the small sub-volumes of water as: particles. Even for simplified velocity fields, very complicated trajectories of these particles can be expected. Nevertheless, information on particle trajectories may improve our understanding of sediment transport. By using particle tracking, the morphology is studied as a function of both estuarine length and width. Hence, the main question of this project can be formulated as: can we predict the evolution of estuarine morphology by using particle tracking?

Since it is difficult to improve our understanding of sand bar formation by using very complicated numerical models, a conceptual numerical model to solve the hydrodynamics was developed. Hence, in this project a simple geometry is used: a rectangular estuary with only one open boundary. At the open boundary, tidal forcing is applied with the main tidal constituent M2. This is the only external forcing: river dynamics are neglected by assuming river input is weak. Moreover, this estuary is assumed to be shallow, implying that the velocity fields are assumed to be approximately two dimensional. Therefore, the 2D depth averaged shallow water equations are numerically solved.

In the process of developing both the hydrodynamic and sediment transport models, many benchmark problems were used as a verification. The hydrodynamic model is capable of reproducing velocity structures and patterns that closely follow analytical solutions, see section 4. Even though the sediment transport model uses a Lagrangian viewpoint, the hydrodynamic model still provides an Eulerian velocity field. This Eulerian velocity field is in turn used by the sediment transport model to solve the kinematic equations, which requires a Lagrangian viewpoint. Subsequently, for each particle the concentration equation is solved, more details follow in sections 2 and 5.

In addition to studying the initial formation of sand bars, another interesting point of research is to investigate the coupling between hydrodynamics and morphodynamics on long timescales. Erosion and deposition lead to changes in the bedprofile, and this in turn changes the hydrodynamics. Even though the dynamics on longer timescales received attention, this deserves more research.

Summarized, this study aims to improve our understanding of sand bars by using a conceptual model that uses particle tracking to simulate sediment transport. By doing so, information about where the water and the sediment it is holding, is obtained. Ultimately, this provides knowledge about the development of sand bars and contributes to our ability to predict sand bar characteristics in estuaries.

2 Physics and literature review

This section reviews the mismatch between theory and observations regarding sand bar shapes and dimensions. In addition, theory on hydrodynamics and sediment transport is presented, which is required to set up the numerical model. This includes a short introduction to dynamical systems required to understand particle tracking.

2.1 Tidal bar dimensions and characteristics

As a starting point, before comparing theory on tidal bars with observations, a short introduction about sand bars is given. Depending on estuary geometry, sediment properties and hydrodynamic conditions, different tidal bar types prevail. Tidal bars can be classified based on their shape¹⁷ and the following types can be distinguished:

- Linear bars
- U-shaped bars
- Sidebars
- Compound bars

Compound bars have more complex structures as can be observed in figure 1, moreover: each bar type has its own length to width ratio. For linear bars, the ratio¹⁷ is $L = 6.9 W$. Even though the length scale of the bars in figure 1 is in the order of a few hundred meters, tidal bars can have a length of more than ten kilometers.¹⁷

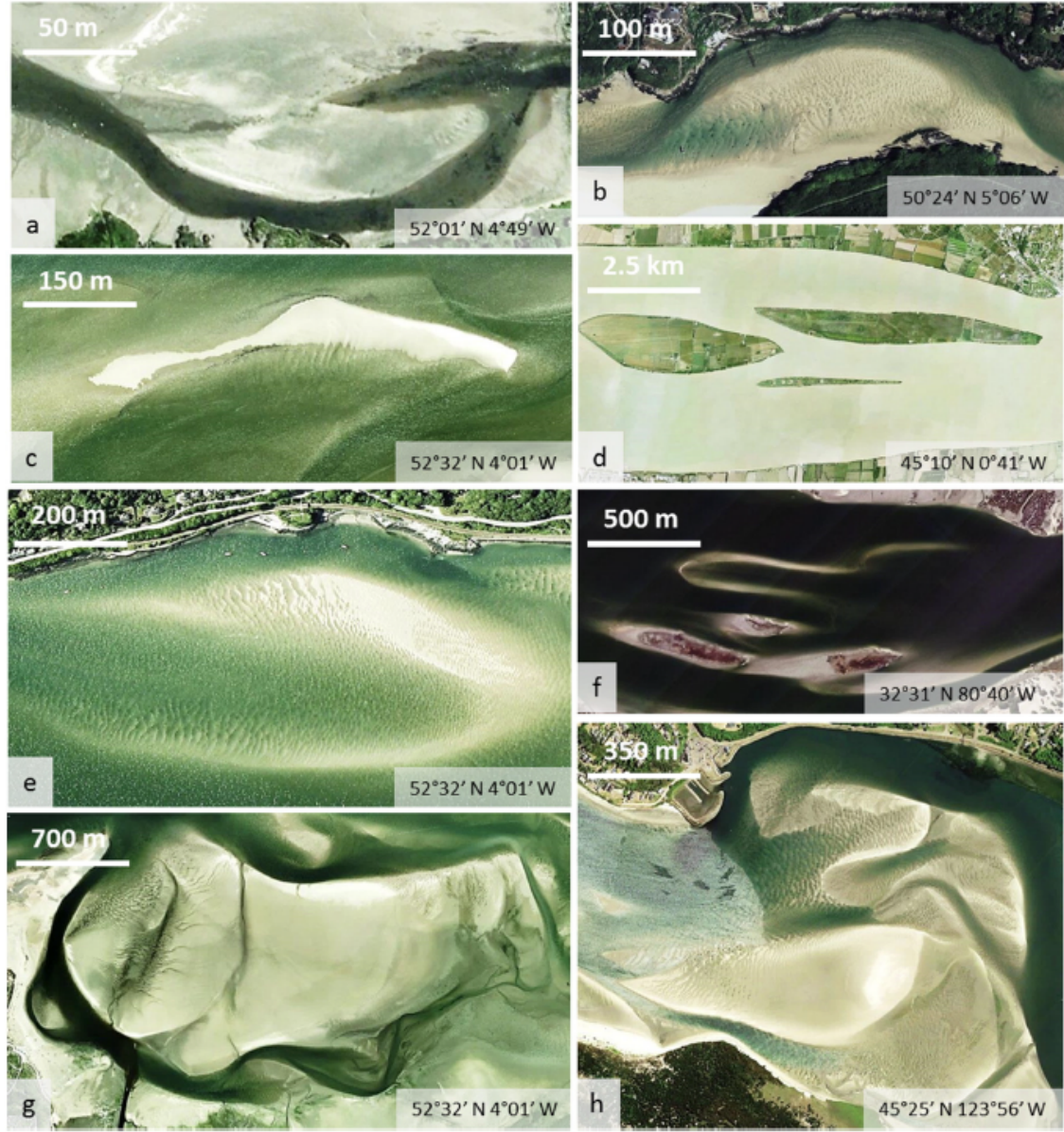


Figure 1: Satellite images used by Leuven et al. (2016) to classify bar types in estuaries. a & b: side bars, c & d: linear bars, e & f: u-shaped bars, g & h: compound bars. For more details the reader is referred to Leuven et al (2016).

Two parameters are often used when it comes to tidal bar descriptions, bar mode (figure 2) and the aspect ratio, which is the ratio of estuary width over average water depth.

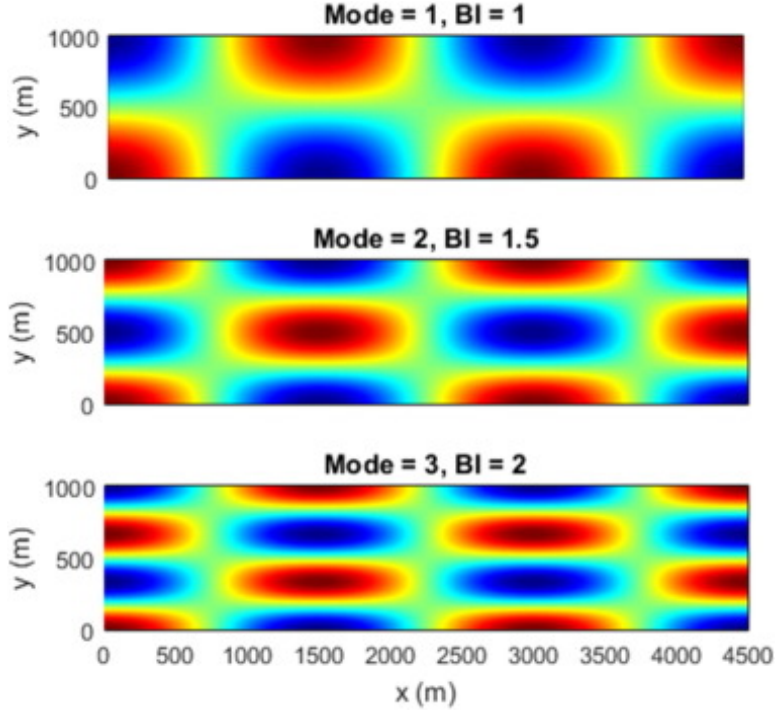


Figure 2: Illustration of different bar modes in a channel. BI stands for braiding index, which is a quantity that is also used to describe bars, and is linearly related to bar mode. Figure by Leuven et al (2016).

In the literature many potential important factors that determine bar shapes and dimensions have been identified, examples include: estuary width, the aspect ratio, current velocity, tidal period, estuary geometry and tidal asymmetry. To summarize, a few important general findings¹⁷ are listed below.

- Bar height is linearly related to local water depth.
- Bar length is best correlated with estuary width.
- Bar length can be (and is often) shorter than the tidal excursion length.
- Bar width increases with estuary width. However, bar width reduces when a higher bar mode (m) is reached.

Current velocity may also be important for bar shape and dimensions. However, according to observations,¹⁷ bar length is independent of current velocities for current velocities in the range of 0.8 to 1.2 ms^{-1} . Except for that specific range of velocities, bar length increases with current velocities. On the other hand, bar length correlates for the full range of current velocity with estuary width: $L = 0.97 W^{0.87}$. However, in particular for narrow estuaries, predicted theoretical bar length by Schramkowski et al. (2002) cannot match observations.¹⁷ Especially for increasingly more narrow estuaries, theory overpredicts bar length by an order of magnitude. In figure 3 the difference between theoretical and observed values is expressed as a fraction of theoretical and observed values. This fraction is plotted against both estuary width and the aspect ratio (width over depth). For both bar length and width in relation to estuary width and the aspect ratio the differences between theory and observations are visualized. In any case, there is a large spread and almost always theory overpredicts bar length.

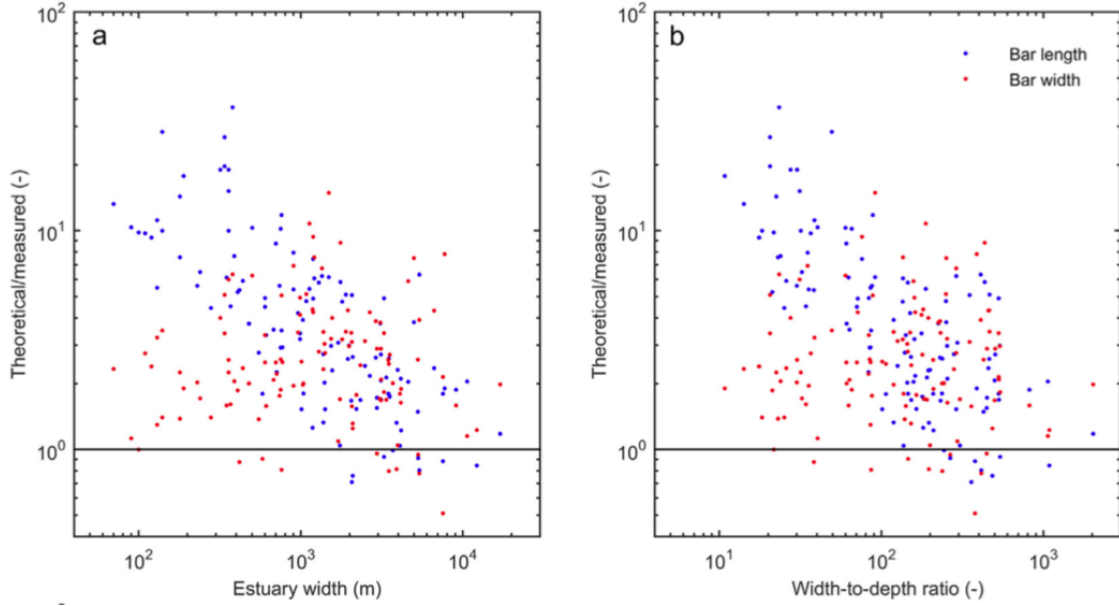


Figure 3: Theoretical bar length divided by observed bar length for different estuarine widths. In particular the large error for narrow estuaries and the enormous spread are remarkable. Figure by Leuven et al (2016).

Currently, theories use a mathematical tool called linear stability analysis to analyze the development of tidal sand bars. Linear stability analysis provides¹⁰ knowledge on sand bar appearance and characteristics i.e. wavelength and migration speed. As a starting point, a morphodynamic equilibrium state (or basic state) is defined with a simplified geometry and or topography. Subsequently, a small spatially periodic perturbation is applied to the bedprofile. This in turn leads to perturbations in the velocity field and water level. Eventually, depending on the perturbation wavelength, growth or decay occurs. By assuming the perturbation to be small, the problem can be linearized. As a consequence, this limits the applicability of linear stability analysis to the initial stage of the sand bar development. However, the perturbation with the wavelength that has the highest growth rate, the fastest growing mode (FGM), is still assumed to become dominant.

2.2 Hydrodynamics in estuaries

Estuaries can be classified based on the dominant hydrodynamic forcing: tide dominated, wave dominated or river dominated. In this project, we focus on sediment transport solely due to tide, therefore the estuary considered in this project is fully tide dominated. For tide dominated estuaries, rivers are of minor importance and are not implemented in the hydrodynamical model. By considering river input to be negligible, it follows that this particular estuary type is well-mixed, i.e. a constant density is assumed. Hence, density driven circulations cannot be resolved by this hydrodynamical model. In fact, density stratification is another often used classification type, in this case: a well-mixed estuary. Another assumption that characterizes the estuary to be investigated, is that the geometry is approximated by a very simple rectangular model domain, see figure 4.

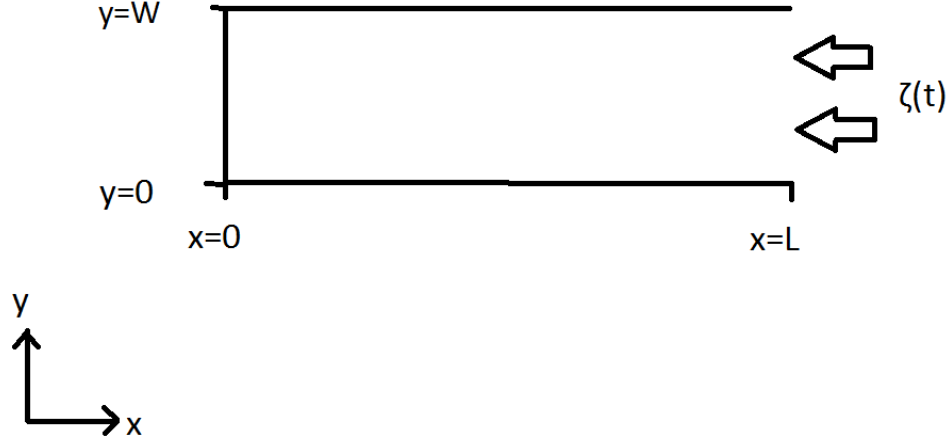


Figure 4: Schematized view of the domain used in the numerical model, basically a rectangular domain. Length L and width W have to be specified.

On this domain, a simplified version of the Navier Stokes equation is solved. Starting from the Navier Stokes equations and assuming a hydrostatic pressure distribution, the governing equations become:

$$\frac{\partial}{\partial t}(\rho u) + \frac{\partial}{\partial x}(\rho u^2) + \frac{\partial}{\partial y}(\rho uv) + \frac{\partial}{\partial z}(\rho uw) - \rho fv + \frac{\partial p}{\partial x} - \frac{\partial \tau_{xx}}{\partial x} - \frac{\partial \tau_{xy}}{\partial y} - \frac{\partial \tau_{xz}}{\partial z} = 0 \quad (2)$$

$$\frac{\partial}{\partial t}(\rho v) + \frac{\partial}{\partial x}(\rho uv) + \frac{\partial}{\partial y}(\rho v^2) + \frac{\partial}{\partial z}(\rho vw) + \rho fu + \frac{\partial p}{\partial y} - \frac{\partial \tau_{yx}}{\partial x} - \frac{\partial \tau_{yy}}{\partial y} - \frac{\partial \tau_{yz}}{\partial z} = 0 \quad (3)$$

$$\frac{\partial u}{\partial x} + \frac{\partial v}{\partial y} + \frac{\partial w}{\partial z} = 0, \quad \frac{\tau_{ij}}{\rho} = \nu \left(\frac{\partial u_i}{\partial x_j} + \frac{\partial u_j}{\partial x_i} \right), \quad \frac{\partial p}{\partial z} + \rho g = 0. \quad (4)$$

For the purpose of a conceptual model, we used a relatively simple set of equations, without neglecting essential processes. In order to simplify, a scale analysis was used to identify the relative importance of each term. Since this research is applied to estuaries, the shallow water equations are the governing equations. By using scaling arguments we can assume⁴ lateral friction to be negligible compared to bottom friction. Firstly, define dimensionless variables:

$$x = x_*/L \quad y = y_*/L \quad z = z_*/H \quad u = u_*/U \quad v = v_*/U.$$

As an example, the viscous terms are made dimensionless: (equation 5 in the x-component of the momentum equation, equation 2)

$$\nabla^2 u = \frac{U}{L^2} \frac{\partial^2 u}{\partial x^2} + \frac{U}{L^2} \frac{\partial^2 u}{\partial y^2} + \frac{U}{H^2} \frac{\partial^2 u}{\partial z^2}. \quad (5)$$

In case of estuaries, horizontal length scales are much larger than vertical length scales: $L \gg H$. Hence, as can be observed from equation 5, lateral friction can be ignored. Furthermore, as already mentioned, density effects are ignored because the estuary is classified as well-mixed. Other notable assumptions are:

- Wind shear stress is ignored.
- Incompressible fluid
- Constant viscosity

- Quadratic bottom stress parametrization

Furthermore, whether Coriolis force is dynamically important or not, can be determined by evaluating the Rossby deformation radius L_R . If the width of the estuary (or basin), W , is small compared to this radius, Coriolis force may in fact be neglected, where $W \ll L_R$.

$$L_R = \frac{\sqrt{gH}}{f} \quad (6)$$

For this project, shallow seas will be considered, i.e. estuaries. Whether or not a sea can be characterized as 'shallow' can be decided by considering horizontal (L) and vertical length scales (H). If $H \ll L$ a sea can be called shallow. In this case L is of the order of 100 km, while a typical water depth is 10 m. The flow for a domain where $H \ll L$ can be described as a boundary layer type of flow.³⁷ Hence, hydrodynamics are assumed to be uniform throughout the water column. This allows the use of depth averaged horizontal velocity components, equations 2 and 8.

$$\bar{u} = \frac{1}{H} \int_{-H}^{\zeta} u dz \quad (7)$$

$$\bar{v} = \frac{1}{H} \int_{-H}^{\zeta} v dz \quad (8)$$

Using these definitions of depth averaged horizontal velocity components and dropping the overbars, the final form of equations 2 and 3, is:

$$\frac{\partial u}{\partial t} + u \frac{\partial u}{\partial x} + v \frac{\partial u}{\partial y} = -g \frac{\partial \zeta}{\partial x} - \frac{1}{\rho H} \tau_{xb} \quad (9)$$

$$\frac{\partial v}{\partial t} + u \frac{\partial v}{\partial x} + v \frac{\partial v}{\partial y} = -g \frac{\partial \zeta}{\partial y} - \frac{1}{\rho H} \tau_{yb} \quad (10)$$

$$\frac{\partial(uH)}{\partial x} + \frac{\partial(vH)}{\partial y} + \frac{\partial H}{\partial t} = 0. \quad (11)$$

However, the vertical component of the bottom stress still has to be specified. As already mentioned, scaling arguments were used to establish dominance of bottom friction over lateral friction. Bottom friction is the result of boundary conditions in 3D flow,³⁷ hence bottom friction has to be parametrized since only a 2D model is used. In a linear vectorized form bottom friction is described by:

$$\boldsymbol{\tau}_b = \rho r \mathbf{u} \quad r = \frac{8}{3\pi} C_d U_{max}. \quad (12)$$

This parametrization is often not used, instead a quadratic dependence on the depth averaged velocity is adopted:

$$\boldsymbol{\tau}_b = \rho C_d \mathbf{u} |\mathbf{u}|. \quad (13)$$

Vreugdenhil (1994) explained that a quadratic parametrization is used because it is related to turbulent boundary layer theory. A characteristic value for the drag coefficient is $C_D = 10^{-3}$ and this value will be used in all computations for this project. Nevertheless, the linear friction law is still consistent with the quadratic formulation in the sense of energy dissipation.⁴¹

2.3 Residual velocity and vorticity

As can be expected from the shallow water equations, depth variations induce variations in the velocity field. These variations persist through time and result in residual currents. When considering a spatially periodic bottom perturbation on a flat bedprofile, this results in residual circulation cells due to nonlinear terms in the momentum equations. Mathematically, the velocity field can be described in a very general way by a superposition of many spatially and time dependent components:

$$\begin{aligned} u &= R_u + A(t) \sin \pi x \cos \pi y \\ v &= R_v - A(t) \sin \pi y \cos \pi x. \end{aligned} \quad (14)$$

The subscript u, v indicates which vector component is involved (R is a vector). For scaling of these equations, a typical length scale is the perturbation length scale L_E was taken²³ and for time the tidal period T . In equation 14, R represents a spatially homogeneous tide (including all tidal harmonics and the residual (0) component), with $R = R_0 + R_1(t) + R_2(t) + \dots$. Additionally, A with $A = A_0 + A_1(t) + A_2(t) + \dots$ represents oscillatory eddies of the basic tide, A_1 and the residual A_0 and harmonic components A_2, A_3, \dots , caused by fluctuations in the bottom topography. To illustrate the first order behaviour of the velocity field, this set of equations can be heavily truncated. Retaining only the components R_1 and A_0 , as was done by Beerens et al. (1994), the set of equations become:

$$\begin{aligned} u &= \pi \lambda \nu \Psi_y(x, y) + \pi \lambda \cos(2\pi t) \\ v &= -\pi \lambda \nu \Psi_x(x, y) \end{aligned} \quad (15)$$

with the streamfunction defined as $\Psi(x, y) = \frac{1}{\pi} \sin(\pi x) \sin(\pi y)$ and subscripts indicating derivatives. Flow is assumed to be incompressible, essentially meaning that it is volume preserving. A volume preserving system is characterized as a Hamiltonian system, with the streamfunction acting as the Hamiltonian. In this case, this type of system is a strongly perturbed Hamiltonian system. This system of equations is a simplification²³ of the system given by equation 14.

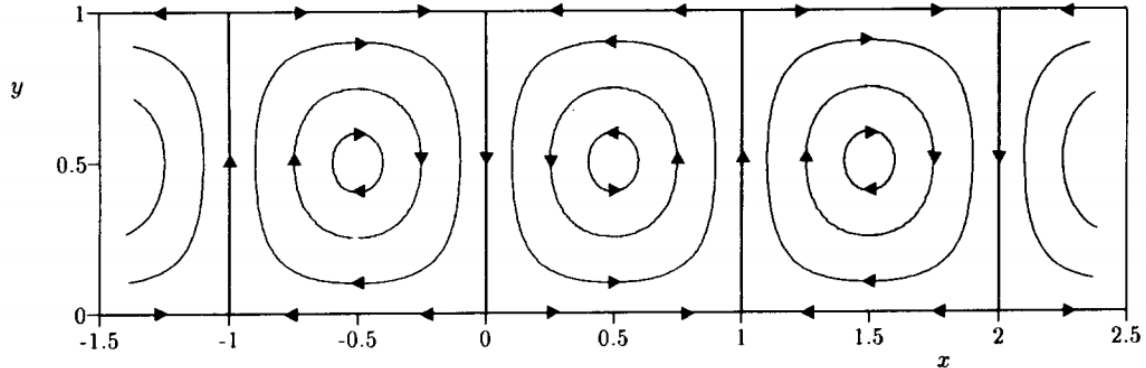


Figure 5: Schematized view of residual eddies represented by the streamfunction in equation 15, as was made by Beerens et al. (1994).

Non-dimensionalizing the velocity field yields two important parameters that determine particle trajectories (phase-space of the system), which are:

$$\lambda = \frac{L_T}{L_E} = \frac{\text{tidal excursion}}{\text{eddy diameter}} , \quad \nu = \frac{u}{U} = \frac{\text{velocity in residual eddies}}{\text{tidal velocity amplitude}} \quad (16)$$

To simulate the movement of sub-volumes (now called particles), the kinematic equations are solved. The accompanying kinematic model⁵ for tidal flow becomes :

$$\begin{aligned}\frac{dx}{dt} &= \pi\lambda\nu\Psi_y(x, y) + \pi\lambda\cos(2\pi t) \\ \frac{dy}{dt} &= -\pi\lambda\nu\Psi_x(x, y)\end{aligned}\tag{17}$$

A visualization of the phase-space of this dynamical system is built by creating the positions of some particles stroboscopically (once every tidal period) and is called a tidal map. This tidal map indicates the tide averaged net movement of (small) particles through space. A tidal map is often characterized by trapped regions and mixing regions.⁵ Regions where particles theoretically remain forever are called trapped regions, on the other hand mixing regions are characterized by chaotic particle trajectories. Chaotic stirring in time-periodic flows can therefore significantly contribute to horizontal dispersion. Since this system is technically still a (perturbed) Hamiltonian system, this type of Lagrangian chaos is volume preserving. Mathematically seen, hyperbolic points of the residual velocity field, such as (0,0), (1,0), (0,1) and (1,1) in figure 5, are associated with these mixing regions while elliptic points are associated with trapped regions. In this case, see figure 5, with a residual velocity field in the form of residual circulation cells, hyperbolic points are located in the corners of such cells. On the other hand, elliptic points are located in the centre of these circulation cells. In figure 6 chaotic regions can be observed around these hyperbolic points, while elliptic points are surrounded by trapped regions.

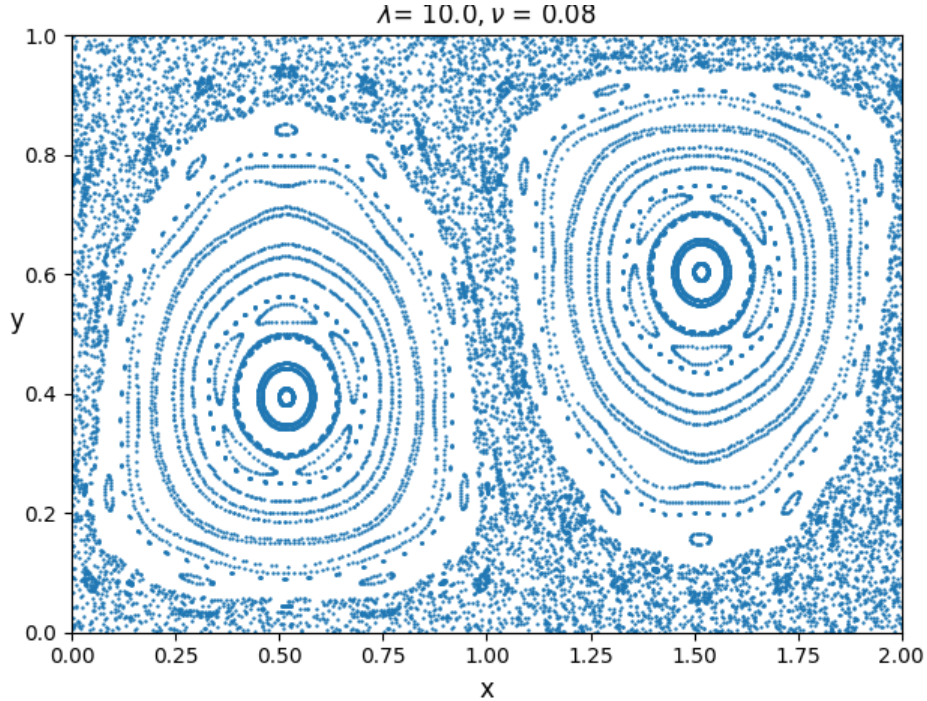


Figure 6: Visualization of the dynamical system (eq. 17) with parameter values $\lambda = 10$ and $\nu = 0.08$. This example illustrates both chaotic and trapped (i.e. clear and structured trajectories) regions. Length scales are dimensionless.

Randomness of the Eulerian velocity field is not required for particles to display chaotic behaviour. Even a time periodic and deterministic 2D velocity field allows particles to have trajectories described by random functions. While the model by Beerens et al. (1994), equation 17 - makes simplifications about the velocity field, in this project the velocity fields provided by the hydrodynamic model are more complicated. With

a free surface, local convergence or divergence is allowed, so in particular for shallow water, the particle dynamics are not Hamiltonian anymore. This furthermore implies that no streamfunction can be established that governs this more complex velocity field.

Along with residual circulation cells, a residual vorticity field exists. The vorticity equation can be derived from the depth averaged shallow water equations for 2D flow by only combining the horizontal momentum equations:

$$\frac{\partial u}{\partial t} + u \frac{\partial u}{\partial x} + v \frac{\partial u}{\partial y} - fv = -g \frac{\partial \zeta}{\partial x} + \frac{1}{\rho H} \frac{\partial}{\partial x} (H \tau_{xx}) + \frac{1}{\rho H} \frac{\partial}{\partial y} (H \tau_{xy}) - \frac{1}{\rho H} \tau_{xb} \quad (18)$$

$$\frac{\partial v}{\partial t} + u \frac{\partial v}{\partial x} + v \frac{\partial v}{\partial y} + fu = -g \frac{\partial \zeta}{\partial y} + \frac{1}{\rho H} \frac{\partial}{\partial x} (H \tau_{yy}) + \frac{1}{\rho H} \frac{\partial}{\partial y} (H \tau_{xy}) - \frac{1}{\rho H} \tau_{yb}. \quad (19)$$

The simplifying assumptions used to derive equations 9 and 10 of neglecting both Coriolis force and lateral friction are omitted because this is not necessary to derive analytical solutions for vorticity. Including Coriolis force and lateral friction, the dimensionless vorticity equation can be derived:⁴⁰

$$\partial_t \eta + \mathbf{U} \cdot \nabla \eta + \frac{r}{H} \eta = \frac{f}{H} \cdot \nabla h - \frac{r}{H^2} \mathbf{U} \times \nabla h. \quad (20)$$

Vorticity is defined as $\eta = \nabla \times \mathbf{u}$. H is a characteristic vertical scale while h represents variations in the spatially dependent topography. The tidal unperturbed velocity is indicated with \mathbf{U} and the topographically induced velocity with \mathbf{u} . The solution for the residual vorticity can be obtained^{5,40} analytically. Furthermore the topographic wavenumber is assumed to be equal for both x and y direction. From the solution it can be concluded that a maximum in the residual vorticity occurs for wavenumbers that are common for sandbars in tidal areas.⁵ This suggests that the fastest growing mode has a wavelength that corresponds to the wavelength with a vorticity maximum.

2.4 Sediment transport and bed evolution

Two different types of sediment transport exist: bed-load and suspended load transport. Bed-load transport is defined as transport of sediment by rolling, sliding and saltation. This type of sediment transport takes place in a layer close to the bottom. In this project, only fine sediment is considered, which remains in suspension. Dynamics of suspended sediment is often^{28,29,34} described using an advection-diffusion equation with a source/sink term. For depth averaged models, the concentration equation with C (unit: m) representing the volume concentration of sediment in a column of seawater per unit area, is:

$$\frac{\partial C}{\partial t} + \nabla \cdot (uC - \kappa \nabla C) = S_*. \quad (21)$$

Here u indicates the depth averaged velocity velocity field while S_* , with units m/s, represents contributions of erosion ($S > 0$) and deposition ($S < 0$). Multiplying C with sediment density yields the depth integrated mass concentration. Omitting the diffusion term and rewriting the equation using $\rho_s C / H = M/V = \hat{C}$ yields:³⁴

$$\frac{\partial \hat{C}H}{\partial t} + \nabla \cdot (u \hat{C}H) = \rho_s S_* \quad (22)$$

with H indicating the total water depth. In this equation, \hat{C} now represents a depth averaged sediment mass concentration with units kg/m³. Reworking the brackets yields:

$$H \frac{\partial \hat{C}}{\partial t} + \hat{C} \frac{\partial H}{\partial t} + \hat{C} \nabla \cdot (uH) + Hu \nabla \cdot (\hat{C}) = \rho_s S_* \quad (23)$$

and rearranging gives:

$$H \left(\frac{\partial \hat{C}}{\partial t} + u \nabla \cdot (\hat{C}) \right) + \hat{C} \left(\frac{\partial H}{\partial t} + \nabla \cdot (u H) \right) = \rho_s S_*. \quad (24)$$

In this equation, the continuity equation for shallow water can be recognized, equation 11, and hence can be omitted. Subsequently, H is moved to the right hand side:

$$\frac{\partial \hat{C}}{\partial t} + u \nabla \cdot (\hat{C}) = \rho_s \frac{S_*}{H}. \quad (25)$$

To frame this equation in a more Lagrangian form, it is rewritten to an equivalent form. For this purpose, the definition of material derivative (indicated by d/dt), which contains local and advective derivatives, is used:

$$\frac{d\hat{C}}{dt} = \rho_s \frac{S_*}{H} \quad (26)$$

Many parametrizations have been used for both erosion and deposition, ranging from empirical and engineering type to more physics based parametrizations. Source/sink terms include erosion and deposition, basically: $S_* = E - D$. Examples of older erosion-deposition parametrizations are by Partheniades (1965) and Krone's (1962) formulation for deposition. Essentially erosion scales linearly with bottom stress in these parametrizations and a critical shear stress is used for both erosion and deposition. Other similar (but nonlinear) formulations for erosion exist,¹⁹ for example in the form of $E = A(\tau_b - \tau_c)^n$ with $n= 1.5$, τ_b is the bottom stress, τ_c a threshold value for erosion to occur and A a constant. Another parametrization,³⁴ which will be used in this project, is described below. For erodible boundaries, the erosion-deposition flux S_* of volume concentration, derived by using boundary conditions,^{9,34} is:

$$S_* = w_s c_a - w_s c_0. \quad (27)$$

In equation 27, c_a is a reference concentration and c_0 represents the suspended sediment concentration at the bottom, both c_a and c_0 have yet to be specified. Additionally, an import parameter is the settling velocity w_s that emerges in the deposition-erosion flux and mainly depends on grain size.³⁵ For fine sediment (silt or very fine sand, diameter of 60 μm) the settling velocity is in the order of a millimetre per second and this value is used for all the results in this project. Furthermore, c_0 is determined by using the concept of equilibrium concentration. Sediment concentration has a vertical dependency and this structure can be obtained by solving a balance between settling and stirring (by eddies) of sediment for \hat{c} :

$$w_s \hat{c} + \kappa_v \frac{\partial \hat{c}}{\partial z} = 0. \quad (28)$$

with C the volume concentration of sediment in a column of seawater per unit area. The boundary condition at the bottom ($z = -H + h$) reads: $\hat{c} = c_0$. It is assumed that the vertical distribution of sediment in the water column remains the same, regardless of hydrodynamic conditions (stationary or transient). For simplicity, the turbulent vertical eddy diffusion coefficient κ_v (and w_s), is assumed to be constant. Using these assumptions, \hat{c} becomes:⁸

$$\hat{c} = c_0 \exp \left(\frac{w_s}{K_v} (z + H - h) \right). \quad (29)$$

Integrating \hat{c} over z yields C , the volume concentration of sediment in a column of seawater per unit area:

$$C = c_0 \frac{K_v}{w_s} \left(1 - \exp \left(-\frac{w_s}{K_v} (H + h) \right) \right) \approx c_0 \frac{K_v}{w_s}. \quad (30)$$

Here it is assumed⁸ that the thickness of the suspended layer (measured by the ratio K_v over w_s) is small compared to the total water depth. This provides a simple relation between C and c_0 according to equation

30. For the reference concentration c_a , which is determined by hydrodynamic conditions, observations¹¹ have led to the establishment of:

$$c_a = (1 - p) \frac{\gamma s}{1 + \gamma s} , \quad s = \frac{\tau - \tau_c}{\tau_c} \quad (31)$$

with $\gamma = 7.8 * 10^{-5}$ a dimensionless parameter (determined empirically) and p represents porosity of the sediment. τ is the bottom stress and τ_c is a threshold value for erosion to occur. Most sediment consists of quartz⁹ which has a density of $\rho_s = 2650 \text{ kg/m}^3$ and this density will be used throughout this report. Sediment porosity is set to $p = 0.3$. Now that the erosion-deposition flux S_* is specified, the bottom evolution equation⁸ is:

$$(1 - p) \frac{\partial h}{\partial t} + \nabla \cdot \mathbf{q}_b = -S_* \quad (32)$$

can be used to determine morphologic changes due to erosion and deposition. h represents the bedprofile, which depends on time on a morphologic timescale and \mathbf{q}_b denotes volumetric sediment transport. This equation governs the conservation of mass applied to sediment in water and describes changes in bed elevation. In this project, convergence or divergence of volumetric sediment transport in the bedload layer is ignored, $\nabla \cdot \mathbf{q}_b = 0$, because only fine sediment is considered. As already mentioned, S_* (units: m/s) describes the contributions of deposition and erosion.

2.5 Compound tides

With regards to sediment transport, residual velocity fields due to nonlinear terms are relevant to analyze. If we assume a simple tidal velocity field to be given by a tidal constituent with frequency ω , nonlinearities can give rise to both a residual part and tidal superharmonics or overtones. In other words, in addition to a residual part, oscillations with higher frequencies (a multiple of ω) are produced. This is best illustrated³⁸ by considering the 1D shallow water equations:

$$\frac{\partial u}{\partial t} + u \frac{\partial u}{\partial x} = -g \frac{\partial \zeta}{\partial x} - \frac{u|u|}{h_0} - \frac{\zeta u|u|}{h_0^2}. \quad (33)$$

In equation 33, the frictional terms are split in two parts to distinguish between the effect of depth variations and the nonlinear friction part ($|u|$ stands for the velocity vector length). Hereby it is assumed that surface variations are small compared to the total water depth. This is a Taylor series expansion and it is of second order $(\zeta/h)^2$ accuracy.

For example consider the inertial term and substitute $u(x, t) = U(x) \cos(\omega t - kx)$ with ω the forcing frequency M2. This yields after a straightforward derivation both a residual part (first term on the right hand side) and an overtide part (the other two terms on the r.h.s.), as can be observed in equation 34. In this case the overtide compound's frequency is twice the forcing frequency M2; subsequently this specific overtide compound is called M4.

$$u \frac{\partial u}{\partial x} = \frac{1}{2} U \frac{\partial U}{\partial x} + \frac{1}{2} U \frac{\partial U}{\partial x} \cos 2(\omega t - kx) + \frac{1}{2} U^2 k \sin 2(\omega t - kx) \quad (34)$$

For a derivation of the interaction between two different modes, the reader is referred to Wang et al.(1999). The derivation of the effect of the frictional terms is more difficult but eventually they also produce a residual part. Furthermore frictional terms contribute multiples of the main frequency, especially M6 and to a lesser extent M4. To the lowest order approximation, the contribution of $u|u|$ is $\frac{1}{2} + \frac{1}{2} \cos 2\omega t$, For details about the derivation of the interaction between different modes and the influence of friction, see Wang et al.(1999). Compound tides cause the tide to be asymmetric. Effects of tidal asymmetry on sediment transport are twofold, since sediment transport can be distinguished in two types: bed load transport and suspended load transport. In this project, a depth averaged concentration is used, in this sense sediment transport can be viewed as suspended load transport. To this end, only the settling lag mechanism for suspended load

transport is discussed here. When compared to bed load transport, suspended load transport has more subtle dynamics.¹³ As mentioned before, bottom friction and nonlinear interactions between tidal forcing and topography generate over tides, for example M_4 and M_6 . The resulting velocity curve can be asymmetric, depending on the relative phase³³ of the over tides compared to M_2 . This asymmetric nature is important to sediment transport, both for bed load and suspended sediment transport. Retaining only M_2 and its first overtide M_4 , the tidal current can be formulated as:

$$u(t) = u_2 \cos(\omega t) + u_4 \cos(2\omega t - \beta). \quad (35)$$

Here β determines whether or not the velocity curve becomes asymmetric and additionally, β also determines strength and duration of both ebb and flood. Last but not least, it also determines the duration of high and low water slack. In figure 7 the velocity curve corresponding to the superposition of the contribution of M_2 and M_4 to the tidal current is depicted. Even though the maximum of ebb and flood velocities is equal, the velocity curve is not symmetrical due to a difference in (high and low water) slack time. During high water slack (at $t=T/2$) sediment has more time to settle, while during low water slack (at $t=0$) this is not the case due to a rapid transition towards high water. This implies that when high water comes up, a relatively large part of the sediment is still in the water column. The consequence is in this case net transport in the direction of the flood current. This mechanism is described as temporal settling lag.

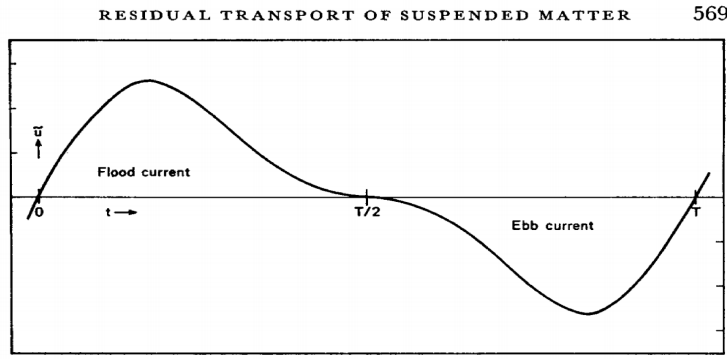


Fig. 1. Time variation of the effective current velocity $\bar{u} = A (2 \sin \omega t + \sin 2 \omega t)$. The current velocity scale is arbitrary.

Figure 7: Groen (1967) used this graph to illustrate tidal asymmetry due to differences in high and low water slack time.

In addition, even without tidal asymmetry a net transport of sediment can occur due to a spatial settling lag mechanism. This behaviour can be derived²⁷ by starting from the (1D) concentration equation:

$$\frac{\partial C}{\partial t} + \frac{\partial uC}{\partial x} = \alpha u^2 - \beta C \quad (36)$$

with the right-hand side describing respectively erosion and deposition. The first step is to make an assumption about the structure of the velocity: $u = U(x) \cos(\omega t)$. Neglecting advection, the tidally averaged net transport follows²⁷ from time averaging (tidal average):

$$\langle uC \rangle = -\frac{3}{4} \frac{\alpha}{\beta} U^3 \frac{du}{dx} F(a), \quad F(a) = \frac{a}{1+a^2} \left(1 + \frac{11-2a^2}{21+4a^2}\right) \quad (37)$$

with settling lag parameter a being the fraction of the deposition timescale (measured by β) and the tidal period. F solely depends on this settling lag parameter but in any case $F \geq 0$. From equation 37 it follows that a net transport of sediment occurs towards areas of small tidal amplitudes. If the current flows towards areas with a decreasing tidal current (flood), local sediment concentration will increase in that area,^{9,27} i.e. convergence of sediment occurs. During the opposite tidal phase (ebb), sediment is transported away, leading

to a decrease in concentration (divergence of sediment) in this area of small tidal amplitudes. Subsequently, sediment transport during flood exceeds sediment transport during ebb, leading to a net transport towards areas with smaller tidal amplitudes.

3 Methods

The project goals require decisions for both hydrodynamical and morphological aspects. In the process of constructing the numerical model, the results need continuous verification, before proceeding and extending the model. Hence, this section is divided into two parts, namely, model description and verification.

3.1 Hydrodynamical model

Three main strategies can be distinguished regarding hydrodynamics:

- Analytical approximation of hydrodynamics
- Setting up a conceptual numerical model
- Using an existing numerical model (Delft3D)

Each method comes with advantages and limitations. In this project the second option was chosen as it provides more control compared to using an existing numerical model. As a starting point, the governing conservation equations were determined. The most relevant processes were identified by a scaling analysis. Moreover, an important reason to use an idealized depth averaged model is that important physical processes can be reproduced while avoiding complexities of 3D models and processes. Subsequently, identifying and quantifying important processes from results is also easier since 3D processes are excluded. A 3D model is computationally seen also more expensive to run and hence does not suit a relatively short term project well.

Once the decision was made to set up a conceptual model, further choices had to be made, in particular with respect to numerical methods and language. For this project, Python was selected as programming language. Several finite difference methods exist, each come with certain advantages and disadvantages. An important requirement is decent stability, which is achieved by (semi-) implicit methods rather than explicit methods. In section 4 an extensive description of the numerical methods used for the hydrodynamic model is given. Furthermore, the verification of the hydrodynamic model is presented.

3.2 Kinematic model

This part of the model requires the output of the hydrodynamic model, e.g. depth averaged velocity fields. Subsequently, velocity fields are used to integrate the kinematic equations over time yielding particle trajectories. For the numerical integration several numerical methods are available. Multiple methods were tested on their efficiency and accuracy. Afterwards, the best performing method was selected and used in any following computation. Additionally, the kinematic model was verified in various stages. As a reference, the kinematic model described in section 2 by Beerens et al. (1994) was used. See section 5 for more details.

3.3 Sediment transport model

Lastly, another part was added to the model that computes erosion, deposition, bottom evolution and incoming sediment. Deposition and erosion occur on small subgrid scales and have to be parametrized. The parametrizations of erosion and deposition used in the sediment transport model, are described in section 2. Using the numerical framework established by the aforementioned kinematic model, erosion and deposition parametrizations were implemented. An outline of the numerical implementation and the verification of this part of the model is given in section 5.

3.4 Model outline

As already explained, the numerical model consists of two coupled parts: a hydrodynamic model and a sediment transport model. As already mentioned in section 2, bathymetry influences the (residual) velocity

field. The numerical model has as input the spatially dependent bathymetry. Subsequently, the hydrodynamic model computes the currents corresponding to the initial bathymetry. Next, the sediment transport model computes erosion and deposition, leading to changes in the bathymetry. When the bottom topography changes its shape, this leads to changes in the residual velocity field. This in turn, leads to changes in sediment transport. In this way, hydrodynamics and sediment transport processes interact, which is visualized in a flow chart, figure 8.

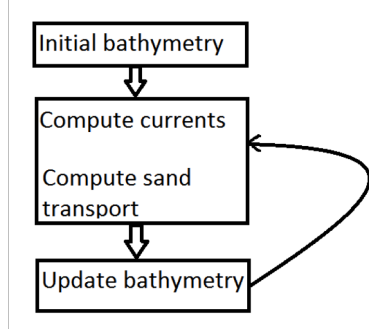


Figure 8: Flow diagram of the numerical model.

To be more precise, given an initial bathymetry, the hydrodynamic model delivers space and time dependent data, i.e. $u(x, y, t)$, $v(x, y, t)$ and $H(x, y, t)$ to the sediment transport model in the form of text files. Afterwards, the sediment transport model processes all hydrodynamic data and computes the corresponding sediment transport. If this leads to considerable changes in the bathymetry (exact threshold value is specified along with the results), the sediment transport model delivers the updated bathymetry to the hydrodynamic model. Basically this coupling involves a loop where the bathymetry is updated. The evolution of the topography can be formulated as equation 38. Indices i, j refer to a particle gridcell with location ($x_i = i \cdot dx, y_j = j \cdot dy$), k refers to the Lagrangian particle trajectories contributing to deposition at each location x_i, y_j . The bathymetry (at stage n) and hence hydrodynamics is kept fixed, until erosion and deposition contributions exceed a threshold value. If this occurs, the bathymetry is updated to stage $n + 1$, in which n is a measure of time.

$$H_{i,j,n+1} = H_{i,j,n} - E_{i,j,n} + \sum_k S_{i,j,n,k} \quad (38)$$

After the simulation has finished, data on the residual field, bathymetry and parameters are saved in the form of text files. Depending on the simulation type, additional data are saved: particle trajectories and perturbation growth or decay rates.

4 Hydrodynamic model

In this section an outline of the hydrodynamic model and all numerical aspects involved is presented. This includes a description of the exact discretization procedure, the grid, boundary conditions and the verification of this model.

4.1 Computational grid

For discretization, the Arakawa C grid is used. In this model central difference is used in the interior, while at the boundaries either forward or backward differentiation is used. The use of staggered grids reduces, according to Stelling (1984), so called '2 Δx ' waves.

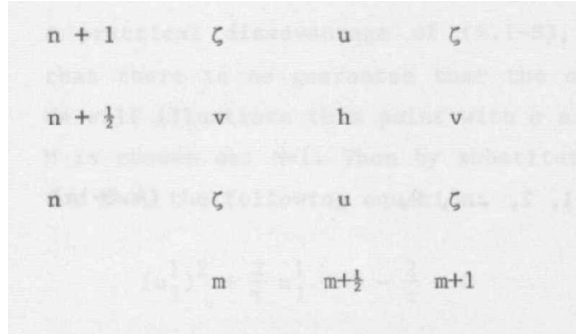


Figure 9: Staggered grid for u, v, h and regular grid for ζ , as was used in Stelling (1984).

4.2 Alternating direction implicit method

The shallow water equations are classified as nonlinear hyperbolic partial differential equations, implying that solutions are wave-like. If these type of equations are explicitly solved, one has to limit timestep-size in order to avoid instabilities. The numerical solution can be achieved by means of different finite difference methods (FDM), which can be characterized as either explicit, semi-implicit or fully implicit. One of the benefits of implicit methods is that (greater) numerical stability is obtained. Some examples of implicit methods are Crank Nicholson and Alternating direction implicit method(ADI). ADI methods are popular because tridiagonal matrices are involved, which can be inverted very efficiently using the Thomas algorithm (see Appendix). For this project a rectangular spatial region is used, which justifies¹² the choice of an Alternating Direction Implicit method (ADI). As explained later in this section, this is a very efficient method. The ADI procedure of solving the shallow water equations was first proposed by Leendertse (1967). Afterwards, more sophisticated (and complicated) versions of his method have been introduced. However, to serve the project goals best, more complicated numerical methods proposed by Stelling (1984) are avoided. Stelling basically extended the ADI method by Leendertse (1967) and treats the advective terms in a more implicit way. Eventually, the so- called WAQUA and Cyclic method were developed to handle horizontal advective terms even fully implicitly. To this end iterations are required. The numerical model Delft3D makes use of the same but extended ADI method and additionally incorporates the WAQUA and Cyclic method. Delft3D is a well known model that is used for computations of sediment transport and hydrodynamics and applied to coastal and estuarine environments. Below the set of equations proposed by Leendertse is repeated here for convenience. This set of equations is used for the numerical solution of the shallow water equations in this project.

$$- \text{Stage 1: } t + \frac{1}{2} \Delta t -$$

$$u^{n+\frac{1}{2}} = u^n + \frac{1}{2} \Delta t f v^n - \frac{1}{2} \Delta t u^{n+\frac{1}{2}} \frac{\partial u^n}{\partial x} - \frac{1}{2} \Delta t v^n \frac{\partial u^n}{\partial y} - \frac{g \Delta t}{2} \frac{\partial \zeta^{n+\frac{1}{2}}}{\partial x} - r u^{n+\frac{1}{2}} \quad (39)$$

$$v^{n+\frac{1}{2}} = v^n - \frac{1}{2} \Delta t f u^{n+\frac{1}{2}} - \frac{1}{2} \Delta t u^{n+\frac{1}{2}} \frac{\partial v^n}{\partial x} - \frac{1}{2} \Delta t v^{n+\frac{1}{2}} \frac{\partial v^n}{\partial y} - \frac{g \Delta t}{2} \frac{\partial \zeta^n}{\partial y} - r v^{n+\frac{1}{2}} \quad (40)$$

$$\zeta^{n+\frac{1}{2}} = \zeta^n - \frac{\partial(Hu)}{\partial x}^{n+\frac{1}{2}} - \frac{\partial(Hv)}{\partial y}^n \quad (41)$$

- Stage 2: $t + dt$ -

$$u^{n+1} = u^{n+\frac{1}{2}} + \frac{1}{2} \Delta t f v^{n+1} - \frac{1}{2} \Delta t u^{n+1} \frac{\partial u^{n+\frac{1}{2}}}{\partial x} - \frac{1}{2} \Delta t v^{n+1} \frac{\partial u^{n+\frac{1}{2}}}{\partial y} - \frac{g \Delta t}{2} \frac{\partial \zeta^{n+\frac{1}{2}}}{\partial x} - r u^{n+1} \quad (42)$$

$$v^{n+1} = v^{n+\frac{1}{2}} - \frac{1}{2} \Delta t f u^{n+\frac{1}{2}} - \frac{1}{2} \Delta t u^{n+\frac{1}{2}} \frac{\partial v^{n+\frac{1}{2}}}{\partial x} - \frac{1}{2} \Delta t v^{n+1} \frac{\partial v^{n+\frac{1}{2}}}{\partial y} - \frac{g \Delta t}{2} \frac{\partial \zeta^{n+1}}{\partial y} - r v^{n+1} \quad (43)$$

$$\zeta^{n+1} = \zeta^{n+\frac{1}{2}} - \frac{\partial(Hu)}{\partial x}^{n+\frac{1}{2}} - \frac{\partial(Hv)}{\partial y}^{n+1} \quad (44)$$

This scheme allows a fluent switch between linear and nonlinear bottom stress. If a nonlinear bottom stress law is used, then r effectively becomes a function of the velocity itself. Nevertheless this does not involve any additional computations or considerable change of the discretized equations. If r is linear (eq. 12), it is a just a prescribed value (see literature review section). In case of nonlinear friction, r will be treated explicitly according to equation 13. In that case, to compute the length of the velocity vector, values for the velocity components on the previous timestep are used, both of which are already known. Therefore the finite difference equations still remain linear even though the bottom stress is nonlinear, because the bottom stress uses velocity components from the previous timestep or stage. Even though linear friction can easily be adopted, in this project always nonlinear bottom stress is used.

Note that the total water depth H is a superposition of a reference depth, H_0 , bathymetry variations, $H'(x, y)$ and sea surface variations: $\zeta(x, y, t)$, yielding $H(x, y, t) = H_0 + H'(x, y) + \zeta(x, y, t)$.

In the first stage the u-momentum equation and the continuity equation are solved simultaneously, leading to an equation with a tridiagonal matrix. This equation is obtained by substituting respectively the u-momentum equation in the continuity equation during the first stage while in the second stage the v-momentum equation is substituted in the continuity equation. This procedure is also used in Delft3D, for an extensive description of this procedure, see Stelling (1984). In the Delft3D model this is even more extended, for example iterations are added and advective terms can be treated fully implicitly.

$$a_{s=1} \zeta_{i-1,j}^{n+\frac{1}{2}} + b_{s=1} \zeta_{i,j}^{n+\frac{1}{2}} + c_{s=1} \zeta_{i+1,j}^{n+\frac{1}{2}} = d_{s=1}^n \quad (45)$$

$$a_{s=2} \zeta_{i,j-1}^{n+1} + b_{s=2} \zeta_{i,j}^{n+1} + c_{s=2} \zeta_{i,j+1}^{n+1} = d_{s=2}^{n+\frac{1}{2}} \quad (46)$$

Equations 45 and 46 can be written in matrix and vector notation: $\mathbf{Ax} = \mathbf{b}$. Subscript 1,2 indicates the stage wheras i,j refers to the computational grid. Using the Thomas algorithm, this equation can be effectively solved in $\mathcal{O}(n)$ operations while Gaussian elimination requires $\mathcal{O}(n^3)$ operations. In equations 45 and 46 the right hand side indicated with d consists of variables u, v, ζ at the previous stage, see as an example the right hand side for the first stage :

$$d_1 = \zeta_{i,j}^n - \frac{\Delta t}{2 \Delta x} \left[\frac{H_{i+\frac{1}{2}}(u_{i+\frac{1}{2}}^n - \bar{v}^n \frac{\Delta t}{4\Delta y}(u_{j+1}^n - u_{j-1}^n) - f \frac{\Delta t}{2} \bar{v}^n)}{1 + r \frac{\Delta t}{2} + \frac{\Delta t}{4\Delta x}(u_{i+1\frac{1}{2}}^n - u_{i-\frac{1}{2}}^n)} - \frac{H_{i-\frac{1}{2}}(u_{i-\frac{1}{2}}^n - \bar{v}^n \frac{\Delta t}{4\Delta y}(u_{j+1}^n - u_{j-1}^n) - f \frac{\Delta t}{2} \bar{v}^n)}{1 + r \frac{\Delta t}{2} + \frac{\Delta t}{4\Delta x}(u_{i+\frac{1}{2}}^n - u_{i-1\frac{1}{2}}^n)} - \right. \\ \left. \frac{\Delta t}{2} \left(\frac{v_{j+\frac{1}{2}} H_{j+\frac{1}{2}} - v_{j-\frac{1}{2}} H_{j-\frac{1}{2}}}{\Delta y} \right) \right] \quad (47)$$

with \bar{v} representing an average of all four gridpoint v -values surrounding $u_{i,j}$. The coefficients a, b, c depend on the variables u, v of the previous stage and are formulated in equations as an example for the first stage in equations 48, 49 and 50. a, b and c essentially make up the diagonals of the three-diagonal matrix (figure 10).

$$a_i = \frac{KH_{i-\frac{1}{2}}}{1 + r \frac{\Delta t}{2} + \frac{\Delta t}{4\Delta x}(u_{i+\frac{1}{2}}^n - u_{i-1\frac{1}{2}}^n)} \quad (48)$$

$$b_i = 1 + \frac{KH_{i-\frac{1}{2}}}{1 + r \frac{\Delta t}{2} + \frac{\Delta t}{4\Delta x}(u_{i+\frac{1}{2}}^n - u_{i-1\frac{1}{2}}^n)} + \frac{KH_{i+\frac{1}{2}}}{1 + r \frac{\Delta t}{2} + \frac{\Delta t}{4\Delta x}(u_{i+1\frac{1}{2}}^n - u_{i-\frac{1}{2}}^n)} \quad (49)$$

$$c_i = \frac{KH_{i+\frac{1}{2}}}{1 + r \frac{\Delta t}{2} + \frac{\Delta t}{4\Delta x}(u_{i+1\frac{1}{2}}^n - u_{i-\frac{1}{2}}^n)} \quad (50)$$

With $K = \frac{g\Delta t^2}{4\Delta x^2}$. For the second stage, these diagonals look similar, the main difference being that instead of the u velocity component the v component is used.

$$A = \begin{pmatrix} b_1 & c_1 & & \emptyset \\ a_2 & b_2 & \ddots & \\ \ddots & \ddots & c_{k-1} & \\ \emptyset & a_k & b_k & \end{pmatrix}$$

Figure 10: Matrix A in $Ax = b$ with only three non-zero diagonals.

4.3 Boundary conditions

While in the interior often central difference methods are used, close to the open boundary this is avoided. Changing central difference method is theoretically not always necessary.³⁰ However, in practice, this might produce artificial boundary layers or even instabilities. This is the case when discretization is unaltered near the boundary and variables at the boundaries (which are zero) are included in computations. In the hydrodynamic model two types of boundaries exist: one open boundary and three closed boundaries.

4.3.1 Closed boundaries

As is stated in the project goals, the aim is to investigate morphologic features in estuaries with simple geometries, for example rectangular geometries. The allowed degree of complexity in the input, i.e. input of geometry, largely determines the complexity of the closed boundary conditions. Particularly for irregular geometries, this requires extensive work on the boundary conditions. For simplicity, a very basic discretization is used: either forward or backward Euler such that the variable value at the boundary is not used by the discretized shallow water equations. Using this variable values at the boundary should be avoided.³⁰

4.3.2 Open boundary

Specification of all three variables at the open boundary is less straightforward. Since the model is forced at the open boundary, this controls the quality of the model solution. Moreover, if one fixes all variables at the open boundary, the model becomes over-specified. This implies that the specified variables at the open boundary are not coherent with the interior. Nevertheless several strategies have been proposed to treat this problem at the open boundary. A number of main strategies can be distinguished:^{3,20,30}

- fix u, v at $x = L$
- fix ζ at $x = L$
- Flather condition
- Riemann invariants
- QH discharge boundary
- Radial inflow
- Radiation boundary conditions

The Flather condition prescribes the longitudinal velocity component by removing deviations from the tidally induced current velocity. While several options may work as well, the straightforward second option is selected for this project. In the numerical model the tidal forcing is applied at the boundary ($x = L, y$). For simplicity, only one tidal constituent, M2, is used in the model, hence $N = 1$ in the following equation:

$$\zeta(t) = \sum_{j=1}^N \zeta_j \cos(\sigma_j t). \quad (51)$$

In order to improve stability of the hydrodynamical model, the discretization scheme proposed by Stelling (1984) is used and repeated for convenience:

$$\text{if } u_{i=nx-\frac{1}{2}} > 0 : u \frac{\partial u}{\partial x} = u_{i-\frac{1}{2}} \frac{u_{i-\frac{1}{2}} - u_{i-1\frac{1}{2}}}{\Delta x} \quad \text{if } u_{i=nx-\frac{1}{2}} \leq 0 : u \frac{\partial u}{\partial x} = 0 \quad (52)$$

$$\text{if } u_{i=nx-1\frac{1}{2}} > 0 : u \frac{\partial u}{\partial x} = u_{i-1\frac{1}{2}} \frac{u_{i-1\frac{1}{2}} - u_{i-2\frac{1}{2}}}{\Delta x} \quad \text{if } u_{i=nx-1\frac{1}{2}} \leq 0 : u \frac{\partial u}{\partial x} = u_{i-1\frac{1}{2}} \frac{u_{i-\frac{1}{2}} - u_{i-1\frac{1}{2}}}{\Delta x} \quad (53)$$

index i corresponds to x, and i=nx corresponds to the open boundary. In figure 11 the computational grid is shown to clarify where the discretization for u is changed.

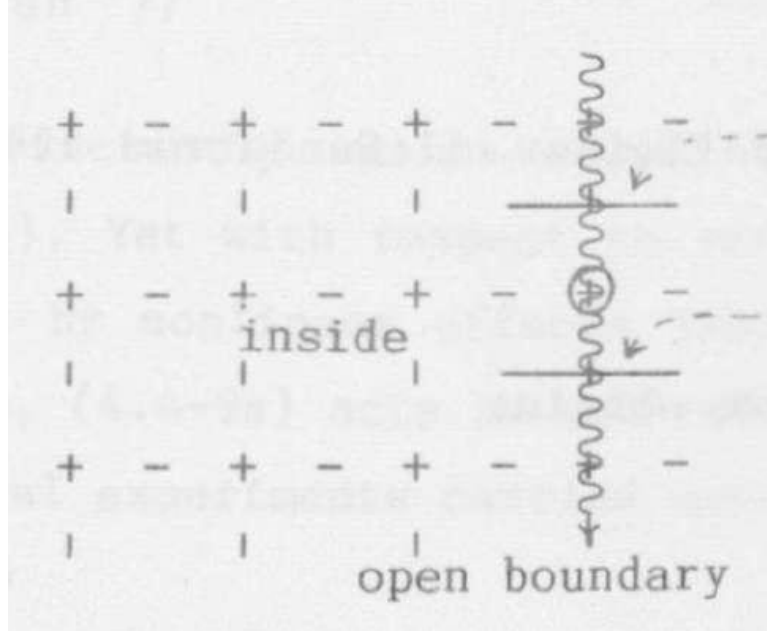


Figure 11: Grid in the vicinity of the open boundary, which is located at $i=nx$. The small horizontal lines indicate the location where u is computed. At $i=nx-1/2$ and $i=nx-1\frac{1}{2}$ the discretization scheme for u proposed by Stelling (1984) is used.

4.4 Initial conditions

By default, $u(x, y, t = 0) = 0, v(x, y, t = 0) = 0$ and $\zeta(x, y, t = 0) = 0$ is used as initial condition. The hydrodynamic model spin up always uses this as initial condition.

4.5 Model input and output

The hydrodynamic model is imported in the Main file and can be run by a single line by specifying the following:

- $\Delta x, \Delta y, \Delta t$
- Tidal forcing amplitude
- Domain length L, domain width W
- Bedprofile H(x,y)
- Output frequency

Output consists of text files containing data of the velocities u, v and surface elevation ζ on staggered grids during one single tidal period. Before starting the simulation, the output frequency of data can be specified (either every 5 or every 15 minutes). After the model spin-up is concluded, the model runs for one more tidal period and saves the aforementioned variables to a folder.

4.6 Comments on stability, accuracy and consistency

In this project the method proposed by Leendertse is used since this offers a relatively stable method.^{16,37} This ADI-method is second order accurate in space and only first order time accuracy. Nevertheless, they

mentioned that a proof of unconditional stability does not exist, this is only the case for a more simplified version of the shallow water equations. Thus before embarking on particle tracking and sediment transport processes, it is necessary to evaluate the limitations of the model with respect to grid size, timestep and water depth. A less favourable combination of the aforementioned model parameters may lead to inferior hydrodynamic results. Since particle trajectories can be very sensitive to small changes in position or velocity, it is important to consider this. When it comes to describing the (dis-)advantage of a numerical model, three important definitions of numerical concepts^{1,39} are used:

Consistency: a finite difference method (FDM) is consistent if the truncation error vanishes in the limit of the gridsize or timestep going to zero. This is the case if the scheme has at least a first order approximation. If the truncation error vanishes, the numerical solution approaches the true P.D.E solution.

Stability: if the errors (truncation error and round-off error) decay or are at least not amplified proceeding to the next timestep, then the FDM is considered to be stable.

Convergence: convergence (approaching of the P.D.E by the numerical solution) is achieved by the FDM if it is consistent and furthermore also stable.

These concepts are used in the following part of this section. As mentioned in section 'Boundary conditions', the discretization scheme for the open boundary proposed by Stelling (1984) is used. Stelling stated about this scheme that it only provides a zero order consistent approximation of the momentum equations close to the open boundary. Furthermore it yields first order convergence. Hence, the open boundary discretization can be considered a weak part of the hydrodynamic model. Increasing timestep size leads to problems at the open boundary. Secondly, another weak part is that advective terms are not time-centered: these terms are not treated fully implicitly. Since this project focuses on long waves in coastal waters, these terms are expected to have a small magnitude, justifying that they are not treated fully implicitly. This is completely in line with idea behind the model, to keep it relatively simple but well suited for the main purpose: tidal sediment transport in estuaries. However, this approximation of these advection terms may still allow instabilities to occur^{21,30}. In order to monitor model convergence, the root mean square difference between the velocity field (u -component) at different integer multiples of a tidal period is computed and added as solver output, see equation 54. A lower and upper RMSD bound can be specified, the upper bound is implemented to force the model to quit running if it becomes unstable, while the lower bound decides the degree of convergence.

$$RMSD = \sqrt{\frac{\sum_{i=0}^{nx} \sum_{j=0}^{ny} (u_{ij}^{T+1} - u_{ij}^T)^2}{nx \cdot ny}} \quad (54)$$

If the model tends to converge to a dynamic state, the RMSD approaches zero. Nevertheless, inaccuracies close to the open boundary can occur even though numerical stability is achieved. In figure 12 and 13 it is illustrated for different timesteps what happens with the velocity patterns close to the open boundary. In general taking smaller timesteps (partly) removes oscillations close to the open boundary. This makes sense, since a small timestep allows the model solution for the interior to adapt to the forcing.

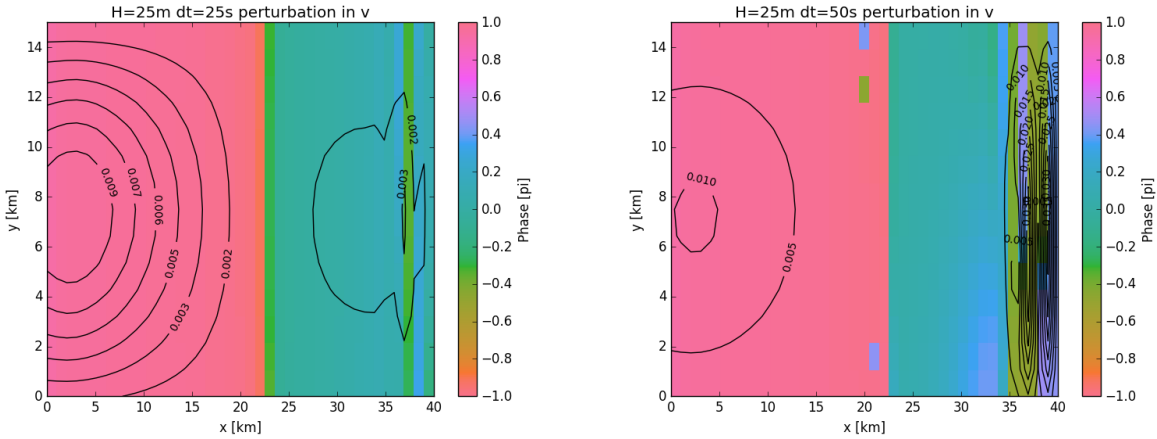


Figure 12: Influence timestep size on the phase and amplitude of the velocity component v . Results are plotted for a timestep size of respectively 25 and 50 s.

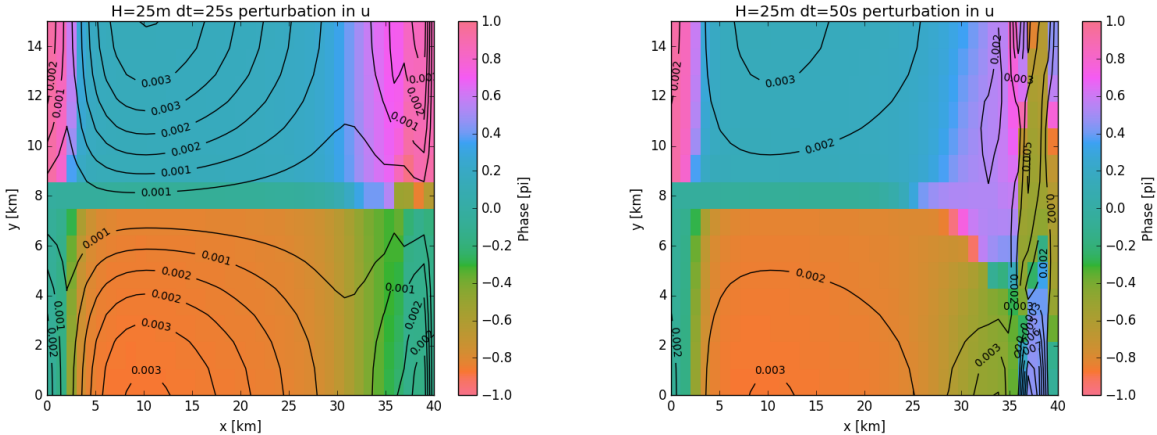


Figure 13: Influence timestep size on the phase and amplitude of the velocity component u . Results are plotted for a timestep size of respectively 25 and 50 s.

As is already clear from the (discretized) shallow water equations, model accuracy depends on a combination of timestep size, gridsize and water depth. In this case, water depth variations induce these irregular oscillations close to the open boundary in figure 12 and 13. With a flat bottom (close to the open boundary) these oscillations do not occur at all. Concluding, errors close to the open boundary can only be avoided by selecting small timesteps and hence an unacceptable computational time. This motivates to select five kilometres of the model domain near the open boundary as adaptation area. Moreover, this spin-up domain will have a flat bottom to further ease hydrodynamic computations. This can be observed from the (discretized) shallow water equations, where every spatial derivative with respect to $H(x, y)$ nullifies. Lastly, this area is excluded from morphologic computations, e.g. no bedprofile changes, no sediment in the water column. It should be noted that fixing the bathymetry in the spin-up domain may, for longer simulations, result in unusual bathymetry gradients. These inferior gradients may arise in the region where the transition between the spin-up domain (with fixed bathymetry) and the inner part of the estuary takes place.

4.7 Verification hydrodynamical model

The hydrodynamical model was developed from scratch, thus this requires continuous verification of the results. Ideally one would use analytical solutions to test the hydrodynamical model against simplified cases. For this purpose, some assumptions have to be made regarding hydrodynamics in order to test model performance against analytical solutions. In this section the model is verified by means of the ability of reproducing Kelvin waves, resonance effects, residual currents and velocity field patterns.

4.7.1 Kelvin waves and harmonic analysis

A well known benchmark problem is the Taylor problem: Kelvin wave reflection in a rectangular rotating basin with constant depth. In order to simplify the dynamics described by the shallow water equations given by equations 2, 3 and 4, the following list of assumptions are made:

- Dynamics are approximately 2D, hence depth averaging the velocity field is justified.
- Flat bedprofile
- Small velocities; nonlinear products are negligible.
- f-plane approximation.
- Linear friction

With these assumptions, the full set of governing equations becomes:

$$\frac{\partial u}{\partial t} - fv = -g \frac{\partial \zeta}{\partial x} - ru \quad (55)$$

$$\frac{\partial v}{\partial t} + fu = -g \frac{\partial \zeta}{\partial y} - rv \quad (56)$$

$$\frac{\partial \zeta}{\partial t} = -H \left(\frac{\partial u}{\partial x} + \frac{\partial v}{\partial y} \right) \quad (57)$$

Analytical solutions for a semi enclosed basin with the dynamics governed by setting $r = 0$ in equations 55, 56 and 57 were derived by Taylor (1920).³² Although Taylor's solution captured the important feature of an Amphidromic point, there was still room for improvement. Throughout time, it was attempted to generalize or extend the solutions by Taylor by adding for example friction, as was already present in the aforementioned equations in a linear form. In the next section the results of the hydrodynamical model reproducing Kelvin waves and Amphidromic points are presented.

In Rizal (2002),²⁵ the location of amphidromic points was investigated by using the analytical model of Rieneker and Teuber (1980).²⁴ An outline of the basin geometry assumed by the analytical solution is presented in figure 15. The dimensions of the basin (domain outline figure 15) are: width of approximately 500 km and a length of 1250 km. A flat bottom was used and the water depth 74 m.

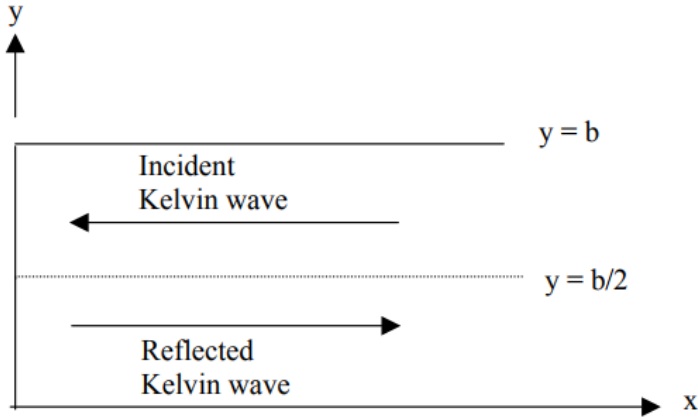


Figure 14: Semi-enclosed basin for which analytical solutions are available governing (damped) Kelvin waves. View is from top. As was used in Rizal (2002).

This exact set of dimensions are used in the hydrodynamical model used in this research. Rizal also varied the strength of the Coriolis effect by varying latitude. In the hydrodynamical model a typical value $f = 10^{-4}$ is used. With this the basin dimensions match the situation in Rizal (2002) completely. However, the hydrodynamical model still solves dynamics including advective terms. One can demonstrate by scaling that advective terms are negligible in this case:

$$x = \frac{x_*}{L} \quad y = \frac{y_*}{L} \quad z = \frac{z_*}{L} \quad u = \frac{u_*}{U} \quad v = \frac{v_*}{U} \quad t = t_*\sigma$$

Scaling yields the parameter $\epsilon = \frac{U}{\sigma L}$, also called the Strouhal number, which determines the order of the advective terms. Using typical values: $U = 1 \text{ m/s}$, $L = 100 \text{ km}$, and $\sigma = 10^{-4} \text{ s}^{-1}$, we have $\epsilon = 10^{-1}$. Hence advective terms will not influence the dynamics that much. The Kelvin wave amplitude and phase is plotted in figure 15.

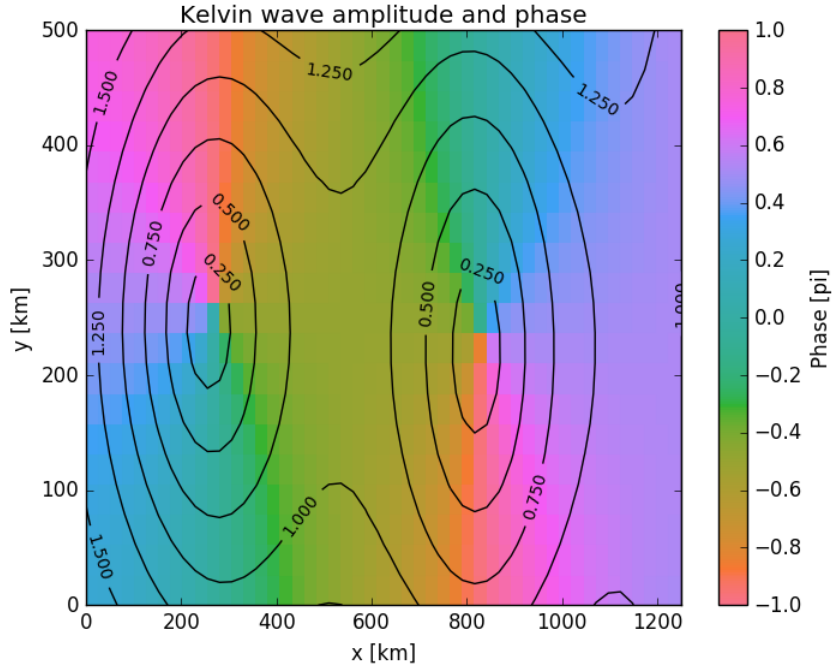


Figure 15: Phase and amplitude of $M2$ constituent in a basin with a flat bottom at a depth of 74m, dimensions are 1250 km by 500 km with a grid size of 25 km. This is the result by the numerical model of this project.

This is the only time in the results of this project that linear friction was used ($r = 5 \cdot 10^{-5}$), the same value that was used by Rizal (2002). The result by Rizal (2002) is visualized in figure 16 where on the axis the number of gridcells is indicated. To convert to dimensions in kilometers one has to multiply the x-coordinate with 25 ($\Delta x = 25$ km) and the y-coordinate with 20 ($\Delta y = 20$ km). By comparing the model results with the analytical solution, it can be concluded that the numerical model performed very well, e.g. similar Amphidromic point locations and similar phase and amplitude contour lines.

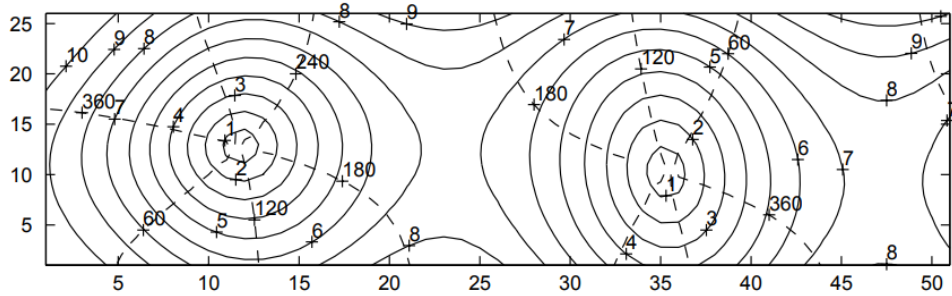


Figure 16: Phase and amplitude of $M2$ constituent in a basin with a flat bottom at a depth of 74m, dimensions are 1250 km by 500 km with a grid size of 25 km. Result by Rizal (2002).

4.7.2 Velocity field analysis

For simplified estuary geometries and dynamics, analytical solutions for the temporal and spatial structure of the velocity components are available. In Schuttelaars and de Swart (1998), the coupled system of momentum

and vorticity equations, concentration equation and bed evolution equation was considered for a non-rotating basin. Basically this is a set of 5 equations with 5 unknowns: u, v, ζ, C and h . Applying a tidal forcing at $x = L$ with the main tidal constituent M2, $\zeta(x, y, t) = \cos(t)$ allows as a dimensionless equilibrium solution: $u = -\sin(\sigma t)$ and $h_{eq}(x) = x$. Additionally it was assumed that there is no variation in the y -direction. For a (dimensional) bedprofile that is formulated like $h(x) = H(1 - \frac{x}{L})$ (sloping in the opposite direction), the solution for u , with $v = 0$ everywhere reads $u = \frac{\sigma L}{H} \sin(\sigma t)$. This can be considered to be a basic state, no perturbations are applied to the bedprofile yet. As a starting point, the ability of the hydrodynamic model to reproduce the velocity components is tested for this basic state. A harmonic analysis was used to determine amplitude and phase variations in u . In figure 17a it can be observed that clearly the velocity amplitude depends on x showing a decrease towards the closed end of the domain. Technically speaking, the bathymetry used for the computation of the numerical results was slightly different, i.e. $h = H(1 - x/L) + 3.0$ instead of $h = H(1 - x/L)$. The bedprofile had to be modified, because otherwise at $x = 0$, the waterdepth would have been zero, which is not acceptable for the numerical model. This minimum waterdepth of 3 m cannot be decreased even more, otherwise a blow up of the model occurs during the spin-up. This minimum water depth becomes relatively more important towards the closed end, causing a decrease of velocity amplitude in that area. On the other hand, the maximum velocity amplitude, which is about 0.3, corresponds greatly to the amplitude predicted by the equilibrium solution, figure 17, 18 and 19. Furthermore, the velocity phase is almost spatially independent (figure 17a), greatly corresponding to the analytical solution.

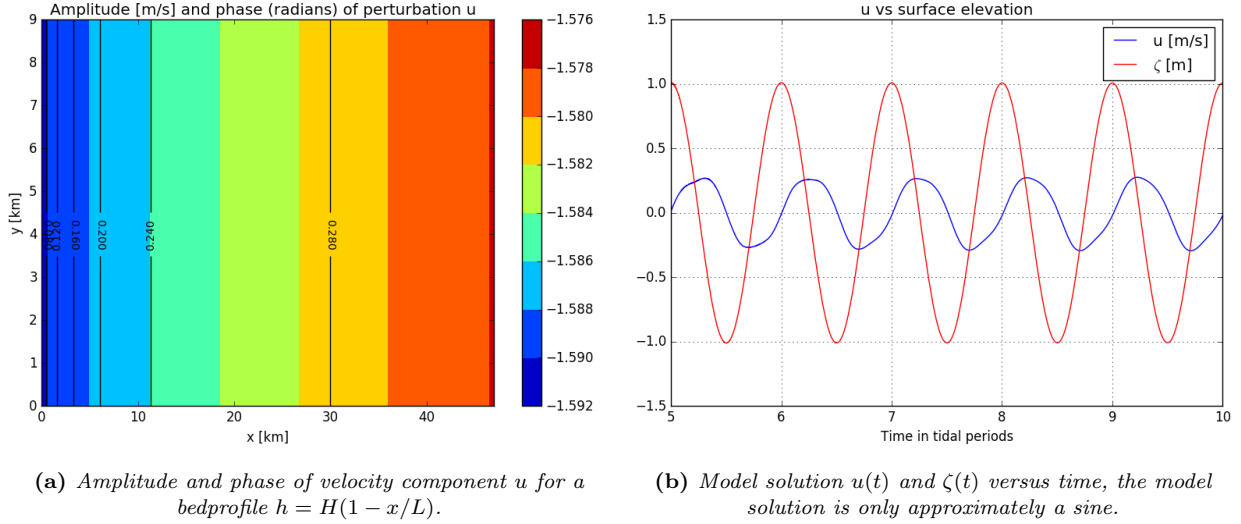


Figure 17: Respectively a harmonic analysis of u as a function position and time series of ζ and u from a location exactly in the middle of the basin.

Parameters used for this model run were: $H = 25$ m, $L = 50$ km and $\sigma = \frac{2\pi}{T}$ with $T = 43200$ s, approximately the tidal period. This yields a velocity amplitude of $2\pi * 50000/(25T) = 0.29$ m/s thus the numerical solution corresponds greatly to this amplitude. However, due to other interfering frequencies, the velocity curve is not a perfect sine, as can be observed in figure 19. Frequency peaks other than the tidal forcing frequency have periods of $1/2$ and $1/3$ of the tidal period, see figure 18. For the hydrodynamical model the nonlinear form of the shallow water equations is used, instead of a linearized form which is required for analytical solutions. Due to nonlinear effects, small M4 and M6 components arise and contribute to the time series. A period of about 6 hours (half the tidal period) corresponds to M4 and $1/3$ correspond to M6.

Until now, only a basic state with a flat but sloping topography was examined. By linearizing the system of equations (vorticity-, momentum-, concentration- and bed evolution equation), the response of the system, e.g. changes in velocity patterns, to 2D perturbations on the bedprofile can be analyzed. In the analysis by Schuttelaars and de Swart (1998) all variables are split in a zeroth order part (corresponding to the previous

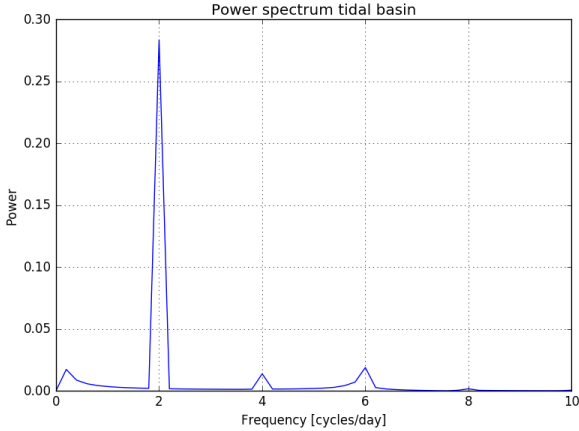


Figure 18: Power spectrum of the time series $\zeta(t)$ produced by the model for a linear sloping but flat bottom. One large peak is present, representing the M2 constituent.

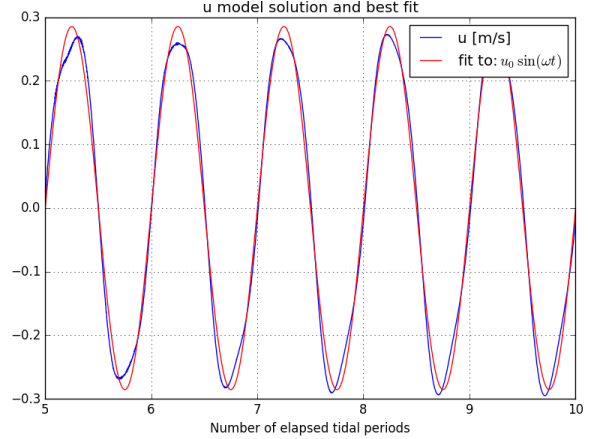


Figure 19: Numerical solution versus analytical solution for the amplitude and phase of u in case of a flat but sloping bedprofile.

equilibrium solution) and a 2D perturbation:

$$\Psi(x, y, t) = \Psi_{eq}(t) + \Psi'(x, y, t). \quad (58)$$

As already explained in the literature review, Ψ denotes a vector containing all variables $\Psi = (u, v, \zeta, C, h)$. The governing equations and the accompanying boundary conditions allow for velocity perturbation structures as in equations 60 and 61 in response to the perturbation in the bedprofile, equation 59.

$$h' = \sum_{n=0}^{\infty} h_n(x) \cos(l_n y) \quad (59)$$

$$u' = \sum_{n=0}^{\infty} [u_n^c(x) \cos(t) + u_n^s(x) \sin(t)] \cos(l_n y) \quad (60)$$

$$v' = \sum_{n=0}^{\infty} [v_n^c(x) \cos(t) + v_n^s(x) \sin(t)] \sin(l_n y) \quad (61)$$

Solving the longitudinal structure for all variables (in the x-direction) requires numerically solving an eigenvalue problem: $A\Psi = \omega B\Psi$. However, for vorticity conserving velocity fields (no dissipation of vorticity due to friction), analytical solutions can be derived for the longitudinal structure of the velocity components. Depending on the choice of the form and the number of bottom modes, one generates a perturbation on the velocity field u' and v' . As an example, we may select only one mode: $h' = A \sin(\pi x) \cos(l_1 y)$, figure 20.

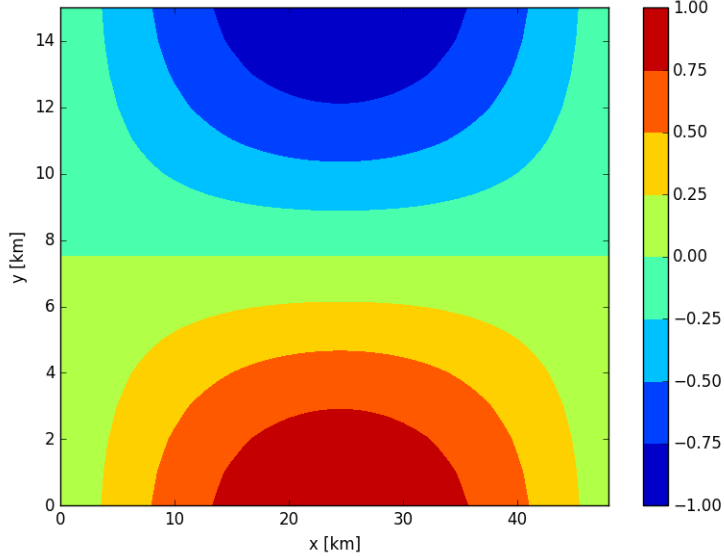


Figure 20: Plot of the structure of the perturbation h' in $h = h_{eq} + h'$ with $h' = A \sin(\pi x) \cos(l_1 y)$. Negative perturbation values correspond to more shallow areas.

Substituting the equations for u' and v' in the continuity and vorticity equations yields differential equations for u^s, v^s, u^c and v^c . As an example equations for the v component are given below with x-subscripts denoting derivatives with respect to x :

$$v_{nxx}^s - \frac{v_{nx}^s}{1-x} - l_n^2 v_n^s = l_n \frac{h_{nx}}{1-x} \quad (62)$$

$$(1-x)v_{nxx}^c - v_{nx}^c - (1-x)l_n^2 v_n^c = 0. \quad (63)$$

The governing equation for u_n^c, v_n^c can be characterized as a homogenous differential equation. Since the boundary conditions are homogenous too, these components (u_n^c and v_n^c) are zero over the whole domain and do not contribute to the perturbation solution u' and v' . Even though for irrotational flow fields these components do not contribute, they will in case when vorticity is produced (either by friction or Coriolis force). As demonstrated by Schuttelaars and de Swart (1998), non-trivial analytical solutions for respectively u_n^s, v_n^s exist. Equation 62 is an inhomogeneous Bessel equation but the analytical solution is rather complicated. u_n^s is related to v_n^s by: $u_n^s = -l_n \frac{\partial v_n^s}{\partial x}$. These equations can also be solved numerically, the numerical solution of equation 62 with boundary conditions $v' = 0$ at $x=0$ and $\frac{h'}{1-x} = \text{finite}$ at $x=1$ is presented in figure 21.

Here $l_n = \frac{n\pi L}{B}$, so in case of $n=1$, we have $l_1 = \frac{\pi L}{B}$ and from now on, subscript or index n is omitted, since it is set to 1. If equation 61 is considered at $y = \frac{B}{2L}$ in non-dimensional coordinates, then equation 61 is simplified to: $v' = v^c(x)$ at $t = (0, 1, 2, \dots)\pi$ and $v' = v^s(x)$ at $t = (0, 1, 2, \dots)\pi + 0.5\pi$.

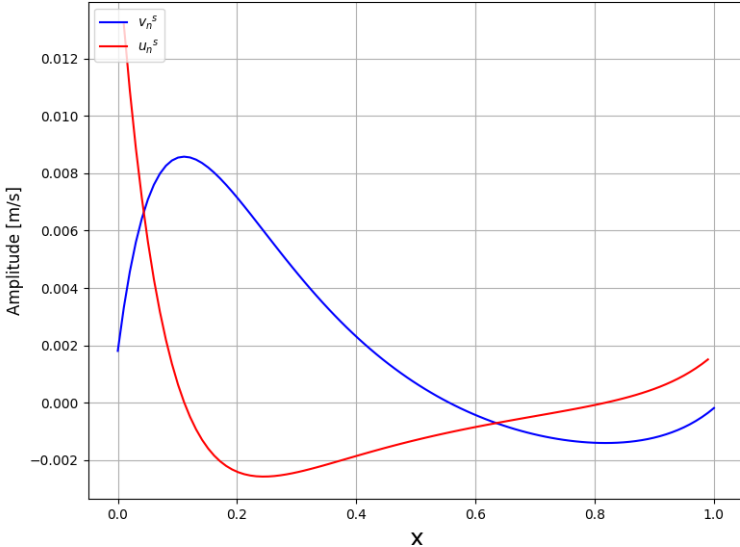


Figure 21: Plot of the structure in x -direction of the solution for respectively u_s and v_s . This is for the case that $t = 0.5\pi$ and respectively $y = 0$ and $y = \frac{B}{2L}$ to illustrate the structure in x -direction best. Compared to Schuttelaars and de Swart (1998), in our case $x=1$ represents the open boundary and not $x=0$, the analytical solution is mirrored in $x=0.5$.

A harmonic analysis was conducted to obtain the perturbation on the velocity field. Using the slightly modified equilibrium profile from Schuttelaars and de Swart (1998), which is, as already mentioned $h = H(1 - x/L) + 3.0$, the structure of the perturbations was investigated for different timestep-sizes, namely for 25 and 50 seconds. If the perturbation on the linearly sloping bottom profile was not present, then $v=0$. Adding the perturbation on the bottom profile immediately yields the perturbation in v . However, to obtain the perturbation in u' in $u = u_{eq} + u'$, first time series of $u_{eq}(t)$ were obtained. Subsequently the model was run and $u(t)$ was obtained. Afterwards these time series were subtracted from each other to derive the perturbation structure. Qualitatively, the patterns in the perturbation structure by the numerical model, figure 22 match with the analytical solution, figure 21. At the sides $y = 0$ and $y = B$, the perturbation in v becomes zero, whereas u becomes zero at $y = B/2$. This is in line with equations 60 and 61. Furthermore, if the analytical solution changes sign, so does the phase of the perturbations according to the numerical model. In addition, the locations with strongest perturbation velocities match with the analytical solution. However, quantitatively, the numerical results of velocity component u close to $x = 0$ are smaller compared to the analytical solution. As already mentioned, the bathymetry used for the computation of the numerical results uses a minimum water depth of 3 m to prevent a blow up, i.e. $h = H(1 - x/L) + 3.0$ instead of $h = H(1 - x/L)$. This causes a decrease in velocities towards the closed end of the domain. Hence, this can explain weaker perturbation magnitudes.

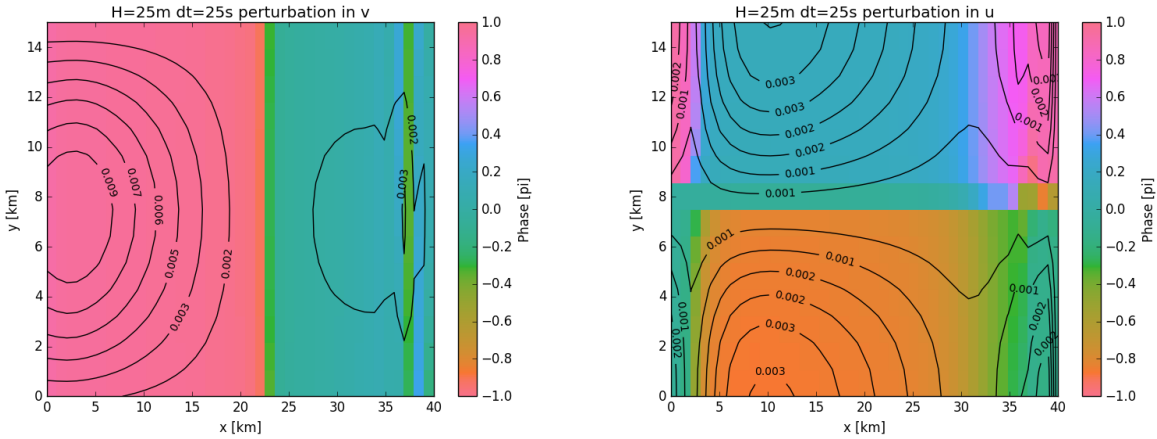


Figure 22: Perturbation structure for respectively v and u . Close to the open boundary, structures in the velocity field become more irregular due to numerical inaccuracies.

4.7.3 Resonance effects

If the basin lengthscale is similar to one quarter of the tidal wavelength, resonance effects occur,² i.e. amplification of the tidal amplitude. For the sake of verification, a frictionless narrow elongated basin was tested on resonance effects. A water depth of 20 m and a domain length of 150 km was used such that the domain length corresponds to one quarter of the tidal wavelength. Strong resonance effects occurred with the model producing wave heights of up to 10 m before the model blows up, as can be observed in figure 23.

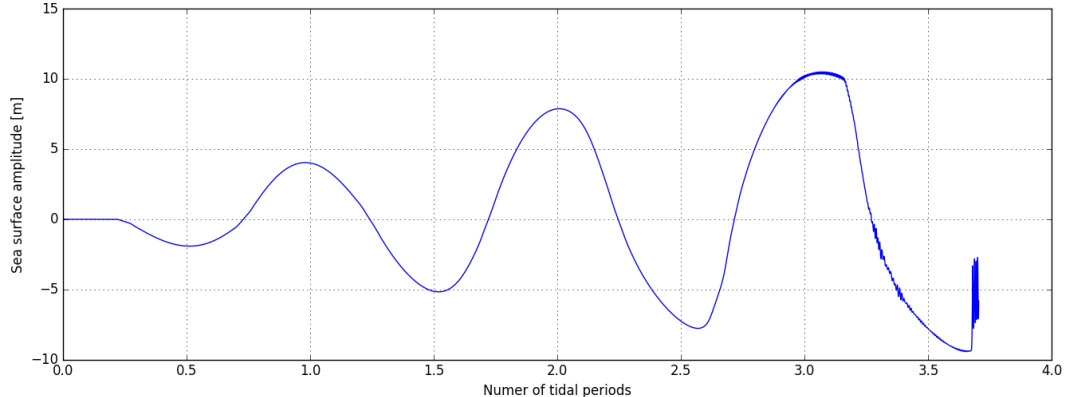


Figure 23: Resonance in a narrow elongated channel with $H = 20\text{m}$ and $L = 150\text{km}$, with L being approximately one quarter of the tidal wave length, one would expect resonance. Friction was almost turned off (factor 100 decrease).

Concluding, the numerical model is able to capture this mechanism.

4.7.4 Residual current verification

In the previous section it was established that the hydrodynamical model was capable of reproducing oscillatory perturbation structures correctly. Since nonlinear effects (friction, inertia) also produce residual velocity fields, the ability of the model to reproduce this should be examined too. Residual fields produced

by the model are presented and analyzed qualitatively (in terms of patterns) as well quantitatively (magnitude of the residual field). Analytical solutions for residual velocity fields exist only in simplified cases, the shallow water equations have to be linearized in order to obtain analytical solutions. In figure 24 the residual velocity field produced by the numerical model is visualized for a water depth of 10 meters. The analytical solution for the same bedprofile perturbation is given in figure 25 where both the left and the right boundary are open (semi-infinite domain). The analytical solution for the residual velocity field follows from time-averaging the vorticity equation, as explained by Schuttelaars et al. (2002). Since the analytical solution is valid for a semi-infinite channel, the numerical residual velocity field is computed in the middle of a channel with a length of 100 km to resemble the analytical solution better. In this way, (closed and open) boundary effects are minimized.

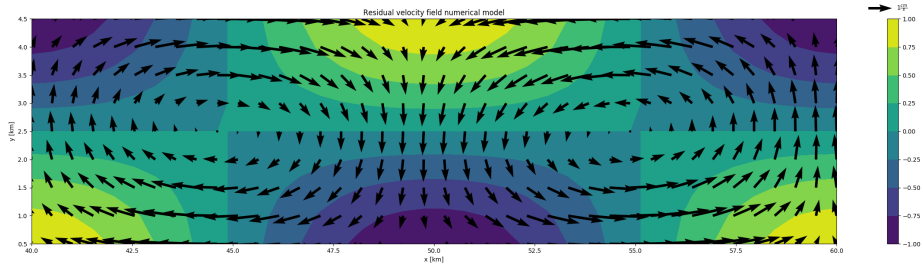


Figure 24: Residual field produced by the hydrodynamical model for a perturbation of 1 meter. The residual velocity field shown, is in the middle of channel with a length of 100 km instead of 20 km, in order to resemble the analytical solution better of figure 25, which is valid for a semi-infinite channel.

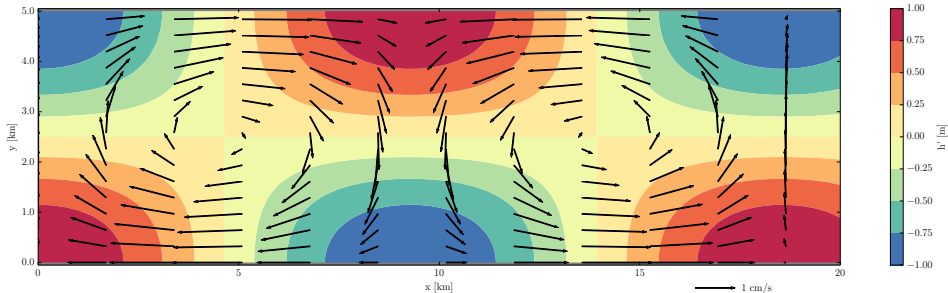


Figure 25: Residual field according to analytical solutions of Schramkowski et al. (2002) to the simplified and linearized shallow water equations by Tjebbe Hepkema. Here both the left and the right boundaries are open.

The patterns are more or less the same: the numerical model is capable of producing reasonable residual velocity fields.

In the computation of the residual velocity field by the numerical model, the Stokes flow effect has been removed to visualize the effect of bathymetry variations on the residual flow. Next to a varying bathymetry, Stokes flow also causes gradients in the horizontal velocity field. Stokes flow can be separated from the residual velocity field to highlight the residual part due to bathymetry variations. Before embarking on how to do so, the Stokes flow mechanism is briefly discussed. The tidal wave can be characterized as a purely progressive wave in an infinitely long channel, whereas in estuaries, the tidal wave is in fact a superposition of an incident wave and a reflected wave.^{18,38} Bottom friction causes a loss of tidal wave energy, which implies that the reflected wave is relatively weak with respect to the incident wave. Moreover, if the reflected wave is weak, the tidal wave has a more progressive nature. For a purely progressive wave there is no phase

difference between surface elevation and flow velocity. Furthermore, maximum ebb and flood velocities are almost equal, resulting in a net transport of water. During flood, the total water depth is larger than ebb, while the flow velocities remain the same, hence during flood more water is transported landward. This causes a nonzero mean surface elevation which increases landward yielding a negative pressure gradient in the surface elevation which in turn evokes a seaward flow, called Stokes flow.¹⁴ In order to capture residual variations in the horizontal velocity field caused by bathymetry variations only, we have to determine average velocity by making use of equation 64, with \mathbf{u} the velocity vector.

$$\bar{\mathbf{u}}(x, y) = \frac{1}{T(H_0 + B(x, y))} \int_0^T [H_0 + B(x, y) + \zeta(x, y, t)] \mathbf{u}(x, y, t) dt \quad (64)$$

In all the residual velocity field plots presented in this research, Stokes flow is excluded by using equation 64.

5 Sediment transport and bed evolution model

In this section, an outline of the second part of the numerical model is presented. This second part consists of a kinematic model and the other part accounts for sediment transport processes. Firstly, erosion and deposition parametrizations are discussed, secondly the numerical implementation of particle tracking and sediment transport processes is described. Lastly, the process of model verification is presented. Before continuing, a few assumptions that are (implicitly) made in deriving the results presented in later sections are listed below:

- Non-erodible estuary banks
- No bedslope effects
- No diffusion of sediment
- Unlimited sediment availability, i.e. erodible bottom layer
- Bottom sediment is characterized by fine grained sediment (diameter $\approx 60 \mu\text{m}$)
- Flocculation and fragmentation is not accounted for
- No net residual bed load transport, only suspended sediment (fine sediment, diameter $\approx 60 \mu\text{m}$) is considered.
- Bottom layer consists of non-cohesive and uniform sediment.
- Suspended sediment does not influence the fluid density

5.1 Numerical implementation particle tracking

In order to solve the advection of particles, the kinematic equations (equation 1) have to be integrated over time. For the time integration both Euler forward and Runge Kutta 4 (abbreviated RK4) were tested. Basically, Euler Forward is a simplified form of RK4. The difference is determined by the truncation order of the Taylor series of function y around a certain point x_0 . Compared to Euler Forward, RK4 truncates the Taylor series at a later stage. RK4 has better stability properties,³⁷ more than compensating the fact that it is computationally more expensive than Euler forward.

However, during the first numerical experiments with integrating the kinematic equations, a problem concerning mass conservation quickly surfaced. Mass conservation is defined in terms of transport (water depth multiplied by depth averaged velocity) or discharge, not in terms of velocities. Using flow velocities only does not guarantee divergence-free particle movement (it does in 3D, not in 2D). This problem can be deduced by observing the continuity equation for shallow water:

$$\frac{\partial(uH)}{\partial x} + \frac{\partial(vH)}{\partial y} + \frac{\partial H}{\partial t} = 0. \quad (65)$$

Clearly the influence of both bedprofile and surface height variations become increasingly more important for decreasing water depths. Hence, the problem of local convergence/divergence of particle trajectories becomes more significant too.

To illustrate the need for a divergence free method, an Eulerian viewpoint is employed to monitor local convergence or divergence of mass. Basically, the concentration of particles in gridcell i with (gridcell) coordinates (x_i, y_i) is determined by accumulating each particle labelled k present in this particular grid cell i . Subsequently, the total amount of particles is divided by the grid cell volume which in turn is determined by grid size $\Delta x, \Delta y$ and water height.

$$C_{xi,yi} = \sum_k^N M_k / V_{xi,yi} \quad (66)$$

A spatially periodic perturbation was applied to the bedprofile to provide a realistic test case. Starting from a fully uniform particle distribution (50 particles per gridcell volume of $V_0 = \Delta x \Delta y H_0$, it can be observed that the classical method (eq. 1) quickly yields inferior results, figure 26. Some areas experience a strong convergence of particles, corresponding to an accumulation of water, whereas in other regions, no particles are left at all, corresponding to a dry area.

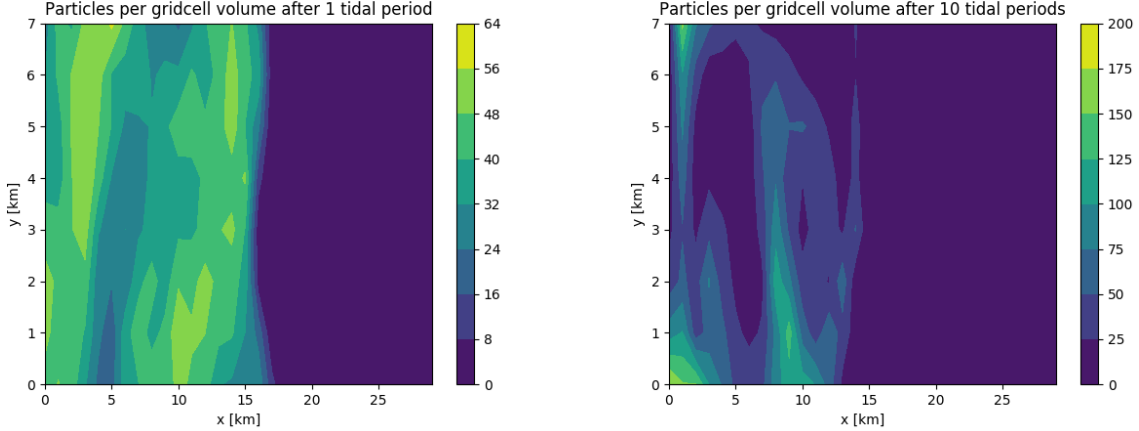


Figure 26: Particle concentration after respectively 1 and 10 simulated tidal periods. Especially after 10 tidal periods, some regions experience strong convergence of particles, i.e. accumulation of water.

To overcome this mass conservation problem, a few strategies are available. For this project, the solution proposed by Postma et al. (2012) is followed. This solution assumes particles to have their own volume (and location), which is exactly how in this project a particle is defined, i.e. a subvolume. In this way, persisting convergence and divergence is not acceptable. For convenience, the definition of a particle is repeated below:

Particle: a sub-volume of water which moves throughout the domain with its own location.

In the method of Postma et al. (2012), particle velocities are determined by using volumes and discharges rather than velocities. Instead of velocities, rates of 'fraction of grid cell volume per second' are defined at the gridcell boundaries. In figure 27 the sides of an example gridcell coincide with locations of the velocities on the staggered grids provided by the hydrodynamical model. Therefore the output location of the u-component coincides with the left and the right cell edge while the v-component coincides with the lower and upper cell edge. At these locations, the depth averaged velocities u, v provided by the hydrodynamic model are converted to discharges, respectively Q_x and Q_y . This is achieved by multiplying u, v with the total water depth and gridcell width (respectively dy and dx) over which u, v enter the gridcell.

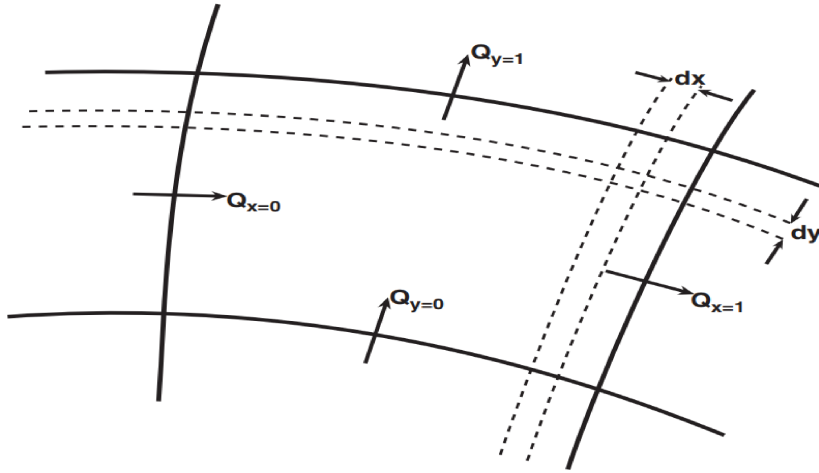


Figure 27: Illustration of the curvilinear grid by Postma et al. (2012). All the Q 's are discharges with units m^3/s . The flow rates are computed by dividing each Q by the average grid cell volume. dx and dy form an area which should be interpreted as a sub-volume within the gridcell.

Subsequently, to obtain flow rates (unit: 1/s), the discharge is divided by the gridcell volume. A simple linear interpolation yields the particle velocities within each gridcell:

$$u = u_0 + x(u_1 - u_0), \quad v = v_0 + y(v_1 - v_0) \quad x, y \in [0, 1] \quad (67)$$

This flow rate indicates how fast the particle travels through the gridcell, expressed in fraction of the gridcell volume per second. Within such a gridcell, both the x and y coordinate are in the range between 0 and 1. This is because particle coordinates inside a grid cell are viewed as volumetric (dimensionless) coordinates. In figure 28 the particle concentration by the non mass conserving method is compared with the Postma method. The results of the Postma method more or less preserves mass because the particle concentration remains about spatially uniform. However, after simulating hundred or a few hundreds of tidal periods using the Postma method, the results eventually displayed convergence or divergence, possibly due to numerical inaccuracies. Nevertheless, this is not harmful for sedimentation processes since this happens on a timescale much larger than a particle spends time in the water column. Note that at this point, no additional particles enter the channel during flood (hence a particle concentration of zero towards the open boundary) and no particles left the domain during this simulation.

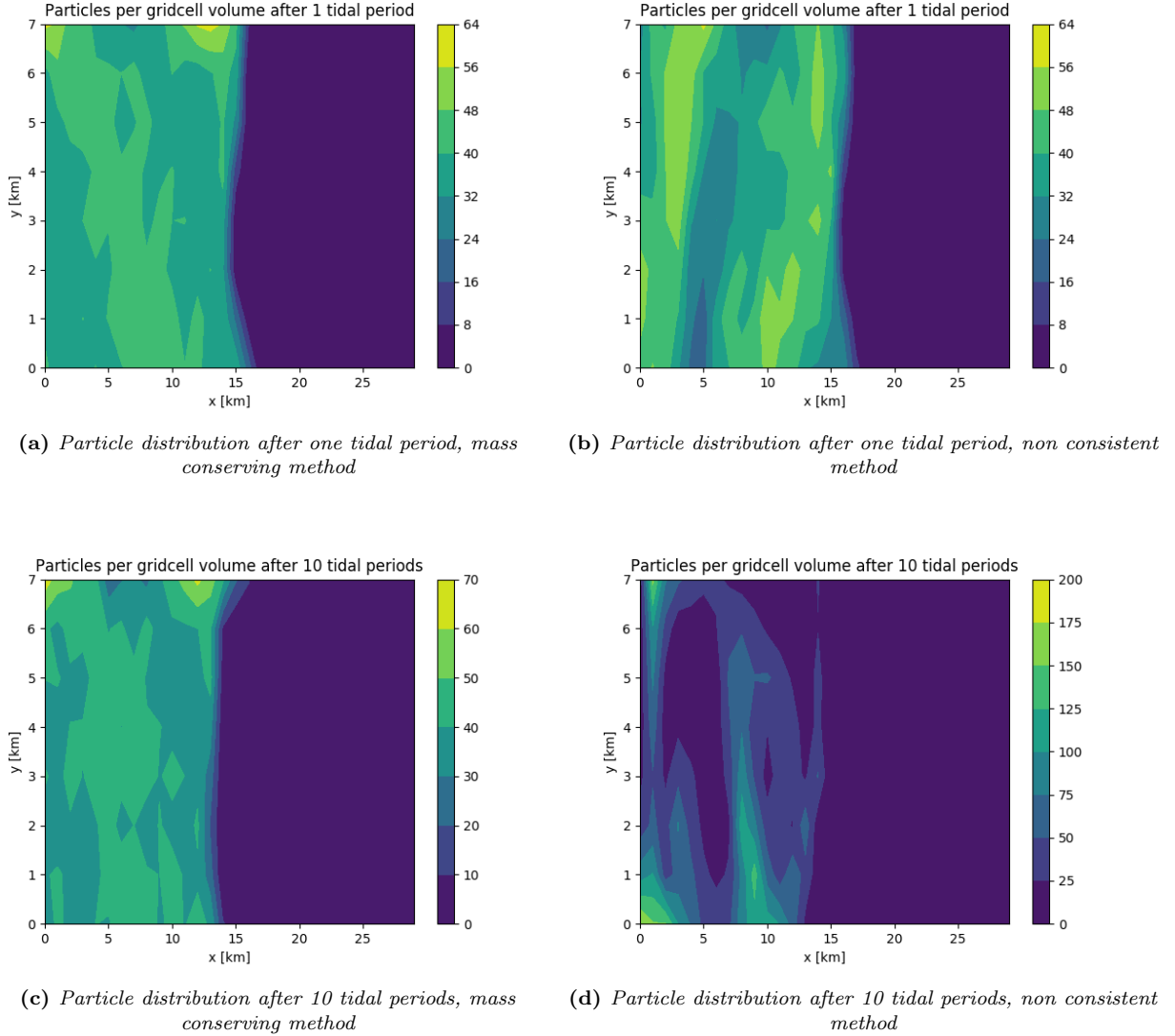


Figure 28: Comparison of the results produced using the method by Postma et al. (2012) on the left and the non-conserving method that uses velocities on the right, after respectively one and 10 tidal periods.

To quantify the improvements of using the Postma method, the mean and standard deviation of particle concentration was monitored for two different basins. The first half of the domain was initialized with a particle concentration of 50 particles per V_0 . For each basin the mean and standard deviation (equation 68, N is the number of particle containing gridcells) at specific moments in time were determined for different water depths. Whereas the non-consistent method (where velocities are used and not volumes) displays large variations in particle distributions, the Postma method does not, see table 1. Variations in the mean concentration of particles are minor and the standard deviation is relatively small compared to the non-consistent method. This means that a particle density of 50 particles (or higher) per V_0 prevents the existence of voids or empty areas.

$$\mu = \frac{1}{N} \sum_i^N C_i, \quad \sigma = \sqrt{\frac{1}{N} \sum_i^N (C_i - \mu)^2} \quad (68)$$

| Number of tidal periods | H = 2.5 m | | H = 5 m | | H = 10 m | |
|-------------------------|-----------|-------|----------|-------|----------|-------|
| | σ | μ | σ | μ | σ | μ |
| 1 | 3.7 | 49.8 | 3.3 | 49.8 | 2.1 | 49.8 |
| 5 | 6.1 | 49.8 | 3.4 | 49.8 | 3.4 | 49.8 |
| 10 | 8.1 | 49.7 | 3.9 | 49.8 | 3.4 | 49.8 |
| 20 | 10.9 | 49.9 | 4.5 | 49.8 | 3.6 | 49.8 |

| Number of tidal periods | H = 2.5 m | | H = 5 m | | H = 10 m | |
|-------------------------|-----------|-------|----------|-------|----------|-------|
| | σ | μ | σ | μ | σ | μ |
| 1 | 4.8 | 49.6 | 4.0 | 49.9 | 2.5 | 49.8 |
| 5 | 16.7 | 48.7 | 13.7 | 50.7 | 5.5 | 49.9 |
| 10 | 29.8 | 48.3 | 25.4 | 51.7 | 9.5 | 50.0 |
| 20 | 48.8 | 49.1 | 41.2 | 51.2 | 17.8 | 50.4 |

Table 1: Mean and standard deviation of the particle concentration within particle containing grid-cells on a domain of 8×80 km. On the left the consistent method by Postma and the non-consistent method on the right.

5.2 Numerical implementation erosion and deposition

For every particle (sub-volume), while moving through the domain, the Lagrangian form of the concentration equation is solved, repeated here for convenience:

$$\frac{d\hat{C}}{dt} = \rho_s \frac{S_*}{H} \quad (69)$$

where \hat{C} is the depth averaged sediment mass concentration with units kg/m³. The numerical model uses an equivalent form of this equation, instead of using \hat{C} as a variable, the mass M will be used as variable. Naturally, the sediment concentration of each subvolume is related to the total sediment it holds by: $\hat{C} = M/V$. Here V represents the total volume of water of a subvolume. At the start of the simulation, each particle is initialized with the same volume of water and this is equal to: $V = \Delta x \Delta y H_0/N$. N is the average amount of particles present in a gridcell. Substituting M for \hat{C} in the concentration equation yields:

$$\frac{dM}{dt} = \frac{V}{H} \rho_s S_* \quad (70)$$

with d/dt denoting the total (material) derivative. Using $V = \Delta x \Delta y H_0/N$ (in fact assuming: $H_0 \approx H$, see section 7), gives:

$$\frac{dM}{dt} = \frac{\Delta x \Delta y}{N} \rho_s S_* \quad (71)$$

Using equations 27, 30 and 31 for the erosion and deposition term S_* yields:

$$\frac{dM}{dt} = \frac{\Delta x \Delta y}{N} \rho_s \left(w_s (1-p) \frac{\gamma s}{1 + \gamma s} - \frac{w_s^2 C}{K_v} \right). \quad (72)$$

C absorbs ρ_s according to $H\hat{C} = C\rho_s$, yielding:

$$\frac{dM}{dt} = \frac{\Delta x \Delta y}{N} \left(\rho_s w_s (1-p) \frac{\gamma s}{1 + \gamma s} - \frac{w_s^2 \hat{C} H}{K_v} \right). \quad (73)$$

and subsequently using $M/V = \hat{C}$ and $V = \Delta x \Delta y H_0/N$, gives:

$$\frac{dM}{dt} = \frac{\Delta x \Delta y}{N} \rho_s w_s (1-p) \frac{\gamma s}{1 + \gamma s} - \frac{w_s^2 M}{K_v}. \quad (74)$$

In the numerical model a discretized form of the latter equation is used:

$$M_p^{i+1} = M_p^i + \Delta t \left(\frac{\Delta x \Delta y}{N} \rho_s w_s (1-p) \frac{\gamma s}{1 + \gamma s} - \frac{w_s^2 M_p^i}{K_v} \right). \quad (75)$$

Now both erosion and deposition are explained, but how is the eroded or deposited mass transferred to changes in the bathymetry? For this purpose, neglect erosion processes for simplicity. If only deposition is taken into account, then the amount of sediment inside a subvolume p during the next timestep is equal to:

$$M_p^{n+1} = M_p^n \left(1 - \Delta t \frac{w_s^2}{K_v}\right). \quad (76)$$

This yields the amount of sediment lost by deposition for particle p at timestep n : $M_p^n \Delta t \frac{w_s^2}{K_v}$. As already mentioned, this in fact happens on a sub-grid scale while only computations on the gridcell scale are possible. Therefore, we assume that the mass lost by deposition is evenly distributed over the complete gridcell in which the particle is located. The numerical model saves the amount of mass received by deposition and lost by erosion for each gridcell. Before running the model, a threshold value can be specified after which the model will update the bathymetry according to the net changes. The amount of eroded sediment lost by gridcell with indices i, j due to erosion is equal to $\Delta t \Delta x \Delta y w_s (1-p) \frac{\gamma s_{i,j}}{1+\gamma s_{i,j}}$. In accordance with this, the amount of sediment received by every particle present in gridcell i, j is:

$$M^{n+1} = M^n + \frac{\Delta t w_s (1-p)}{N_{i,j}} \frac{\gamma s_{i,j}}{1+\gamma s_{i,j}}. \quad (77)$$

For simplicity, one representative bottom stress value is used for the complete gridcell. In other words, no sub-grid variations in the bottom stress are considered. $N_{i,j}$ denotes the number of particles present in gridcell i, j and $N_{i,j}$ is selected in such a way that at least 100 particles are present in an area of one squared kilometre. Technically deposition and erosion takes place on sub-grid scale while the bathymetry is defined on a grid. In reality bathymetry is of course continuous. Basically, this implies that, while erosion and deposition are taking place in each sub-volume, this can only have an impact on the (much larger) scale of a gridcell. Each gridcell has its own bathymetry value and within such a gridcell there can be no bathymetry variations.

5.3 Verification kinematic model

This part of the numerical model also required an extensive verification. In order to test the kinematic model, particle trajectories by the numerical model are compared to the trajectories produced by the model by Beerens et al. (1994), equation 17. For this purpose, firstly two sample estuaries and the accompanying particle trajectories by the numerical model are presented. Some model domain properties and numerical settings and results in the form of (individual) particle trajectories and parameter values are given. The two examples are different in the sense that the second example has a relatively strong residual velocity field compared to the first one. Beerens et al. (1994) considered a semi-infinite channel with a velocity field being a superposition of a residual and an oscillating tidal part. Furthermore that model assumes a flat bottom and makes the rigid-lid assumption, for more details see section 2. Next, the model by Beerens is slightly modified and subsequently used to produce trajectories with parameters λ and ν matching the values found in the numerical test cases.

5.3.1 Particle trajectories numerical results

First example:

Domain properties and numerical aspects:

- $L = 80$ km, $W = 8$ km
- $H_0 = 10$ m.
- $L_E = 8$ km, eddy length.

- $H(x, y) = H_0 + \cos(\pi x/L_E) \cos(\pi y/L_E)$
- 1 particle per grid cell
- $\Delta x, \Delta y = 500$ m
- 50 tidal periods of simulation

Particle trajectories:

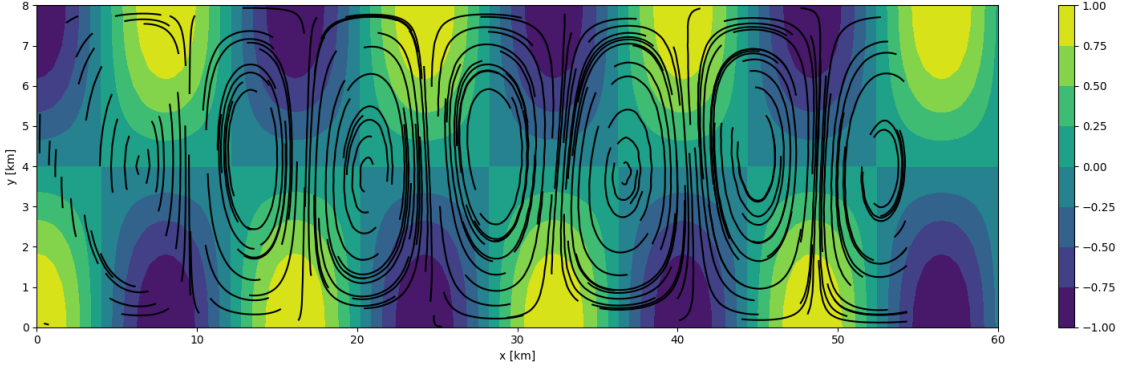


Figure 29: Particle trajectories indicated by black lines in a rectangular channel with a perturbation on a flat bottom: positive values indicate deeper areas and the unit is m. Very structured particle trajectory patterns can be observed throughout the domain.

Parameter values λ and ν :

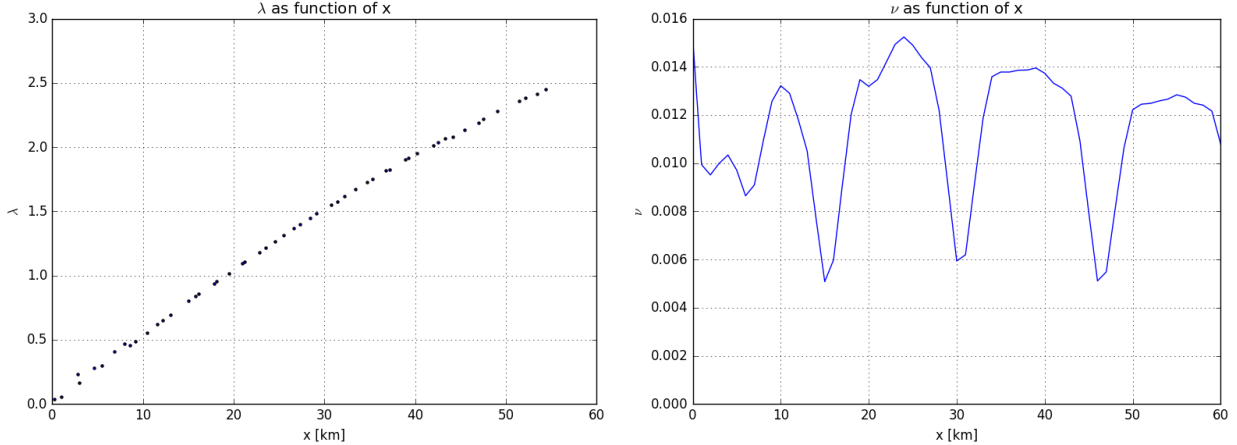


Figure 30: Parameter values as function of x , measured along $y = W/2$. ν is a measure of the strength of the residual velocity field, whereas λ is the fraction of tidal excursion length over perturbation wavelength. Since the velocity in the channel decreases towards the closed end at $x = 0$, so does the tidal excursion length and correspondingly, λ .

Individual particle trajectories:

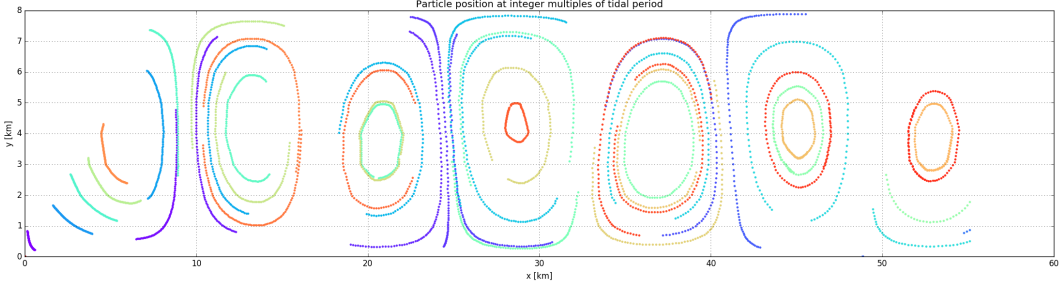


Figure 31: Particle position at integers multiples of simulated tidal periods. Very structured particle trajectory patterns are present in the domain. Each color indicates a different particle.

Second example:

Domain properties and numerical aspects:

- $L = 80 \text{ km}$, $W = 8 \text{ km}$
- $H_0 = 4 \text{ m}$.
- $L_E = 4 \text{ km}$, eddy length.
- $H(x, y) = H_0 + 2.5 \cos(\pi x/L_E) \cos(\pi y/L_E)$
- 1 particle per grid cell
- 10 spin-up columns with a flat bedprofile
- $\Delta x, \Delta y = 500 \text{ m}$
- 50 tidal periods of simulation

Particle trajectories:

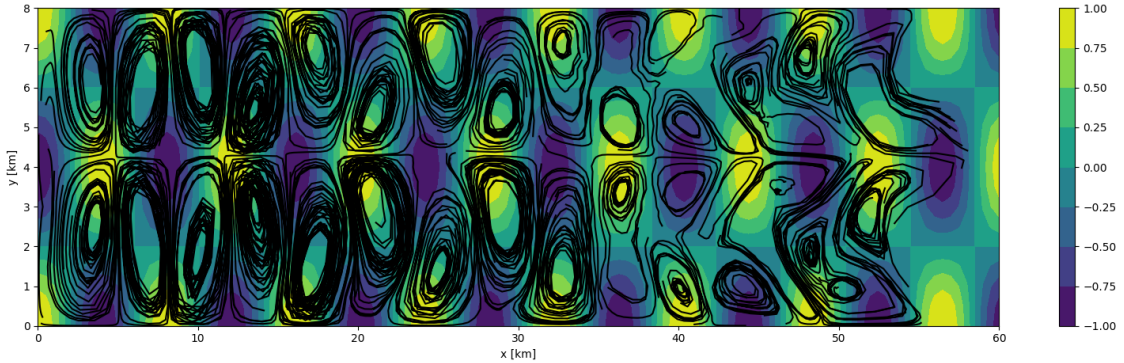


Figure 32: Particle trajectories in a rectangular channel with a perturbation applied to a flat bottom, purple areas indicate shallow regions. Bifurcation of circular trajectory structures occurring between $x = 30$ and $x = 40$.

Parameter values:

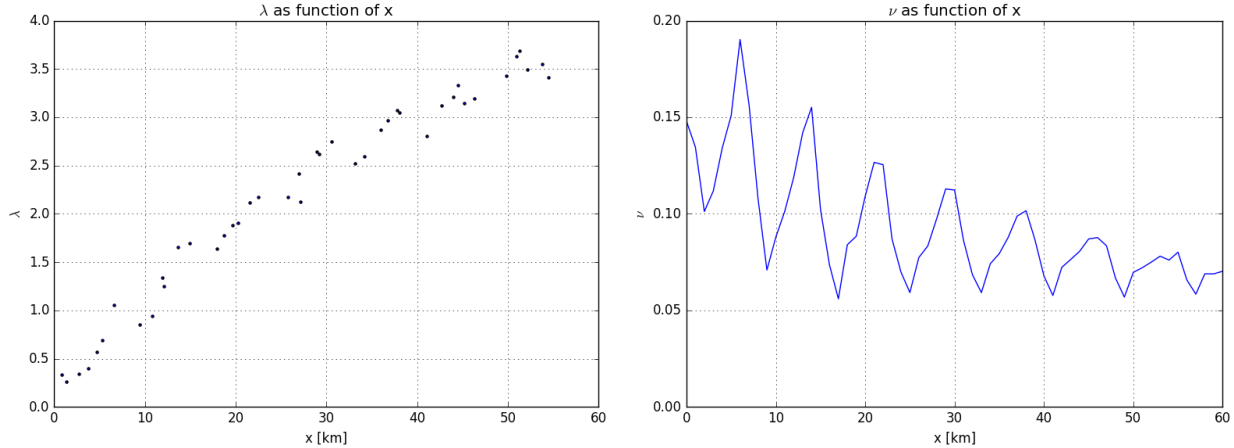


Figure 33: Parameter values as function of x , measured along $y = W/2$. The residual velocity field is relatively strong in this case, with ν reaching values of 0.2 towards the closed end of the channel.

Individual particle trajectories:

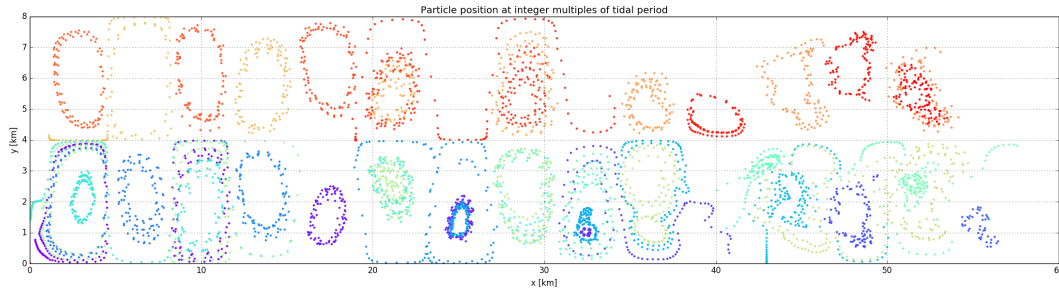


Figure 34: Particle position at integers multiples of simulated tidal periods, each color indicates a different particle. Towards the open boundary, some particles travel great distances throughout the domain, switching between different circulation cells via the edges. When closeby particles diverge rapidly, this is characterized as chaotic behaviour.

Below, some comments on the numerical results are made before these results are compared with the model by Beerens. For convenience, the definitions of the parameters λ and ν used in the model by Beerens et al. (1994), are repeated:

$$\lambda = \frac{L_T}{L_E} = \frac{\text{tidal excursion}}{\text{eddy diameter}} , \quad \nu = \frac{u}{U} = \frac{\text{velocity in residual eddies}}{\text{tidal velocity amplitude}} . \quad (78)$$

Whereas the kinematic model by Beerens (equation 17) assumes λ and ν to be spatially uniform, this is clearly not the case when applied to estuaries, figure 30 and 33. Hydrodynamic conditions change from the open boundary towards the closed end of the estuary, on the left ($x = 0$) and this is reflected by the spatial dependency of the parameters λ and ν . Especially λ has a strong dependency on the longitudinal coordinate x . For every particle, the tidal excursion length is determined and given the perturbation wavelength, λ can be computed. Close to the open boundary, flow velocity is strongest and this decreases almost linearly towards the closed end. Since λ is related to the tidal excursion length (equation 16), it makes sense that λ closely follows this trend. The perturbation wavelength can only amplify or weaken this trend. In the second example the perturbation wavelength is halved, indicating that λ doubles. This is the case, as can

be observed by comparing figure 30 and 33. In the second example, a relatively strong residual velocity field is present, a magnitude stronger than in the first example. This is due to strong bathymetry variations with an amplitude of 2.5 m (over a depth of 4 m): perturbation strength is increased and the water depth is decreased. Both factors contribute to a stronger residual velocity field. Depending on the perturbation strength and wavelength, ν is mostly in the range of $\nu \in [0, 0.20]$. In numerical experiments it was found that only for very strong bathymetry variations and larger wavelengths ν could reach up to 0.25 or at most 0.30 towards the closed end of the basin. Generally, larger values for ν ($\nu > 0.05$) lead to chaotic behaviour, according to the model by Beerens et al. (1994). Chaotic behaviour is characterized by particles travelling large distances throughout the domain and often particles follow irregular trajectories. However, if large values of ν are accompanied with small values for λ ($\lambda < 1$, this chaotic behaviour is suppressed. Often an anticorrelation between ν and λ was found, this is best illustrated in a (parametric) plot of ν against λ in figure 33. λ decreases towards the closed end, while on the other hand ν increases. Since the parameters λ and ν are spatially dependent in estuaries, the phase space is spatially dependent too, i.e. particle trajectories are different throughout the basin.

In the first example, with the lowest energetic conditions and a relatively weak residual velocity field, particle trajectories closely follow residual circulation cells. In figure 29 particle positions at integer multiples of a tidal period are plotted and all these locations are connected with a line to distinguish individual trajectories through time. Particles travel around in circles around (elliptic) fixed points in this first example; they traverse a periodic orbit. If a particle situated at location \mathbf{x}_0 returns to this initial location after a period T , then this point \mathbf{x}_0 (i.e. location) is part of a periodic orbit.²² If a particle is situated on a periodic orbit after each tidal period, it returns to this exact location. The strongest variations in trajectory patterns are found in the second example. While trajectories closely follow residual circulation cells near the closed end, this behaviour changes around $x = 30$ km. At $x = 30$ km the circular trajectory patterns bifurcate and the cell-like structures split in multiple smaller regions in which particles follow more irregular trajectories. Particles are no longer limited to a specific circulation cell but can now switch between circulation cells, figure 34. Since particles carry sediment, mixing of particles with other circulation cells leads to enhanced sediment dispersion in chaotic regions. Regions where particles display this chaotic behaviour are associated with hyperbolic points of the velocity field, as explained in section 2. In section 6, an example is given where chaotic regions are more widespread.

5.3.2 Particle trajectories (semi-) analytical results

Now, the numerical results are compared with the model by Beerens et al. (1994). However, the model by Beerens greatly simplifies the velocity field, it only obeys a simplified continuity equation: $u_x + v_y = 0$. In this way, no variations in the water depth are allowed. In order to provide a better verification, the model by Beerens is generalized by introducing depth variations. Until now, bedprofile variations were only implicitly included in the prescription of the residual velocity field. The reason for this is that residual circulation cells are induced by and attached to this bedprofile variations. However, if bedprofile variations become significant with respect to the total water depth, the prescribed velocity field has to be adjusted. Instead of a divergence free velocity field (u, v) , the model by Beerens et al. (1994) is changed to a divergence free transport field (uH, vH) :

$$\begin{aligned} \frac{dx}{dt} &= (\pi\lambda\nu\Psi_y + \pi\lambda \cos(2\pi t))/H \\ \frac{dy}{dt} &= -\pi\lambda\nu\Psi_x/H. \end{aligned} \tag{79}$$

$$H(x, y) = 1 + \epsilon \cos(\pi x) \cos(\pi y) \tag{80}$$

Here the subscript derivative notation is used, H is the dimensionless version of the waterdepth and equal to $H = 1 + \epsilon H'(x, y)$ with H' representing the bedprofile perturbation and $0 < \epsilon < 1$. The new velocity field (right hand side of equation 79) obeys a simplified version of the continuity equation:

$$\frac{\partial(uH)}{\partial x} + \frac{\partial(vH)}{\partial y} = 0. \quad (81)$$

Of course, the model by Beerens can be extended even more by allowing the water depth to change due to sea surface variations too. This changes the definition of H to $H = 1 + \epsilon \cos(\pi x) \cos(\pi y) + \frac{\zeta_0}{H_0} \cos(2\pi t)$ with ζ_0 the sea surface amplitude of M2 (1 meter). For simplicity, this additional term is omitted. Equations 79 and 80 were used as a verification for the numerical model. Characteristic values of the parameters in the first example of the numerical results (figures 29, 30 and 31) are: $\lambda = 1$ or 2 and $\nu = 0.01$. Using these parameter values to drive the modified kinematic model gives nearly identical particle trajectories when compared to the numerical results, figure 35.

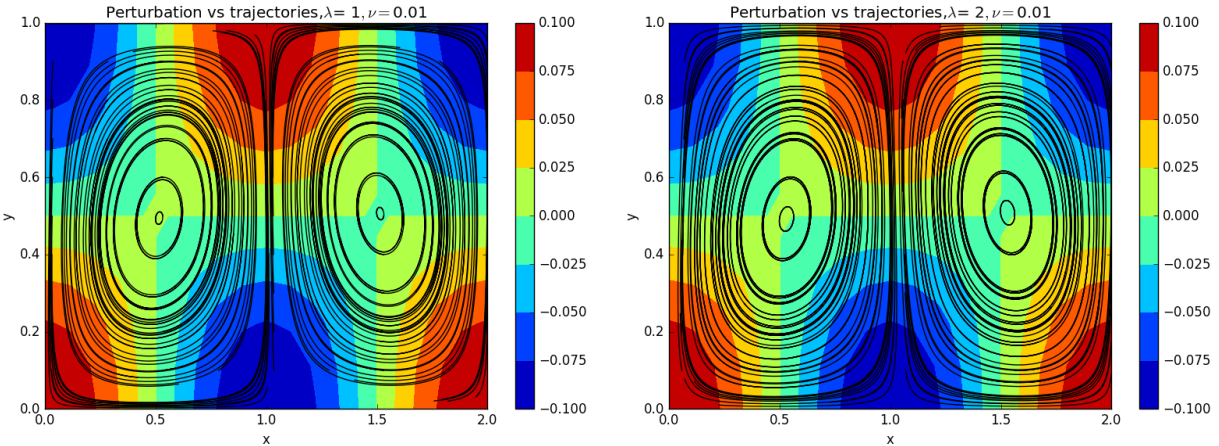


Figure 35: Particle trajectories produced by the modified kinematic model (equations 79-81) for parameter values characteristic for the estuary. Blue areas are shallow, perturbation strength is measured as a fraction of the reference depth, $H_0 = 10m$.

Interesting behaviour in the phase space occurs for combinations between λ and ν that are present in the second estuary example (figures 32, 33 and 34). In the second example of the numerical results, $\nu \approx 0.08$ and this value is used for the modified kinematic model (equation 79). Subsequently, λ is changed: for $\lambda = 1.0, 1.4, 1.5$ and 2.0 , particle trajectories are visualized in figures 36 and 37. Particle trajectories are very sensitive to changes around $\lambda = 1.5$, showing a bifurcation of cellular trajectory structures. This bifurcation, present in the phase space of the dynamical system with a simplified (analytical) velocity field, is for slightly different parameter values also present in the numerical results. In the second example of the numerical results, a similar bifurcation of these structures occurred for $\lambda = 2.5$, figure 32. In the region of $35 < x < 45$ each cellular trajectory structure splits in two smaller cellular trajectory structures.

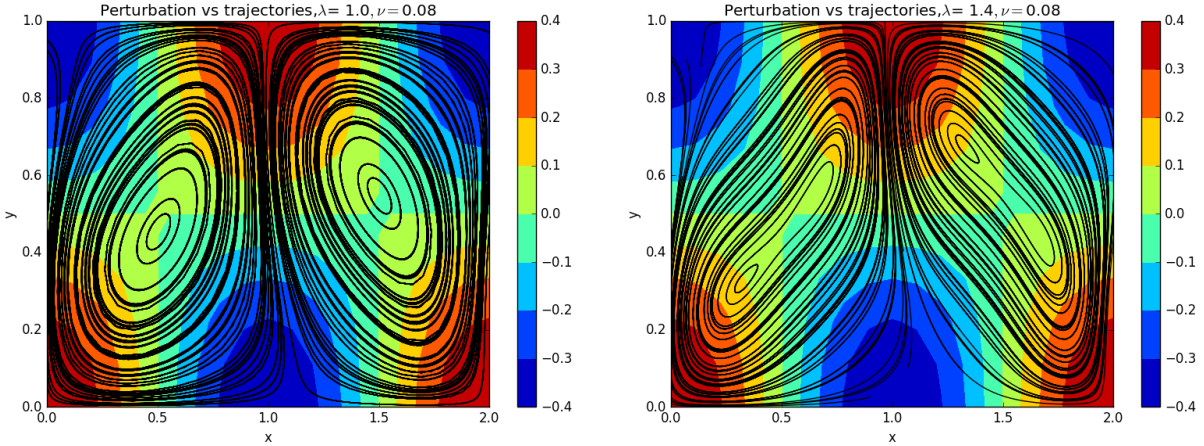


Figure 36: Pinching of the trajectories visualized for different parameters of λ . The perturbation strength is measured as a fraction of the reference depth, $H_0 = 2.5m$.

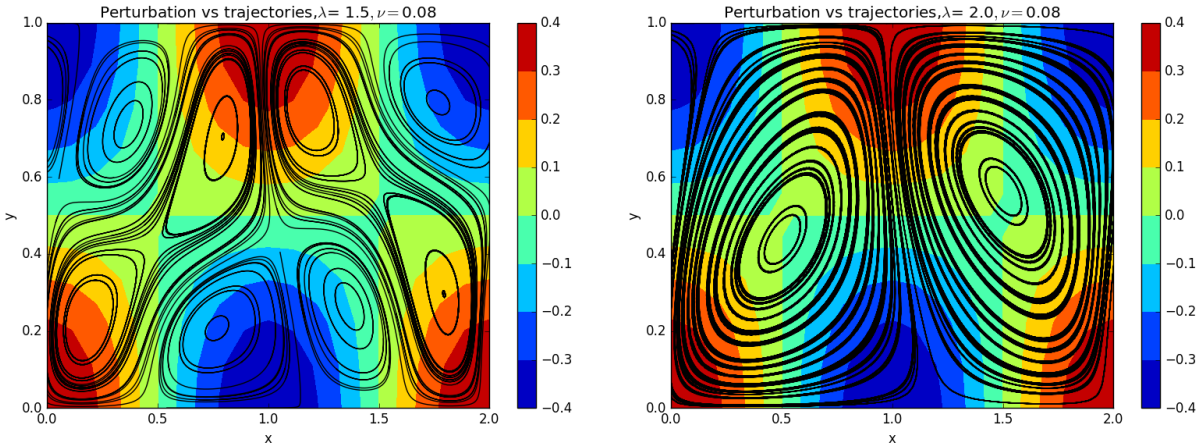


Figure 37: Pinching of the trajectories for different parameters of λ . As can be observed, exchange of particles is possible between deeper areas but not over shallow (negative perturbation) areas. The perturbation strength is measured as a fraction of the reference depth, $H_0 = 2.5m$.

In the parameter space $\lambda = 1.5$ determines the bifurcation of the circular trajectories. Varying ν has less influence, for weaker residual velocity fields $\nu \approx 0.005$, this exact bifurcation still occurs for $\lambda = 1.5$. Weaker residual velocity fields occur for either weaker perturbations or perturbations with a smaller wavelength. Only in case of relatively strong residual velocity fields, a change occurs: then the particle trajectories detach from the bedprofile perturbation, see for example figure 38.

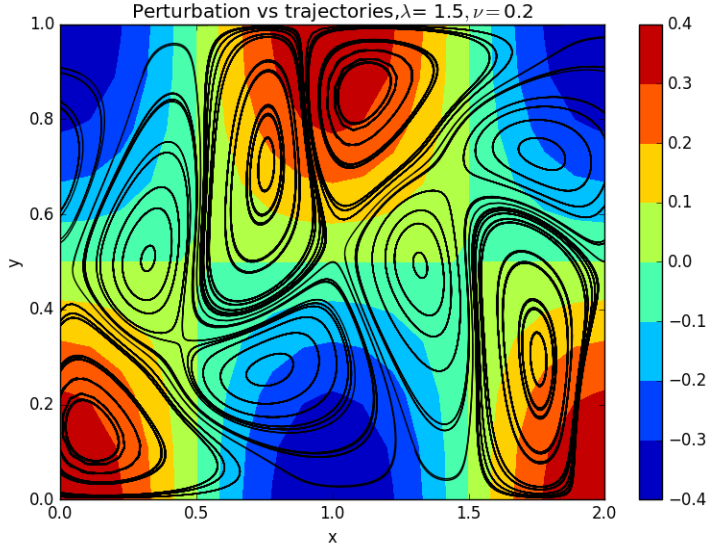


Figure 38: Relatively large ν results in seemingly detachment of the structures in particle trajectories from bedprofile perturbation. The perturbation strength is measured as a fraction of the reference depth, $H_0 = 2.5m$.

Slightly similar bifurcation behaviour around $\lambda = 1.5$ and $\nu = 0.08$ does only occur in the original model by Beerens for very different parameter combinations. In that case, a very strong residual velocity field (high ν) and much higher λ is required, which is a region in the parameter space λ, ν that never occurred in any of the estuaries studied in this project. On the contrary, the numerical model for the estuary in general suggests an anti-correlation between λ and ν , with λ decreasing towards the closed end and ν increasing, figure 33. For perturbations with a small wavelength, λ will naturally increase but ν will decrease. Possibly, if the perturbation has a longer wavelength, the flow can adjust to the perturbation more easily. This allows a stronger residual velocity field to develop and vice versa. This anti-correlation between λ and ν is also analytically confirmed by Beerens, figure 39. However, even though they established that ν and λ are not independent of each other, in their kinematic model this dependency was omitted for simplicity.

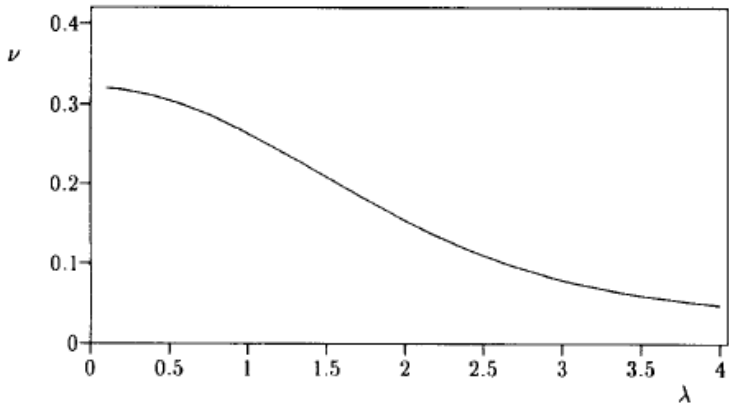


Figure 39: Anti-correlation between parameters λ and ν , analytically derived. figure from (and more details by) Beerens et al. (1994).

As already mentioned, bifurcation behaviour around $\lambda = 1.5$ does occur in the modified kinematic model and not in the original model by Beerens et al. (1994). This suggest that the inclusion of bottom variations evokes this bifurcation behaviour. One way to analyze this bifurcation behaviour, is to analyze what happens to the eigenvalues of the dynamical system (equation 79) around $\lambda = 1.5$, especially for interesting locations, such as $(x=0.5, y=0.4)$ or $(x=1.0, y=0.4)$ in figure 37a.

However, especially in the regime with $\lambda > 5-10$ and $\nu < 0.01$, characteristic for perturbations with a smaller wavelength, the modified kinematic model gives very different results than the numerical model. Whereas the numerical model produces regular chaotic trajectories, the modified kinematic model predicts trajectories as in figure 35. It is in this limit with ν approaching zero (as in figure 39) that comparison is not useful anymore. This does not necessarily mean that the numerical results are wrong but it can also illustrate a limitation of the (modified) model by Beerens. In the limit of λ approaching zero, numerical results match the analytical results of the (modified) model by Beerens. Concluding, in the numerical results, a clear bifurcation of cell-like particle trajectory structures was observed in estuaries. Variations in trajectory structures occur due to changing hydrodynamic conditions. The kinematic model by Beerens does not predict such a bifurcation of these cell-like trajectory structures unless unrealistic parameter combinations are used. On the other hand, by introducing bathymetry variations in the kinematic model, similar bifurcation behaviour is in fact reproduced for realistic parameter values. Next to this, the numerical model produces an anti-correlation between λ and ν , which can also analytically be confirmed.⁵ From this, the ability of the numerical model to simulate trajectories is considered to be decent.

5.4 Verification implementation sediment transport

Several simple experiments were conducted to ensure preservation of sediment mass. This includes verification of erosion and deposition but also changes in the sediment balance due to open boundary conditions. Below an outline of the numerical experiments is given:

- The first experiment was designed to test the implementation of deposition. Each particle was assigned with the same sediment concentration C_0 . Erosion was turned off and it was made sure that no particle left the basin through the open boundary. After simulating a few tidal periods, all sediment was lost by the particles due to deposition. Afterwards, the model provided as output the net change in the bedprofile which was exactly equivalent to the total mass initially present in the water column. Moreover, this means that no errors are made in the mass balance due to the implementation of deposition.
- During the second experiment, the erosion process was tested. The domain was initialized with particles without any sediment, $C_0 = 0$. Deposition was turned off and it was made sure that no particle left the domain during the simulation. After simulating for a few tidal periods, the total amount of sediment in the water column was compared to the net change in the bedprofile. Again, this was exactly the case.
- Thirdly, a net balance between incoming and outgoing sediment through the open boundary was ensured. During ebb, particles (still sub-volumes) leave the domain and may transport sediment out of the domain in this way. During flood, new particles spawn at the open boundary according to the amount of water that enters the domain. The model keeps track of the amount of sediment leaving the domain during ebb and consequently distributes this evenly over all the particles entering during flood. After a morphologic spin-up time of 5 tidal periods, the error made by doing so is of the order of $10^{-2}\%$. When the spin-up is completed, morphological computations will start.

From these experiments, it can be concluded that no errors are made in the conservation of mass (sediment).

5.4.1 Spatial settling lag test case

As a first morphological experiment, it was tested if the model was capable of reproducing the spatial settling lag mechanism, which is described in section 2. As an example, a basin with the following properties was selected:

- $L = 50 \text{ km}$, $W = 5 \text{ km}$
- $H = 5 \text{ m}$
- $w_s = 0.001 \text{ m/s}$
- $K_v = 0.004 \text{ m}^2/\text{s}$
- $\rho_s = 2650 \text{ kg/m}^3$
- $\gamma = 7.8 * 10^{-5}$
- $\Delta x, \Delta y = 500 \text{ m}$
- $\Delta t = 25 \text{ s}$

In this case no perturbation was applied: the bedprofile is completely flat. Furthermore, the bedprofile is updated if the accumulated result of erosion and deposition somewhere in the basin exceeds 10 cm.

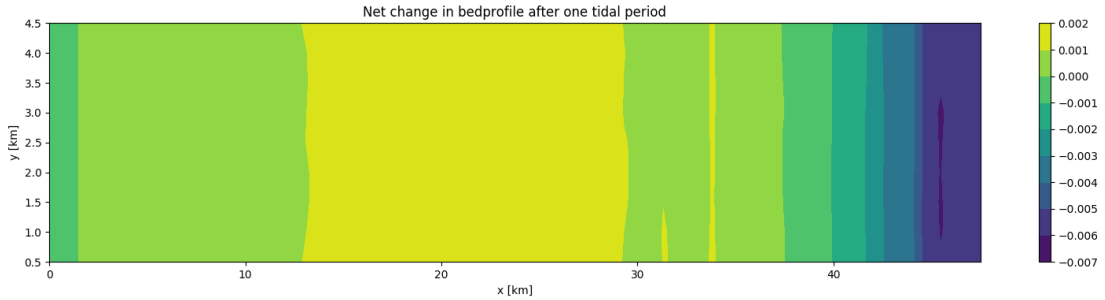


Figure 40: The net change in the bedprofile after one tidal period is shown. Positive values (yellow) indicate net deposition, negative (purple) indicates erosion in meters. A net sediment transport towards direction of decreasing tidal amplitude occurs.

Based on the dimensions, a relatively large longitudinal spatial gradient in the u-component can be expected. The reason for this is twofold: firstly it is a very shallow basin and secondly, it is a relatively short basin. Both factors contribute to an increase of the longitudinal velocity gradient. To pronounce the settling lag effect even more, a small fall velocity indicative of fine grained sediment is selected. In figure 40, the result is presented: a clear net transport of sediment in the direction towards decreasing velocity amplitudes (towards the closed end at the left). This means that this system is not in equilibrium and will adjust. For a similar basin with the same properties and parameters, except for the basin length, which is now $L = 100 \text{ km}$, the evolution of the morphology was simulated on the timescale of years. This pointed out that the system is indeed not in equilibrium, figure 41. However, the net change in the bedprofile cannot be fully attributed to spatial settling lag. For example, the presence of the M4 tidal constituent is also related to sediment transport.

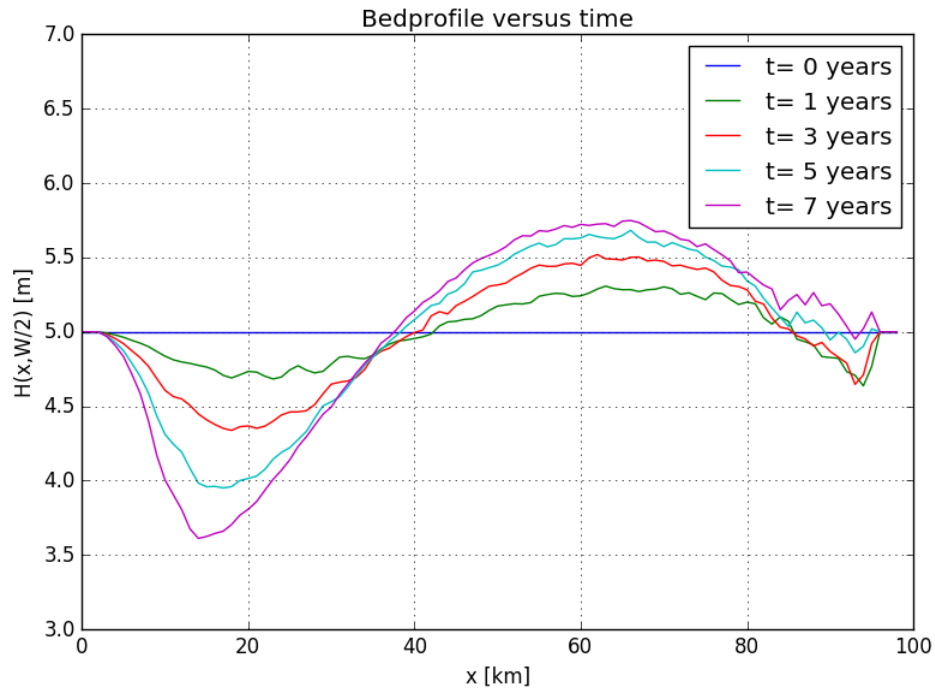


Figure 41: Significant changes in the bathymetry occur on the timescale of years. For this figure, a cross section of the domain is taken, at $y = W/2$.

6 Numerical experiments and results

This section consists of three parts, each part describes a different numerical experiment. For each experiment, the domain properties and numerical settings are briefly outlined. First of all, one example of particle tracking is added to illustrate the large variations in particle trajectory structures. In this example, clear boundaries between chaotic and trapped regions exist. In addition, two more experiments are designed to give a first impression of the model performance regarding sand bar evolution. One experiment shows the numerical results of linear stability analysis in terms of growth or decay rates. Another numerical experiment studies the morphodynamic evolution of the bathymetry on a longer timescale, in the order of a decade.

6.1 Chaotic advection of sediment

Particle trajectories are analyzed for different estuary geometries. To illustrate the appearance of chaotic regions in the domain, an example basin with the following dimensions was selected:

- $H_0 = 5 \text{ m}$
- $L = 100 \text{ km}$, $W = 2.5 \text{ km}$
- $\Delta x, \Delta y = 250 \text{ m}$
- $\Delta t = 10 \text{ s}$
- $k_x = k_y$
- $\lambda = 2500 \text{ m}$

A spatially periodic perturbation of the form:

$$H'(x, y) = 0.1H_0 \cos(k_x x) \cos(k_y y), \quad k_{x,y} = 2\pi/\lambda. \quad (82)$$

was applied to the bedprofile. The resulting particle trajectories are visualized in figure 42, 44 and 45. In the first figure an overview of the trajectories in the whole domain is given, in figure 44 and 45 two slices of the domain are shown in detail. Only a small fraction of all the particle trajectories is shown for clarity.

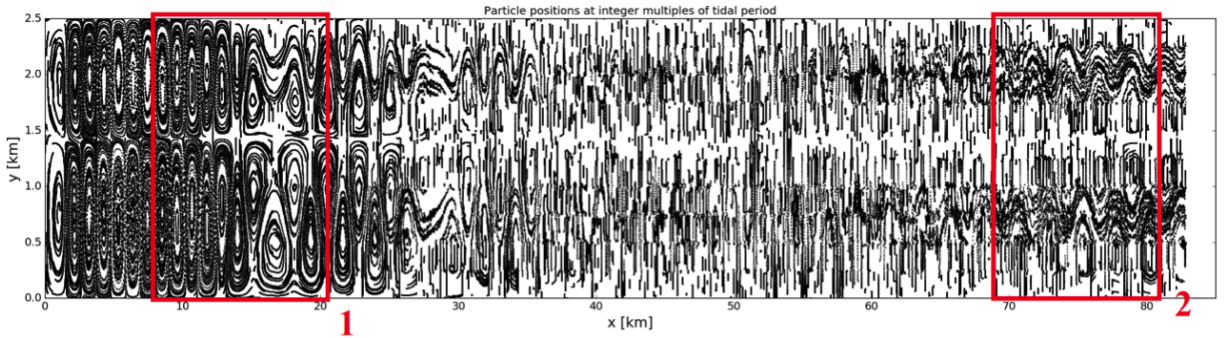


Figure 42: Overview of particle trajectories in the domain. Each dot represents particle positions at integer multiples of a tidal period. In respectively figure 44 and 45 a zoom in on the areas in the red boxes labelled 1,2 is shown.

In figures 42, 44 and 45 the dots represent particle positions at integer multiples of a tidal period. Moving from the closed end on the left towards the open boundary on the right, hydrodynamic conditions change considerably. This is twofold: both the residual velocity field and the amplitude of the tidal velocity change. Towards the closed end, the residual velocity field, measured by ν in figure 46, has strong variations in

amplitude. Variations in the tidal velocity amplitude are reflected by λ , which has a strong longitudinal dependency. λ is proportional to the tidal excursion length, which in turn is proportional to the tidal velocity. These variations in hydrodynamic conditions are reflected by the strong spatial dependency of the structures found in the particle trajectories. Towards the closed end, where less energetic hydrodynamic conditions prevail (λ goes to zero), particles are generally present in trapped regions. Particles will always end up in the same region after every tidal period. This means that there is no exchange with neighbouring residual circulation cells. On the left of figure 44, which is in the vicinity of the closed end, the circular structures show these trapped regions. Trajectories are circular, because they closely follow the residual circulation cells, which look like figure 43. On the other hand, in chaotic regions particles (sub-volumes) can move great distances through the domain. In figure 45 chaotic regions, in this case characterized by wavy structures, are alternated with trapped regions. Within these chaotic regions, particles are persistently displaced in one direction, leading to an increased dispersion (of sediment) when compared to particles in trapped regions. Within these chaotic regions, displacement occurs at a speed of at most 1 mm/s. In other words, particles, while carrying sediment, end up in other circulation cells and in this way contributing to the dispersion of sediment. Especially from halfway the domain to the open boundary, these chaotic regions become more widespread.

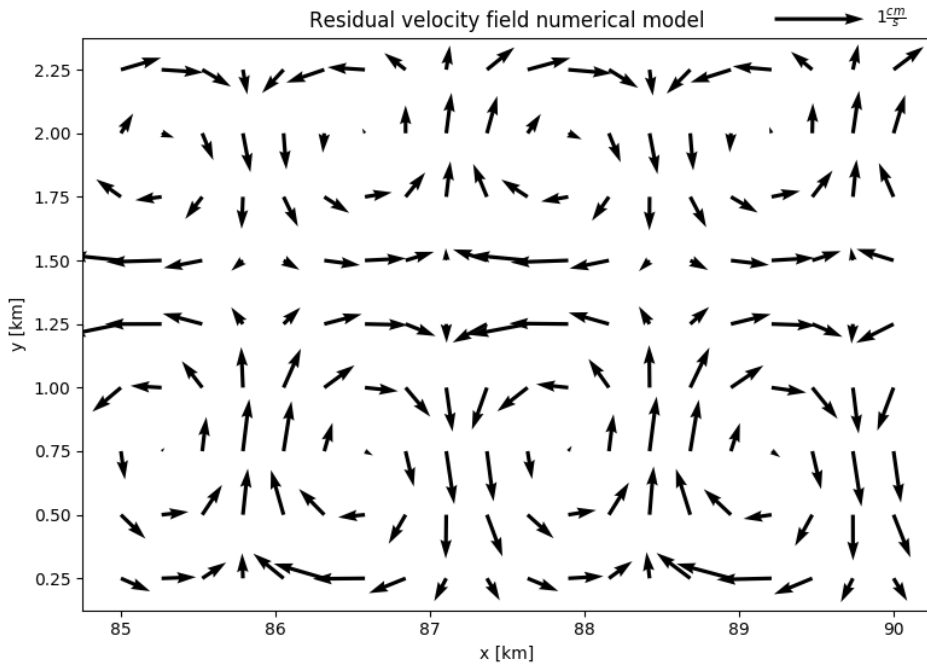


Figure 43: Residual velocity field. Towards the closed end the amplitude is in the order of 1 mm/s, towards the open boundary it is in the order of 1 cm/s. Very structured horizontal circulation cells, comparable to the model by Beerens et al. (1994), but here generated by the dynamical equations (equations 9-11).

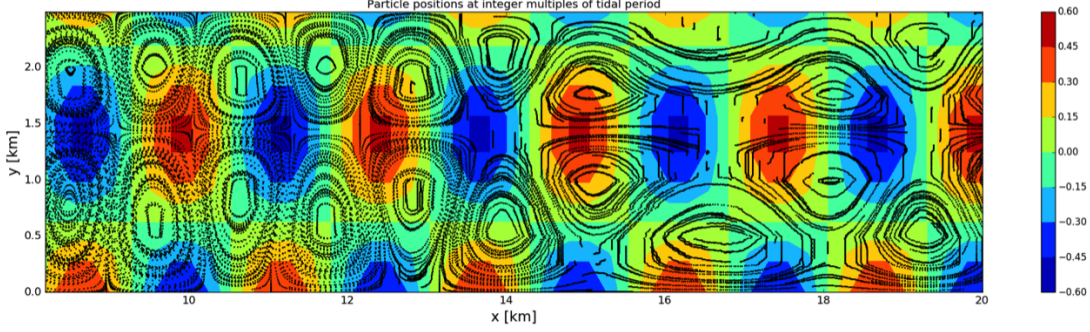


Figure 44: This is a zoom in of the left part (1) of the domain, to improve particle trajectories visualization. Each dot represents particle positions at integer multiples of a tidal period. Positive (red) values indicate deeper regions, while negative (blue) values are shallow regions.

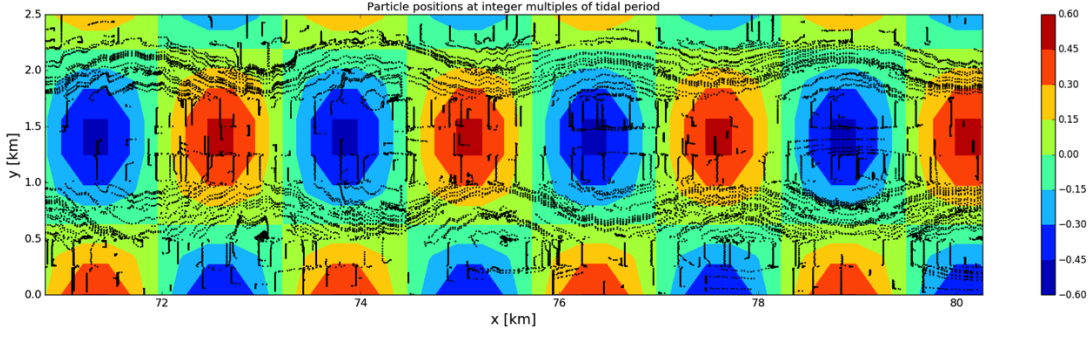


Figure 45: This is a zoom in of the right part (2) of the domain, to improve particle trajectories visualization. Each dot represents particle positions at integer multiples of a tidal period. Positive (red) values indicate deeper regions, while negative (blue) values are shallow regions.

The accompanying parameter values λ and ν for the estuary are given in figure 46. Generally, chaotic regions often occur towards the open boundary for high values of the parameter λ . High λ corresponds to a relatively long tidal excursion length and smaller perturbation wavelengths (at most 3 km). According to the model results, chaotic regions still occur for relatively weak residual velocity fields $\nu \approx 0.005$.

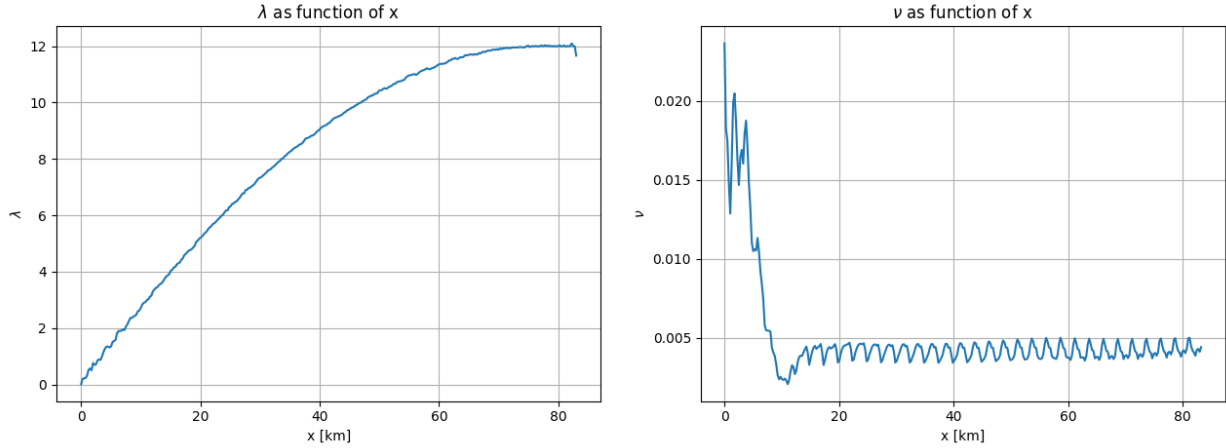


Figure 46: Parameter values as a function of x , measured along $y = W/2$. ν is small in this case, which is indicative of a weak residual velocity field. On the other hand, λ is large, reaching 12 close to the open boundary. A large value of λ is often accompanied with the appearance of chaotic regions.

6.2 Linear stability analysis

This numerical experiment aims at identifying if perturbations of the bottom grow or decay by means of a linear stability analysis. It is determined whether perturbations decay, grow or remain neutral for different perturbation shapes (equation 83). To this end, both estuary width and perturbation wavelength are varied and for each case growth/decay rates are quantified by observing the magnitude and patterns of changes in the bedprofile after simulating one tidal period.

$$H'(x, y) = A \cos(k_x x) \cos(k_y y), \quad k_x = 2\pi/\lambda. \quad (83)$$

During this simulation, the bedprofile was not updated. Nevertheless, the model monitors changes that will occur due to erosion and deposition after one tidal period. For all simulations in this experiment, the following domain properties, parameters and numerical settings are used:

- $L = 100$ km
- $H_0 = 5$ m
- $w_s = 0.001$ m/s
- $K_v = 0.004$ m²/s
- $\rho_s = 2650$ kg/m³
- $\gamma = 7.8 * 10^{-5}$
- $p = 0.3$, sediment porosity
- $\Delta x, \Delta y = 250$ m
- $\Delta t = 10$ s

Perturbation growth or decay is measured by the quantity ρ , equation 84. This involves the perturbation itself, $H'(x, y)$, and the net change in the bedprofile after one tidal period.

$$\rho(x, y) = H'(x, y) \Delta H \quad (84)$$

In section 4, the waterdepth is defined as $H(x, y, t) = H_0 + H'(x, y) + \zeta(x, y, t)$, this means that the total water depth decreases if $H'(x, y) < 0$. In other words, if $H'(x, y) < 0$, it becomes more shallow. Furthermore, the net change over one tidal period in the bedprofile is defined such that if $\Delta H < 0$, it means that net deposition occurred, i.e. the total water depth decreases and vice versa. Since both the perturbation and the net change ΔH over one tidal period can change sign, this leads to four possible scenarios:

- $H'(x, y) < 0$ and $\Delta H < 0$:

For slightly shallower regions ($H'(x, y) < 0$) where net deposition occurs ($\Delta H < 0$), it becomes even more shallow, which means perturbation growth occurs, $\rho > 0$.

- $H'(x, y) < 0$ and $\Delta H > 0$:

For slightly shallower regions ($H'(x, y) < 0$) where net erosion occurs ($\Delta H > 0$), it becomes less shallow, which means the perturbation decays, $\rho < 0$.

- $H'(x, y) > 0$ and $\Delta H > 0$:

For slightly deeper regions ($H'(x, y) > 0$) where net erosion occurs ($\Delta H > 0$), it becomes even more deeper, which means perturbation growth occurs, $\rho > 0$.

- $H'(x, y) > 0$ and $\Delta H < 0$:

For slightly deeper regions ($H'(x, y) > 0$) where net deposition occurs ($\Delta H < 0$), it becomes less deep, which means the perturbation decays, $\rho < 0$.

Obviously, since both the perturbation and the net change ΔH are spatially dependent, so is ρ . Ideally, one would label each different perturbation with one single growth or decay rate. To achieve this, ρ is averaged over every gridcell that represents perturbation crests and troughs in the second half of the rectangular domain (i.e $50 < x < 95$). In this way, each different case (a certain perturbation wavelength and estuary width) is represented with one single value that is a measure for growth or decay. Growth and decay rates are determined for perturbations with equal longitudinal and transverse wavenumbers, $k_x = k_y$. Perturbation wavelength is varied for three different estuary widths: $W = 2.5, 5.0$ and 10.0 km and for each case, ρ is determined, figure 47. As can be observed, ρ is always negative, corresponding to decay of the perturbation. Especially for perturbation wavelengths of a few kilometres, strong decay occurs. Over crests and troughs ρ was always strongly negative, in between crests and troughs, ρ was sometimes weakly positive.

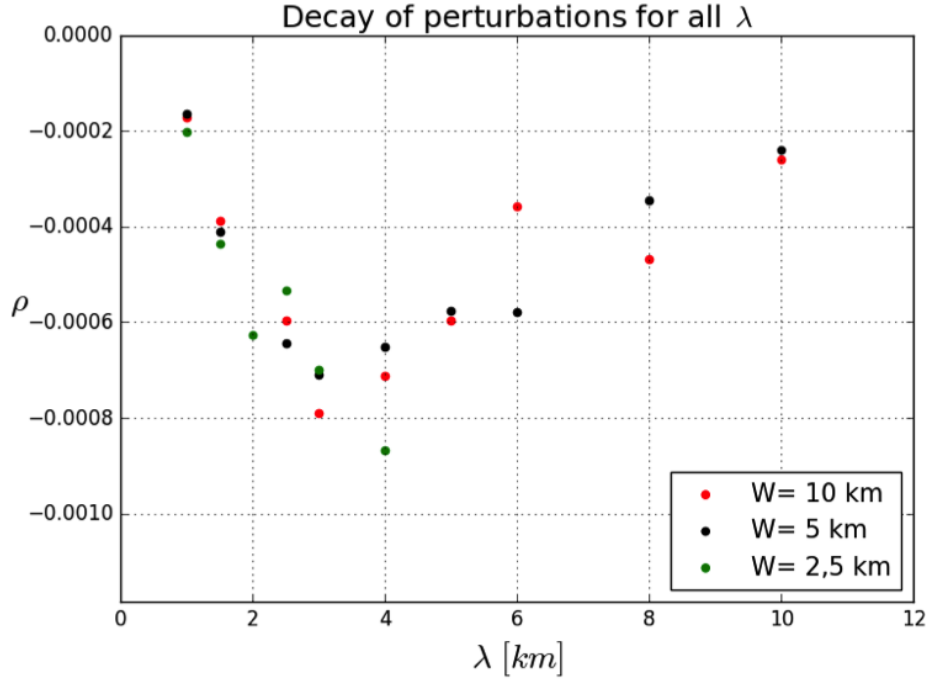


Figure 47: For every investigated combination between λ and W , it was found that $\rho < 0$. In this case $k_x = k_y$ in equation 83 with λ in the range of 1 to 10 km.

Afterwards, k_y was fixed at a few different values and only k_x is varied. For all different combinations between k_x and k_y , estuary width is varied to investigate what happens to the growth or decay rate. ρ is examined for longitudinal wavelengths in the range of 1 km up to 25 km, while $k_y = \frac{n\pi}{W}$. In figure 48 the results are presented for $n = 1$ and $n = 2$. $\rho < 0$ for all investigated combinations of λ and W (with $k_x = k_y$ in equation 83). Consequently, a flat bedprofile is stable to these specific perturbations, suggesting that the model tends to evolve towards a flat bedprofile again. See section 7 for a discussion on this trend.

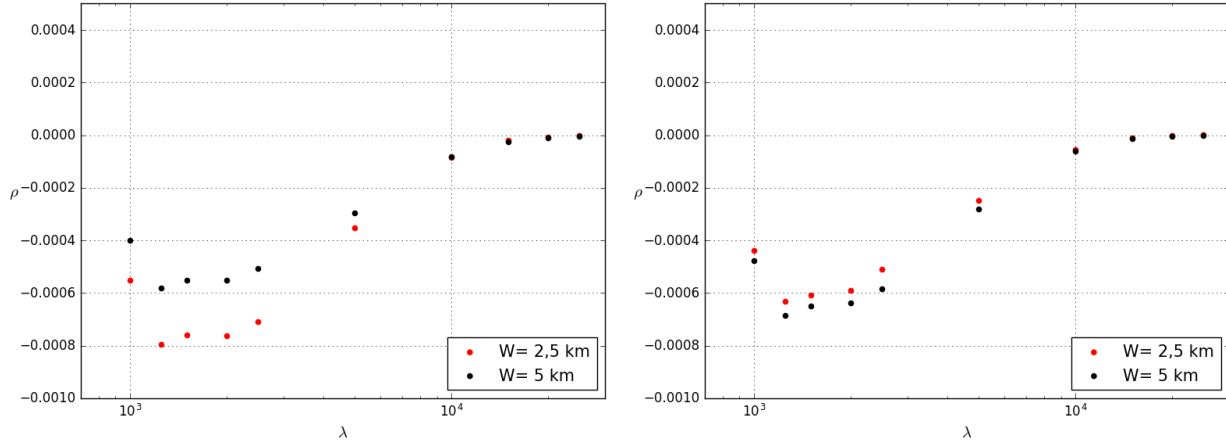


Figure 48: ρ as function of longitudinal perturbation wavelength in meters with on the left $n = 1$ and on the right $n = 2$ in $k_y = \frac{n\pi}{W}$

Until now, the growth/decay rate was investigated for different prescribed combinations of k_x and k_y . Lastly, growth/decay rate is investigated for a random perturbation. This time, the bathymetry is located at a depth of $H = H_0 + H'(x, y)$ with H' being either $-0.1H_0$, 0 or $+0.1H_0$. In words, for each gridcell the bathymetry is either elevated by 10% of the waterdepth, 10% deepened or remains unaltered. Since there is no single representative wavelength present in this case, ρ cannot be spatially averaged. Therefore a 2D plot of ρ is shown in figure 49. In this case, $\rho > 0$ at several places, indicating perturbation growth. Hence, the bedprofile is not stable against this random perturbation.

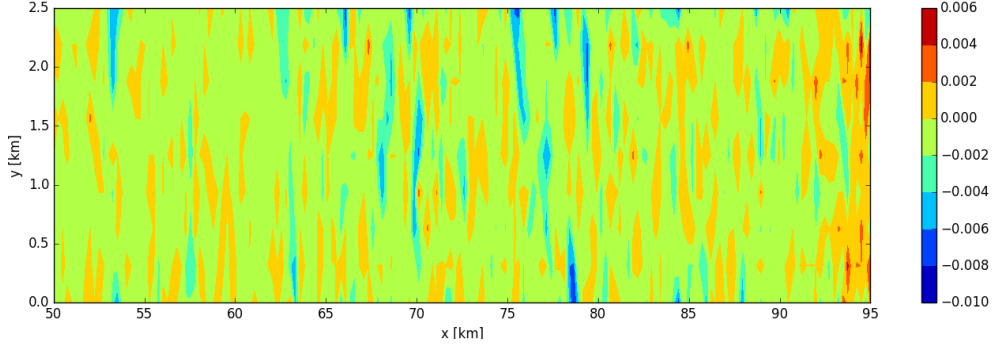


Figure 49: This graph shows the spatial variation of ρ in case of a random perturbation on a flat bedprofile: both growth and decay can be observed.

6.3 Transient morphodynamics

In the previous numerical experiment no feedback between hydrodynamics and bottom evolution was considered, i.e. simplifying the model flow chart presented in figure 8. This last experiment aims to give a first impression of morphological changes with time. Morphodynamic evolution was simulated for a period of five years, the results of the final bedprofile are presented in figure 50. As soon as the contributions of erosion and deposition exceeded 5 cm in any gridcell in the domain, the bedprofile was updated. While parameters and numerical settings are the same as in the previous experiment, the following changed:

- $L = 100$ km, $W = 10$ km
- $H_0 = 2.5$ m
- $\Delta x, \Delta y = 1000$ m
- $\Delta t = 100$ s

A spatially periodic perturbation was used:

$$H'(x, y) = A \cos(k_x x) \cos(k_y y), \quad k_x = 2\pi/\lambda. \quad (85)$$

with $A = 0.1H_0$ and a perturbation wavelength of 10 km. In figure 50 the bathymetry after 5 years is shown. While results on the short timescale suggest that the bedprofile becomes flat for this combination of λ and W , the bedprofile clearly did not become flat. Towards the closed end slightly more deposition occurred due to spatial settling lag: this region becomes even more shallow. In the region close to the open boundary, deeper regions are connected and form a channel, alternated with very shallow regions: shoals.

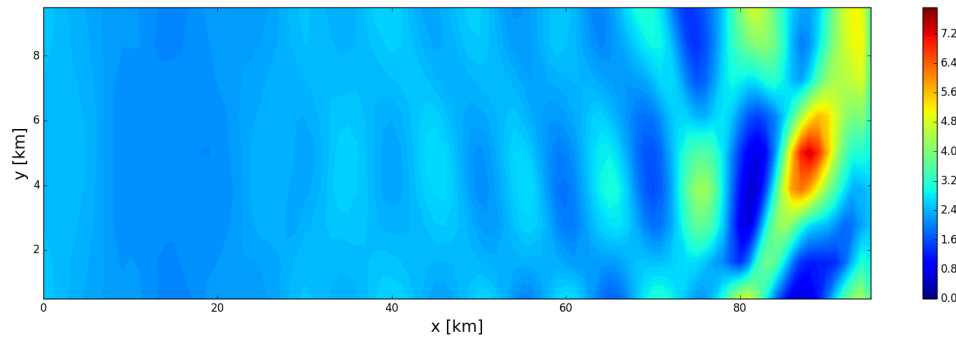


Figure 50: Bedprofile after 5 years of simulation, red represent deep areas whereas blue represents shallow areas. A channel-shoal pattern emerges close to the open boundary with stronger depth variations occurring towards the open boundary on the right.

7 Discussion

In section 6, some preliminary results regarding sand bar formation are discussed. Sand bar formation in its initial stage is investigated by applying a small spatially periodic perturbation to a flat bedprofile. This allows a comparison between numerical and analytical results derived by using linear stability analysis. According to the numerical results, ρ is always negative except for random perturbations. However, according to observations,¹⁷ the strongest growth rate is expected for wavelengths according to: $\lambda = 0.97 W^{0.87}$. Remarkably, the perturbation wavelength that corresponds to the most negative ρ is the observed dominant wavelength in estuaries. In other words, while the model predicts fastest decay, observations suggest that the same wavelength is actually the fastest growing mode (FGM). This can have different reasons. Technically, the FGM according to the analytical solution^{26,28} applies to a semi-infinite channel, bounded in the y-direction and unbounded in x-direction. Solving the eigenvalue problem (section 5 and more details by Schuttelaars and de Swart, 2002) for a domain bounded in the x-direction changes the solution for the FGM. By considering only perturbations of the form of $A \cos(k_x x) \cos(k_y y)$, the FGM may not be captured by the numerical model because the perturbation form should be different (for example Bessel functions instead of cosines). To this end, the solution of the eigenvalue problem (determined either analytically or numerically) should be used as perturbation.

Nevertheless, by using random perturbations, the correct solution of the eigenvalue problem may approximately (and accidentally) be captured. This can explain why only the random perturbations displayed growth, figure 49. Moreover, analyzing the evolution of random perturbation through time can potentially provide the FGM. Furthermore, only a small part of combinations between k_x and k_y was tested: $k_x = k_y$ in figure 47 and for two fixed transversal wavelengths, figure 48. Other combinations may still show perturbation growth. Another reason that may partly explain why no growth is observed, is due to the assumption of $H_0 \approx H$ in the computation of sediment transport by:

$$\frac{dM}{dt} = \frac{V}{H} \rho_s S_* . \quad (86)$$

This assumption only effects the erosion term, which is part of S_* . To illustrate this, the assumption of $H_0 \approx H$ in the following equation is omitted for the moment. Instead S_* is rewritten using equations 27, 30 and 31:

$$\frac{dM}{dt} = \frac{V}{H} \rho_s \left(w_s (1-p) \frac{\gamma s}{1 + \gamma s} - w_s^2 \frac{C}{K_v} \right) . \quad (87)$$

using $H\hat{C} = \rho_s C$ and $\hat{C} = M/V$ to rewrite the deposition term, see section 2 and 5, yields:

$$\frac{dM}{dt} = \frac{V}{H} \left(\rho_s w_s (1-p) \frac{\gamma s}{1 + \gamma s} - w_s^2 \frac{HM}{VK_v} \right) . \quad (88)$$

Removing the brackets cancels both H and V in the deposition term, leading to:

$$\frac{dM}{dt} = A(t) \rho_s w_s (1-p) \frac{\gamma s}{1 + \gamma s} - \frac{w_s^2 M}{K_v} \quad (89)$$

with $A(t) = V/H$ indicating the area a particle (i.e. subvolume) covers. Using $V = \Delta x \Delta y H_0 / N$ and now applying the assumption of $H_0 \approx H$ leads to the equation used in the numerical model to compute the evolution of sediment in each particle:

$$\frac{dM}{dt} = \frac{\Delta x \Delta y}{N} \rho_s w_s (1-p) \frac{\gamma s}{1 + \gamma s} - \frac{w_s^2 M}{K_v} \quad (90)$$

with N the amount of particles needed to represent the volume of water present in a gridcell. While the volume remains constant, each subvolume can adjust its own water depth H and area as long as the product remains constant, i.e. $H \cdot A = V$. In other words, both the area and water depth can still vary, but the

total volume remains constant. Variations in the area, computed by $A = V/H$, are neglected in equation 90, which is used by the model. Neglecting variations in the area, has only implications for the erosion term, the deposition remains unchanged when comparing equation 89 and 90. In shallow regions, A is slightly larger while in regions with deep water, A is slightly smaller. Therefore in shallow regions, erosion is slightly underestimated and vice versa. For the linear stability analysis the error in the computation of erosion made by this assumption is in the order of 10 %. This follows from the amplitude of the perturbation, which is 10 % of the reference depth, H_0 . However, for the simulations on the timescale of years to decades, where depth variations can become very large, the error becomes larger too. Basically, in shallow regions sediment is reworked faster than in deep regions. By keeping track of the area $A(t)$ each subvolume consumes, the assumption of $H_0 \approx H$ can be restored. This assumption possibly influences the quantity ρ but the error is still expected to be relatively small. Since the water depth is provided by the hydrodynamic model (and hence known at every location and time) and the total volume of a particle is constant, it is relatively easy to keep track of the area each particle covers and to implement this numerically.

Simulations on the longer timescale indicate that a flat bedprofile is unstable with respect to perturbations. In figure 50 the final bedprofile produced by a longer simulation is given. This result indicates that the model tries to form a channel-shoal pattern by connecting deeper regions with shallow regions (shoals) in between. Hibma et al. (2003) found a similar channel-shoal pattern. However, this simulation is still on a relatively short timescale and by no means a morphodynamic equilibrium was reached, which was the case after about 100 years of simulated time by Hibma et al. (2003). However, this longer simulation does still not provide any information about the preferred bar wavelength, morphology was still changing rapidly. Thus before the mechanism of sand bar formation is examined by means of particle tracking, the ability of the numerical model to reproduce observed sand bar dimensions (on a longer timescale) has to be tested more extensively. Furthermore, the verification of the sediment transport model can be extended by comparing model results with Delft3D, or results in other papers. Nevertheless, section 6 already illustrates the benefits of particle tracking. The first numerical experiment in section 6 shows what kind of information is otherwise lost by using an Eulerian description of sediment advection. With an Eulerian viewpoint, no information is obtained on where the water and the sediment it is holding is moving to. Due to residual currents particles experience a net displacement after each tidal period. It is important to realize that particles still represent sub-volume of water that can hold sediment, as is defined in section 1. When it comes to sediment transport, tidally averaged erosion and deposition determine morphology changes rather than instantaneous erosion and deposition rates. Equivalently, a tidally averaged net displacement of particles (holding sediment) may provide information on morphology changes. Therefore, by using a different approach to sediment transport, this can provide an additional tool to understand sand bar formation. Both chaotic regions and trapped regions have implications for sediment transport and consequently, estuary morphology. In chaotic regions sediment dispersion is enhanced because particles can travel larger distances through the domain. Their irregular movement also contributes to an enhanced dispersion of sediment. On the other hand, in trapped regions, no exchange between other circulation cells occurs. Analyzing particle trajectories and the distribution of trapped and chaotic regions in relation to ρ and estuary dimensions (width or width to depth ratio) can potentially be a first step towards understanding sand bar formation.

Concluding, this research has to be continued in order to make definite conclusions about particle tracking and understanding sand bar evolution. As a starting point, the implementation of sediment transport may be reviewed. By keeping track of the domain area each particle consumes, the assumption of $H_0 \approx H$ can be omitted in equations 90 and 89. Especially for simulations on the timescales of years benefit from this because this assumption only holds for small amplitude variations in the bathymetry. Furthermore, the incoming sediment concentration during flood at the open boundary can be changed from being constant to velocity dependent. During flood, every particle entering the estuary is now assigned a constant concentration, which is not realistic. Making the incoming sediment concentration velocity dependent can potentially also reduce morphological spin-up time. Next, one may proceed with solving the eigenvalue problem (section 5 and more details in Schuttenaars and de Swart, 1998) for a semi-enclosed basin, instead of semi-infinite. The solution to this eigenvalue problem can then in turn be used to determine the growth/decay rate ρ . In other words, if this improved solution is used, the model should give $\rho > 0$.

Additionally, the model can be improved by means of a vertically dependent eddy diffusion coefficient K_v . Until now, K_v was assumed constant. This may even influence the wavelength of the FGM.⁷ Another point of improvement is the open boundary condition. For example, during flood water in reality radially enters the estuary rather than in the current uniform way.²⁰ In fact, the asymmetry between radial-inflow and rectilinear (jet-like) outflow, may be an important mechanism for sediment transport.³¹ This potentially improves the simulation of sand bars close to the open boundary.

8 Conclusion

In this project a Lagrangian approach to sediment transport was developed and was applied to study the formation of sand bars in estuaries. Complicated numerical models can already greatly simulate the development of sand bars but the models are too complex to unravel physical mechanisms. However, theory on sand bars in estuaries still lacks an accurate predictive ability when it comes to sand bar dimensions. Theories suggest that the wavelength of the fastest growing mode is equal to the tidal excursion length, while according to observations, the bar length scales with the estuary width. This suggests that some mechanism is still missed by the current theory. In order to improve our understanding of sand bar formation in estuaries, particle tracking is used to monitor the movement of water and the sediment it is holding. This information is lost if the common Eulerian viewpoint is used to simulate sediment transport. Subsequently, a numerical model was developed, which consists of a coupled hydrodynamic and sediment transport part. The hydrodynamic model comprises the numerical solution of the two dimensional depth averaged shallow water equations. Both the hydrodynamic and sediment transport model were verified in various stages by means of benchmark problems and analytical solutions for simplified cases. After the development and the verification of the numerical model was completed, some preliminary results on sand bar formation were produced. To simulate the formation of sand bars, perturbations are applied to a flat bedprofile. Sand bar formation is investigated by applying small spatially periodic perturbations to a flat bedprofile. The evolution of these perturbations in their initial stage was monitored. Perturbation growth or decay was determined for different estuary widths and perturbation wavelengths. However, it appeared that for every combination of estuary width and perturbation wavelength a negative ρ was found, which corresponds to decay. Only for a random perturbation ρ was greater than zero. Perhaps the perturbation structure has to be different for growth to occur. Additionally, the parametrization of erosion can still be improved, which may also influence ρ . While the bedprofile was stable against all the tested perturbations on the short timescale, the bedprofile did not become flat on the longer timescale but evolves towards a channel-shoal pattern. This seemingly disagreement between short and longer timescales requires more research before particle tracking can be used to improve our understanding of sand bar formation. Nevertheless, particle tracking already proved to be useful during this project. Particle trajectories are very sensitive to changing hydrodynamic conditions, which also has implications for sediment transport. Particles can be located in either trapped or chaotic regions. Chaotic regions are characterized by irregular movement of particles through the domain, enhancing sediment dispersion in this way. Combining information about trajectories in relation to hydrodynamic conditions and regions of enhanced sediment dispersion may contribute to our understanding of sand bar formation. Concluding, even though particle tracking already proved to be useful, more research is required why all perturbations decay on the short timescale.

Acknowledgements

In the first place, I thank Leo Maas and Maarten van der Vegt for supervising my thesis, for their numerous helpful comments and suggestions. Furthermore, I thank both Christiaan van Dalum and Emmy Stigter for reviewing my thesis and giving feedback. I thank Bing Yuan for giving advice on the numerical aspects of the hydrodynamic model. Last but not least, I thank Tjebbe Hepkema for providing figure 25.

Appendix

The Thomas algorithm solves tridiagonal systems of n equations:

$$a_i x_{i-1} + b_i x_i + c_i x_{i+1} \quad (91)$$

with $i = 1, 2, \dots, n$ and $a_1 = 0$ and $c_n = 0$. In matrix form this set of equations looks like:

$$\begin{bmatrix} b_1 & c_1 & & 0 \\ a_2 & b_2 & c_2 & \\ & a_3 & b_3 & \cdot \\ & \cdot & \cdot & c_{n-1} \\ 0 & & a_n & b_n \end{bmatrix} \begin{bmatrix} x_1 \\ x_2 \\ \vdots \\ x_n \end{bmatrix} = \begin{bmatrix} d_1 \\ d_2 \\ \vdots \\ d_n \end{bmatrix}$$

where x in case of the shallow water equations corresponds to ζ . Coefficients a, b, c are known and also the right hand side is assumed to be known. In case of the shallow water equations, see section 4, this is indeed the case since a, b, c and d consist of model parameters and variable values at the previous timestep. The solution procedure to solve for x , comprises a modification of all coefficients and the right hand side. Consider the equation for x at $i = 1$ and $i = 2$:

$$i = 1 : \quad b_1 x_1 + c_1 x_2 = d_1 \quad (92)$$

$$i = 2 : \quad a_2 x_1 + b_2 x_2 + c_2 x_3 = d_2 \quad (93)$$

Rewriting the equation for $i = 1$ gives:

$$x_1 + \frac{c_1}{b_1} x_2 = \frac{d_1}{b_1}. \quad (94)$$

Introducing $c'_1 = \frac{c_1}{b_1}$ and $d'_1 = \frac{d_1}{b_1}$:

$$x_1 + c'_1 x_2 = d'_1. \quad (95)$$

Multiplying with a_2 yields:

$$a_2 x_1 + a_2 c'_1 x_2 = a_2 d'_1. \quad (96)$$

Substracting this rewritten equation at $i = 1$ from equation 93 gives:

$$(b_2 - c'_1 a_2) x_2 + c_2 x_3 = d_2 - d'_1 a_2 \quad (97)$$

and subsequently rewriting:

$$x_2 + \frac{c_2}{b_2 - c'_1 a_2} x_3 = \frac{d_2 - d'_1 a_2}{b_2 - c'_1 a_2}. \quad (98)$$

In this way x_1 is removed from the equation. Next, introduce: $c'_2 = \frac{c_2}{b_2 - c'_1 a_2}$ and $d'_2 = \frac{d_2 - d'_1 a_2}{b_2 - c'_1 a_2}$:

$$x_2 + c'_2 x_3 = d'_2. \quad (99)$$

Thus the new coefficients c'_i and d'_i are defined in the following way:

$$c'_i = \frac{c_i}{b_i - a_i c'_{i-1}}, \quad d'_i = \frac{d_i - d'_{i-1} a_i}{b_i - c'_{i-1} a_i} \quad (100)$$

and hence:

$$x_i + c'_i x_{i+1} = d'_i. \quad (101)$$

For every i , x_{i-1} , one of the unknowns, can be removed by this modification of coefficients. Eventually, at $i = n$, we obtain: $x_n = d'_n$, since $x_{n+1} = 0$. Subsequently, this value for x_n can be substituted in the equation for $i = n - 1$, yielding x_{n-1} . This backward substitution can be continued for every i , providing the solution for x_i . In other words, starting at $i = n - 1$ in equation 101, x_{n-1} can be computed, since x_n is known. Afterwards, equation 101 can be considered at $i = n - 2$ and x_{n-2} can be computed, since x_{n-1} is known, etc.

References

- ¹ ABBOTT, M. B. *Computational hydraulics*. Pitman, 1979.
- ² BAKKER, W. T. Effect of tidal resonance on the morphology of wadden and estuaries. *Netherlands centre for coastal research -*, *Internal report* (1994), –.
- ³ BAYLISS, A., AND TURKEL, E. Radiation boundary conditions for wave-like equations. *Communications of pure and applied mathematics* 33 (1980), 707–725.
- ⁴ BEARDSLY, R. C., AND HART, J. A simple theoretical model for the flow of an estuary onto a continental shelf. *Journal of geophysical research* 83 (1978), 873–883.
- ⁵ BEERENS, S. P., RIDDERINKHOF, H., AND ZIMMERMAN, J. T. F. An analytical study of chaotic stirring in tidal areas. *Chaos, Solitons & Fractals* 4 (1994), 1011–1029.
- ⁶ BESIO, G., BLONDEAUX, P., BROCCINI, M., HULSCHER, S. J. M. H., IDIER, D., KNAAPEN, M. A. F., NMETH, A. A., ROOS, P. C., AND VITTORI, G. The morphodynamics of tidal sand waves: A model overview. *Coastal Engineering* 55 (2008), 657–670.
- ⁷ BORSJE, B. W., ROOS, P. C., KRANENBURG, W. M., AND HULSCHER, S. J. M. H. Modeling tidal sand wave formation in a numerical shallow water model: The role of turbulence formulation. *Continental Shelf Research* 60 (2013), 17–27.
- ⁸ DE SWART, H. E. lecture notes physics of coastal systems, 2012.
- ⁹ DESWART, H. E., AND ZIMMERMAN, J. T. F. Morphodynamics of tidal inlet systems. *Annual review of fluid dynamics* 41 (2009), 203–229.
- ¹⁰ DODD, N., BLONDEAUX, P., CALVETE, D., DE SWART, H. E., FALQUES, A., HULSCHER, S. J. M. H., RZYNISKI, G., AND VITTORI, G. Understanding coastal morphodynamics using stability methods. *Journal of coastal research* 19 (2003), 849–865.
- ¹¹ DYER, K. R. *Coastal and estuarine sediment transport*. John Wiley & Sons Inc., 1986.
- ¹² FAIRWEATHER, G., AND NAVON, I. M. A linear adi method for the shallow water equations. *Journal of computational physics* 37 (1979), 1–18.
- ¹³ GROEN, P. On the residual transport of suspended matter by an alternating tidal current. *Netherlands Journal of Sea Research* 3 (1967), 564–574.
- ¹⁴ GUO, L., VAN DER WEGEN, M., ROELVINK, J. A., AND HE, Q. The role of river flow and tidal asymmetry on 1-d estuarine morphodynamics. *Geophys. Res. Earth* 119 (2014), 23152334.
- ¹⁵ HIBMA, A., SCHUTTELAARS, H. M., AND DE VRIEND, H. J. Initial formation and evolution of channel-shoal patterns in estuaries. *Continental Shelf Research* 24 (2003), 1637–1650.
- ¹⁶ LEENDERTSE, J. J. Aspects of a computational model for long-period water wave propagation.ph.d. thesis.
- ¹⁷ LEUVEN, J. R. F. W., KLEINHANS, M. G., WEISSCHER, S. A. H., AND VAN DER VEGT, M. Tidal sand bar dimensions and shapes in estuaries. *Earth Science Reviews* 161 (2016), 204–223.
- ¹⁸ LI, C., AND O'DONNELL, J. The effect of channel length on the residual circulation in tidally dominated channels. *Journal of physical oceanography* 35 (2005), 1826–1840.
- ¹⁹ MEYER-PETER, E., AND MULLER, R. Formulas for bed-load transport. *Proceedings of 2nd meeting of the International Association for Hydraulic Structures Research -* (1948), 39–64.

- ²⁰ NOYE, J. *Modelling coastal sea processes*. World Scientific Publishing Co. Pte. Ltd., 1999.
- ²¹ OSHER, S., ENGQUIST, B. E., AND SOMERVILLE, J. *Large scale computations in fluid dynamics*. American Mathematical Society, 1985.
- ²² OTTINO, J. M. *The kinematics of mixing, stretching, chaos and transport*. Cambridge University Press, 1989.
- ²³ PASMANTER, R. A., DRONKERS, J., AND VAN LEUSSEN W. (EDS). *Physical Processes in Estuaries*. Springer, 1988.
- ²⁴ RIENECKER, M. M., AND TEUBNER, M. A note on frictional effects in taylor's problem. *Journal of marine research* 38 (1980), 183–191.
- ²⁵ RIZAL, S. Taylor's problem - influences on the spatial distribution of real and virtual amphidromes. *Continental Shelf Research* 22 (2002), 2147–2158.
- ²⁶ SCHRAMKOWSKI, G. P., SCHUTTELAARS, H. M., AND DE SWART, H. E. The effect of geometry and bottom friction on local bed forms in a tidal embayment. *Continental shelf research* 22 (2002), 1821–1833.
- ²⁷ SCHUTTELAARS, H. M., AND DE SWART, H. E. An idealized long-term morphodynamic model of a tidal embayment. *Eur. Jour. Mech. B Fluids* 15 (1996), 55–80.
- ²⁸ SCHUTTELAARS, H. M., AND DE SWART, H. E. Initial formation of channels and shoals in a tidal embayment. *Journal of fluid mechanics* 386 (1998), 15–42.
- ²⁹ SPAGNOL, S., WOLANSKI, E., DELEERSNIJDER, E., BRINKMAN, R., MCALLISTER, F., CUSHMAN-ROISIN, B., AND HANERT, E. An error frequently made in the evaluation of advective transport in two-dimensional lagrangian models of advection-diffusion in coral reef water. *Marine ecology progress series* 235 (2002), 299–302.
- ³⁰ STELLING, S. On the construction of computational methods for shallow water flow problems. ph.d. thesis.
- ³¹ STOMMEL, H., AND FARMER, H. G. On the nature of estuarine circulation. *Tech. Report* - (1952), 52–88.
- ³² TAYLOR, G. I. Tidal oscillations in gulfs and rectangular basins. *Proceedings of the London mathematical society s2-20* (1920), 148–181.
- ³³ VAN DE KREEKE, J., AND ROBACZEWSKA, K. Tide induced residual transport of coarse sediment: application to the ems estuary. *Netherlands Journal of Sea Research* 31 (1993), 209–220.
- ³⁴ VAN RIJN, L. C. *Principles of sediment transport in rivers, estuaries and coastal seas*. Aqua publications, 1993.
- ³⁵ VAN RIJN, L. C. *Principles of fluid flow and surface waves in rivers, estuaries, seas and oceans*. Aqua publications, 2011.
- ³⁶ VERBEEK, H., WANG, Z., AND THOOLEN, P. Secondary currents in estuarine morphodynamic modelling, a case-study of the western scheldt. *Proceedings of the IAHR symposium on river, coastal and estuarine morphodynamics* - (1999), 649–658.
- ³⁷ VREUGDENHILL, C. B. *Numerical methods for shallow water flow*. Kluwer Academic Publishers, 1994.
- ³⁸ WANG, Z. B., JEUKEN, C., AND DE VRIEND, H. J. Tidal asymmetry and residual sediment transport in estuaries. - - (1999), -.
- ³⁹ ZIKANOV, O. *Essential computational fluid dynamics*. John Wiley & Sons Inc., 2010.

⁴⁰ZIMMERMAN, J. T. F. Vorticity transfer by tidal currents over an irregular topography. *Journal of Marine Research* 31 (1980), 603–630.

⁴¹ZIMMERMAN, J. T. F. On the lorentz linearization of a quadratically damped forced oscillator. *Physics letters* 89A (1982), –.